Title
ENVIRONMENTAL EFFECTS ON PHOTOINDUCED ELECTRON TRANSFER REACTIONS

Author
Casti, T.E.

Publication Date
1985-12-01

Lawrence Berkeley Laboratory
UNIVERSITY OF CALIFORNIA

CHEMICAL BIODYNAMICS DIVISION

ENVIRONMENTAL EFFECTS ON PHOTOINDUCED ELECTRON TRANSFER REACTIONS

T.E. Casti
(Ph.D. Thesis)

December 1985

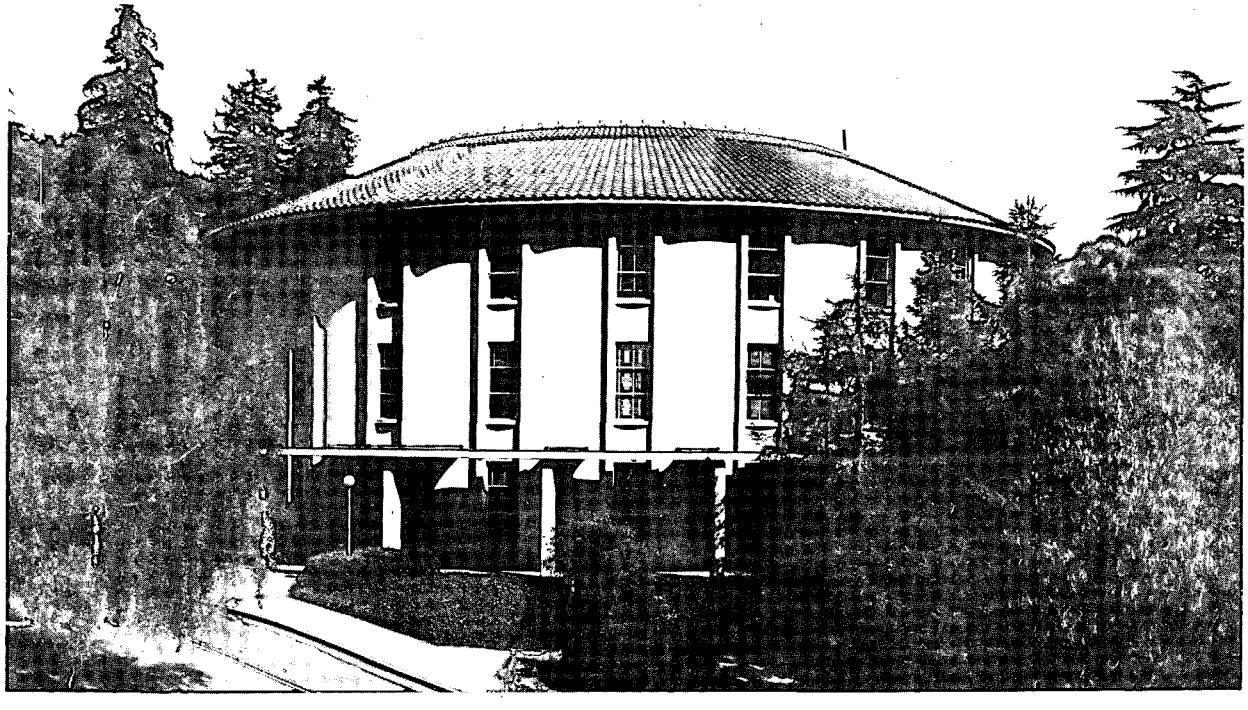

Prepared for the U.S. Department of Energy under Contract DE-AC03-76SF00098

DISCLAIMER

LBL-20817

Environmental Effects on Photoinduced Electron Transfer Reactions

Thomas Edward Casti

Ph.D. Thesis

Lawrence Berkeley Laboratory
University of California
Berkeley, California 94720

December 1985

This work was supported by the Office of Basic Energy Sciences, Chemical Sciences Division of the U.S. Department of Energy under Contract Number DE-AC03-76SF00098.

Environmental Effects on Photoinduced Electron Transfer Reactions

Thomas E. Casti

Abstract

Photoinduced electron transfer reactions between an electronically excited photosensitizer molecule and a reversible electron acceptor capable of hydrogen production are currently being studied to determine the possible utility of these reactions in solar energy conversion systems. For efficient operation of these reaction systems, the back-reaction between initial photoproducts must be minimized. Charged macromolecular systems, e.g., colloidal silica sols and polyelectrolytes, have been utilized in the past to reduce the back-reaction rate through electrostatic interactions between the charged macroions and oppositely charged photoproducts.

The influence of charged macromolecules on the forward and back electron-transfer reaction between oppositely charged initial photoproducts, the photosensitizer Zinc tetra(4-N-methyl pyridinium) porphyrin (ZnP^{+4}) and the neutral electron acceptor, propyl viologen sulfonate (PVS°), has been investigated using continuous photolysis and flash photolysis techniques.

Polyelectrolytes have been shown to have a profound influence on interionic reaction rates. Polyelectrolyte addition increases the rate of reaction between similarly charged species and decreases the rate of reaction between oppositely charged species. Flash photolysis experiments have been performed to study the effect of anionic polyelectrolyte poly(styrene sulfonate) (PSS) on the photoreaction between ZnP^{+4} and PVS°. These experiments show that <u>all</u> bimolecular rate constants involving PSS-bound ZnP^{+4} are decreased by a factor of 40-100 relative to solutions containing no polyelectrolyte. This result can be understood in terms of a hydrophobic "envelopment" of ZnP^{+4} by PSS. Steric blockage of the approach of reactants by the polyelectrolyte supresses <u>all</u> bimolecular reactions involving PSS-bound species.

Addition of the cationic polyelectrolyte poly(N,N-dimethyl-3,5-dimethylene piperidinium chloride) instead of PSS results in a <u>selective</u> decrease in back-reaction rate by a factor of ≈ 2. This observation is consistent with the primary salt effect mechanism of the influence of polyelectrolytes on interionic reactions.

The influence of negatively charged colloidal silica particles on the photoreaction between ZnP^{+4} and PVS° is well known. The strong electric field surrounding the charged silica particle acts to prevent back reaction between particle-bound $ZnP^{+5\cdot}$ and $PVS^{-\cdot}$. A serious limitation in the use of these colloids has been the instability of the silica particles in neutral

and acidic media. $PVS^{-\cdot}$ is thermodynamically incapable of water reduction to hydrogen in high pH media.

Alumina-modified colloidal silica sols are commercially available that have highly acidic aluminosilicate surface sites which give the modified sols substantial stability in neutral and acidic pH media. These sols were studied to determine their effectiveness as charged interfacial systems for supressing back reaction throughout a broad pH range.

A kinetic model has been developed that describes the transient absorbance behavour of ZnP^{+4}/PVS°/colloidal silica photolysis systems in which scavenging of $PVS^{-\cdot}$ by residual O_2 occurs. Flash photolysis experiments confirmed that alumina-modified silica particles are significantly more effective than unmodified silica sols in neutral pH media at decreasing the rate of back-reaction between $ZnP^{+4\cdot}$ and $PVS^{-\cdot}$. At pH 7, the addition of alumina-modifed silica sol decreases the back reaction rate (k_b) by almost three orders of magnitude relative to homogeneous solution, from 7×10^{9} M^{-1} s^{-1} to 1.2×10^{7} M^{-1} s^{-1}. Temperature dependance studies have determined that the activation energy for back-reaction in the presence of alumina-modified silica particles at pH 7 is 13.4 kJ/Mole. This corresponds to an effective surface potential of 140 mV, which is in good agreement with published reports of the surface charge density of colloidal silica sols.

A study of the effect of silica particle size on back-reaction rates shows that for the particle size range between 7 and 22 nm, no express dependence of k_b on particle size exists. This is in agreement with

predictions based on dimensional considerations that collision-controlled reaction rates involving a reactant bound to a spherical particle are independant of particle size.

Melvin Calvin

Acknowledgements

I would like to thank my research directors, Professor Melvin Calvin and Dr. John Otvos for their, advice, inspiration, criticism, encouragement and support throughout my graduate career. Professor Calvin's boundless enthusiasm and Dr. Otvos' critical scientific expertise will continue to be examples for me throughout my scientific career.

I am indebted to various members of the faculty at Cal, especially Professor George Pimentel for chairing my oral examination committee and for being one of the readers of this thesis. I also wish to thank Professors Ken Sauer, Marcin Majda and John Clark for helpful discussions concerning my research.

I would like to thank the various support personnel in the Calvin Lab for sharing their considerable technical knowledge and wisdom (and a few other things) with me. In particular I wish to thank Gary Smith, Phil Eggers, and Mike Press for their understanding and patience the last four years.
Of the many people that were part of the Calvin group during my time at Berkeley, I wish to particularly thank Mike Kahlow, Cindy Skrukrud, Marilyn Taylor and Professor Larry Spreer for their friendship and support.
Thanks also go to my two undergraduate assistants, Barrie Shaffer and Kim Nguyen. I truly enjoyed their help and companionship.

This thesis would not have been possible without the encouragement and support of my wife Catherine, whose support and encouragement has sustained me throughout even the most trying times of my graduate career.

This thesis is dedicated to the memory of my father, Paul R. Casti.

Although my father was not a scientist or a teacher, I nevertheless learned a few important things from him that don't have anything to do with chemistry. He had a simple goal: he wanted his children to be better than him. I cannot think of a higher aspiration than that.

Table of Contents

Abstract 1

Acknowledgements i

Dedication ii

Table of Contents iii

List of Figures xiii

List of Tables xvi

Chapter 1: Introduction

1.1 Scope and Outline 1

1.2 Historical Background 2

1.3 References. 13

Chapter 2: Experimental Techniques 15

2.1 Synthesis and Purification of Reagents 15

2.1.1 Synthesis and Purification of Zinc tetrakis(4-N-Methylpyridinum)Porphyrin, Tetraperchlorate salt (ZnP^{+4}). 16

2.1.2 Synthesis of Propyl Viologen Sulfonate (PVS°) 17

2.2 Laser Flash Photolysis Experiments 17

2.2.1 Candela SLL-66A Dye Laser 20

2.2.1.1 Operating Procedures 21

2.2.1.2 Safety Considerations 21

2.2.1.3 Laser system components 22

2.2.1.4 Choice of Flashlamp 23

2.2.1.5 Choice of Laser Dye 25

2.2.1.6 Laser Head Installation and Alignment . 27

2.2.1.7 Laser Testing 29

2.2.2 Transient Absorbance Spectrometer 34

2.2.2.1 Probe Beam Source 35

2.2.2.2 Wavelength Discrimination: Monochromator vs. Interference Filter 37

2.2.2.3 Time-Resolved Detection 37

2.2.2.4 Correction of Sample Detector Bias . . 38

2.2.2.5 Adjustment of Optics 41

2.2.2.6 Data Collection and Storage 41

2.2.4 Experimental Procedure 42

2.2.4.1 Startup 42

2.2.4.2 Preparation of Laser 43

2.2.4.3 Optics and Electronics Adjustments . . 44

2.2.4.4 Data Collection and Storage 47

2.2.4.5 Data Manipulation 49

2.2.4.5.1 Transformation of Raw Data 49

2.2.4.5.2 Signal-to -noise ratio . . 51

2.2.5 Specific Experimental Procedures 51

2.2.5.1 Determination of Excited State Extinction Coefficients 52

2.2.5.2 Determination of Oxygen Concentration in ZnP^{+4} Samples Using Excited-State Quenching Methods 55

2.3 Continuous Photolysis Experiments 60

2.3.1 Design and Construction 61

2.3.1.1 Actinic Source and Fiber Optics Connection 61

2.3.1.2 Cell Holder Assembly 61

2.3.1.3 Design of Continuous Photolysis Cell . . 65

2.3.2 Experimental Procedure 68

2.3.2.1 Data Storage 68

2.3.2.2 Actinometery and Spectral Convolutive Techniques 69

2.3.2.2.1 Reinecke's salt actinometery 70

2.3.2.2.2 Thermopile Actinometery 71

2.3.2.2.3 Spectral Convolutive Techniques 72

2.4 References 76

Chapter 3: Effect of Polyelectrolytes and Charged Interfaces on Photoinduced Electron Transfer Reactions

3.1 Introduction 77

3.2 Macroion Effects on Interionic Reactions 80

3.2.1 Salt Effects of Simple Electrolytes 82

3.2.1.1 Primary Salt Effects of Simple Electrolytes 82

3.2.1.2 Secondary Salt Effects of Simple Electrolytes 84

3.2.2 Salt Effects of Polyelectroytes 85

3.2.2.1 Deviation of Macromolecular Solutions from Ideality 86

3.2.2.2 Assumptions of Brønsted Theory . . . 86

3.2.2.3 Assumptions of Debye-Hückel Theory . 88

3.2.3 Hydrophobic Effects of Polyelectrolytes . . . 90

3.2.4 Pressure Influences on Solvation and Desolvation in Polyelectrolytes Systems 91

3.2.5 Conclusions 93

3.3 Polyelectrolyte Influences on Photoinduced Electron-Transfer Reactions: A Review 94

3.5 References 98

Chapter 4: Polyelectrolyte Effects on the Photoinduced Electron Transfer Reaction Between ZnP^{+4} and PVS°.

4.1 Introduction 100

4.2 Experimental Section 101

4.2.1 Materials 101

4.2.2 Measurements 103

4.2.3 Methods 103

4.2.3.1 Spectropholometric Titration of ZnP^{+4} by PSS and Poly(vinyl sulfate) . . . 103

4.2.3.2 Sample Preparation for Flash Photolysis Experiments 104

4.2.3.3 Sample Preparation for Continuous Photolysis Experiments 105

4.2.3.4 Determination of the Viscosity of PSS-Containing Aqueous Solutions . . 105

4.2.3.5 Electrochemical Methods 107

4.3 Experimental Results 107

4.3.1 Spectral Changes of ZnP^{+4} in PSS Solutions . . 107

4.3.1.1 Spectral "Flattening of ZnP^{+4} Induced by Aggregation of ZnP^{+4} onto PSS . . . 109

4.3.1.2 PSS-induced Shift in λ_{max} of ZnP^{+4} . . 118

4.3.1.3 Conclusions 122

4.3.2 Continuous Photolysis Experiments 123

4.3.2.1 Introduction 123

4.3.2.2 Results of Continuous Photolysis Experiments 123

4.3.2.3 Sacrificial Donor Reactions 126

4.3.3 Laser Flash Photolysis experiments 130

4.3.3.1 Introduction 130

4.3.3.2 Results 132

4.3.3.2.1 Fitting of Transient Absorbance Data to Kinetic Model . . . 132

4.3.3.2.2 Results of Data Simulations of Transient Absorbance Data 137

4.3.4 Discussion 144

4.5 Conclusions 148

4.6 References 150

Appendix 4.1 Fortran listing of program INT.FOR used to simulate transient absorbance data 152

Chapter 5: Alumina-Modified Silica Colloids as Charged Interfaces to Prevent Back-Reaction in Photoinduced Electron Transfer Reactions

5.1 Introduction 153

5.1.1 Previous Use of Colliodal Silica Sols in Artificial Photosynthetic Systems 155

5.1.1.1 Literature Review 155

5.1.2 Theory of Electrostatic and Dimensional Effects of Charged Colliodal Particles on Interionic Reaction Rates 159

5.1.2.1 Introduction 159

5.1.2.2 Electrostatic Effects of Charged Particles on Interionic Reactions 161

5.1.2.2.1 Calculation of the Electric Field Surrounding a Charged Particle 161

5.1.2.2.2 Influence of Electric Field on Interionic Reaction Rates . 163

5.1.2.3 Influence of Dimensionality on Bimolecular Reaction Rates Involving a Surface-bound Reactant 169

5.1.3.2.1 Theoretical Calculation of Dimensional Influences on Bimolecular Reaction Rates 170

5.1.2.4 Summary 175

5.1.3 Conclusions 176

5.2 Physical and Chemical Properties of Colloidal Silica Sols . 178

5.2.1 Unmodified Sols 178

5.2.1.1 Commercial Preparation 179

5.2.1.2 Surface Charge Density 180

5.2.1.3 Acidity of Surface Silanol Groups . . 181

5.2.1.4 Stability of Silica Sols 182

5.2.2 Alumina Modified Sols 184

5.2.2.1 Commercial Preparation 184

5.2.2.2 Surface Acidity of Alumina-Modified Silica Sols 185

5.2.2.3 Stability of Alumina Modified Silica Sols Compared to Unmodified Silica . . . 186

5.2.3 Summary 187

5.3 Effect of Alumina-Modified Colloidal Silica Sols on The Photoinduced Electron Transfer Reaction Between ZnP^{+4} and PVS° 190

5.3.1 Introduction 190

5.3.2 Experimental Section 190

5.3.2.1 Materials 190

5.3.2.2 Purification and Characterization of Colloidal Silica Sols 191

5.3.2.3 Measurements & Methods 195

5.3.2.3.1 Sample Preparation for Flash Photolysis Experiments 195

5.3.3 Flash Photolysis Experiments 197

5.3.3.1 Kinetic Model 197

5.3.3.2 Effect of pH and Ionic Strength on Back-Reaction 213

5.3.3.3 Effect of Temperature: Determination of The Effective Electric Field Surrounding a Charged Silica Particle 218

5.4 Conclusions 222

5.5 References 224

List of Figures

1.1 Cyclic Photochemical Scheme 1

1.2 Reaction Scheme Utilizing Charged Macromolecules . . . 7

2.1.1 NMR Spectrum of Propyl Viologen Sulfonate 18

2.2.1 Flash Photolysis Spectrometer Schematic. 19

2.2.2 Design of Special Cells Used in Flash Photolysis Experiments 25

2.2.3 Effect of Laser Voltage on Laser Pulse Power 33

2.2.4 Effect of Laser Power on Initial Absorbance Change at 480 nm of 1×10^{-5} M ZnP^{+4} Solution 54

2.2.5 Effect of Oxygen Addition on the Excited State Triplet Lifetime of ZnP^{+4}: Determination of Residual Oxygen Concentration and k_{O_2} 59

2.3.1 Light Input Assembly for Continuous Photolysis Apparatus 62

2.3.2 Cell Holder Assembly for Continuous Photolysis Apparatus 63

2.3.3 Circuit Diagram for Stirrer Controller Used in Continuous Photolysis Apparatus 66

2.3.4 Continuous Photolysis Cell Design 67

4.3.1 Spectral Titration of ZnP^{+4} with PSS 108

4.3.2 Effect of PSS Addition on Extinction Coefficient of ZnP^{+4} Soret Band $\epsilon_{\lambda max}$ 110

4.3.3 Effect of Solvent Dielectric on ZnP^{+4} Soret band λ_{max} . . 121

4.3.4 Effect of PSS and Colloidal Silica on the Quantum Yield of $PVS^{-\cdot}$ Formation in Continuous Photolysis Experiments . 125

4.3.5 Effect of PSS on the Transient Absorbance Behavior of $PVS^{-\cdot}$ 139

4.3.6 Calculated vs. Experimental Transient Absorbance Change at 600 nm: Homogeneous Solution 140

4.3.7 Calculated vs. Experimental Transient Absorbance Change at 600 nm: PSS-Containing Solution 141

4.3.8 Calculated vs. Experimental Transient Absorbance Change at 600 nm: PolyP-Containing Solution 142

5.1.1 Effect of Surface Potential on Reaction Rate 167

5.1.2 Surface Charge Density vs. k/k^* 168

5.2.1 Effect of Alumina Modification on Silica Sol Stability . . 188

5.3.1 Apparatus for Cleaning Ion-Exchange Resins 193

5.3.2 Transient Absorbance Data: Colloidal Silica Containing Samples 200

5.3.3 Transient Absorbance Data: Homogeneous vs. Colloidal Silica Containing Solutions 202

5.3.4 Transient Absorbance Data: Colloidal Silica Containing Samples: Reciprocal Absorbance vs. Time . . 204

5.3.5 Transient Absorbance at 600 nm of Colloidal Silica-Containing Sample: Reciprocal Absorbance vs. Time 210

5.3.6 Graphic Determination of k_b and k_{O_2} 211

5.3.7 Effect of pH on Back-Reaction Rates:
Alumina-Modifed vs. Unmodifed Ludox Colloidal Silica Sol . 215

5.3.8 Effect of Ionic Strength on Back-Reaction Rates:
Alumina-Modified Silica-Containing Samples 217

5.3.9 Arrhenius-Type Plot to Determine Surface Potential of Ludox AM
Alumina-Modified Colloidal Silica Sol 221

Table of Tables

2.2.1 Kinetic Data Used to Calculate Oxygen Quenching Rate and Concentration in Argon-Bubbled Degassed Solutions . . . 58

4.3.1 Effect of Solvent Viscosity on Capillary Flow Rate . . . 106

4.3.2 Calculations of Molecular Aggregate Dimensions Based on Flattening Effects for 4K and 35K MW PSS Samples . . . 116

4.3.3 Extinction Coefficicents Used in Kinetic Analysis of Flash Photolysis Experimental Data 137

4.3.4 Calculated Rated Constants Determined By Curve Fitting of Transient Data to Proposed Kinetic Scheme 143

Chapter 1: Introduction

1.1 Scope and Outline

As fossil fuels are become less abundant and more difficult to obtain, alternative energy sources must be developed to satisfy the world's future energy needs. The United States currently imports a significant percentage of the total amount of crude oil it consumes.[1] The current world political situation cannot guarantee that a plentiful supply of crude oil will always be available to import. Although the United States produces the majority of the crude oil that is needed for energy production and chemical feedstocks, some estimates predict that the current oil supply will be exhausted sometime in the beginning of the next century.[2] Alternate sources of energy must be developed to reduce this nation's current dependence on these nonrenewable fossil fuel reserves.

Although the depletion of world crude oil reserves is a long term problem, there are short term benefits to research in alternative energy technologies. Economic and political benefits include a decrease in the exposure of oil importing countries to the risk of sudden disruptions in crude oil supply and/or price escalations. The development of economically competetitive alternatives to fossil fuel burning sets a price ceiling on crude oil.

Fossil fuel burning is the major source of atmospheric pollutants (CO_2, soot, acid rain, etc.). Even if a major improvement in pollution

control technology occurs, the continued burning of fossil fuels will almost certainly lead to an increase in atmospheric CO_2 levels and concommitant changes in our planet's climate.[3]

Alternative energy sources, including hydroelectric, geothermal, and nuclear technologies, do not contribute to increasing atmospheric CO_2 levels. Unfortunately, these sources are inadequate to supply current or future demand for energy. A process that would allow the direct conversion and storage of solar energy in the form of clean burning fuels such as H_2 and O_2 would help to decrease the need for power obtained from fossil fuel burning and control the increase of atmospheric CO_2.

Current research in solar energy conversion technology includes studies of photovoltaic, photochemical and biological systems. Research efforts in the Calvin group have concentrated on photochemical methods of solar energy storage. This thesis describes experiments designed to probe the mechanism of certain photoinduced electron transfer reactions in a effort to develop an artificial photosynthetic system that is capable of the efficient capture and storage of the energy of solar photons.

1.2 Historical Background

The use of photoinduced electron transfer reactions in solar energy storage systems was first proposed by Arnon in 1961.[4] Since that time, numerous experiments have been performed to develop an understanding of

the mechanism of these reactions. The term "artificial photosynthesis" has often been applied to these systems, as these reactions mimic the stepwise electron transfer reactions that occur in natural photosynthetic systems (green plants). These studies have been the subject of a number of recent review articles in the literature.[5]

A generalized reaction scheme for photoinduced electron transfer reactions used in artificial photosynthetic systems is shown in figure 1.1.

Figure 1.1 : Cyclic Photochemical Scheme

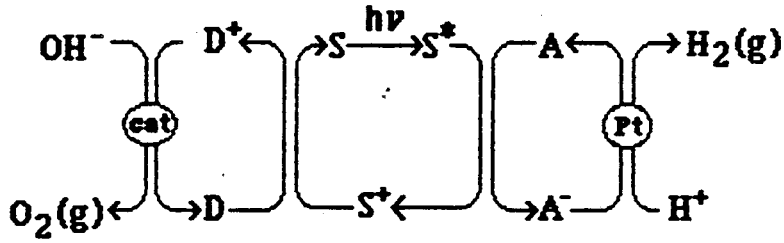

Net photoreaction:

$$2H_2O + h\nu \Longrightarrow 2H_2(g) + O_2(g)$$

Photons are absorbed by a photosensitizer, S, which is electronically excited into a higher energy state, S^*. Oxidative quenching of S^* by a reversible electron acceptor, A, occurs, resulting in the formation of the initial photoproducts, $P^{+}\cdot$ and $A^{-}\cdot$. The reduced electron acceptor, $A^{-}\cdot$, functions as an electron shuttle between the

photosensitizer and a catalyst (typically a Pt colloid) which mediates the redox reaction between $A^{-\cdot}$ and H^+, regenerating A and forming H_2 (g). The oxidized sensitizer, $P^{+\cdot}$, formed by the initial electron transfer reaction is re-reduced by an electron donor. The oxidized donor, $D^{+\cdot}$, functions as an electron shuttle between P and another catalyst system which mediates the oxidation of H_2O to H^+ and O_2, using D as an electron sink. In some cases the donor species itself may function as the catalyst for O_2 formation.

H_2O is used as the ultimate source and sink of electrons. Water is the only reactant used up in the entire cyclic system. H_2 and O_2 are the ultimate photoproducts. The net photoreaction is:

1.1) $$2H_2O + h\nu \rightarrow H_2(g) + O_2(g)$$

One of the major difficulties associated with cyclic reaction systems such as the one shown above is the loss of quantum efficency owing to back-reaction between the primary photoproducts, $P^{+\cdot}$ and $A^{-\cdot}$, which competes with the forward reactions of the initial photoproducts to form stable photoproducts. If the energy wasting back-reaction can be prevented long enough to allow the removal of either $P^{+\cdot}$ or $A^{-\cdot}$ via forward reaction with electron shuttles or catalysts, the overall quantum efficiency of the reaction system can be increased.

Back-reaction is energetically favorable (exothermic) and generally

occurs via a diffusion-controlled reaction ($k_b \approx 10^{10}$ M^{-1} s^{-1}). Subsequent reactions of the initial photoproducts, which compete with energy wasting back reaction, result in a net storage of energy. In most cases the reactions of the initial photoproducts, $P^{+}\cdot$ and $A^{-}\cdot$, involves the reaction of these species with a catalytic surface. Reaction kinetics involving surfaces are generally slower than homogeneous solution reaction kinetics owing to geometric and mass transport considerations.[6] These "dimensional" factors can decrease surface reaction rates by orders of magnitude relative to solution reaction rates. Forward reactions that occur on a catalytic surface cannot sucessfully compete with the rapid back-reaction taking place in solution, therefore quantum efficiencies in heterogeneous artificial photosynthetic systems have generally been poor.

Charged macromolecular systems (micelles[7], vesicles[8], microemulsions[9], colloidal particles[10], inorganic clays,[11] and polyelectrolytes[12]) have been shown to improve the quantum yield of photoinduced electron-transfer reactions. The effectivness of macromolecules in decreasing back-reaction depends on the reaction system being studied and the experimental conditions. The addition of charged macromolecules to a reaction system such as is depicted in figure 1.1 acts to increase quantum yields by decreasing the rate of back reaction between the oppositely charged initial photoproducts $A^{-}\cdot$ and $P^{+}\cdot$. Electrostatic interactions between the highly charged macroion and the initial photoproducts decreases the chemical activity of the reactants participating in back-reaction, which decreases the liklihood of $A^{-}\cdot - P^{+}\cdot$

collision and subsequent back-electron transfer. If back-reaction is supressed to such an extent that the subsequent forward reaction of either $A^{-}\cdot$ or $P^{+}\cdot$ can compete sucessfully with the back-reaction, increased quantum yields are obtained.

Primary salt effects are responsible for the back-reaction rate reduction observed in macromolecular systems.[13] The chemical reactivity of oppositely charged species is decreased upon macroion addition owing to an increase in solution ionic strength. For simple dilute salt solutions, the effect of ionic strength on interionic reaction rate can be described using the Deybe-Hückel theory of electrolyte solutions[14] and the activated-complex theory of Brønsted.[15] The salt effect observed in macromolecular solution, however, is generally greater that that observed in simple salt solutions of comparable ionic strength. The high <u>local</u> ionic strength induced by the high charge density surrounding the macroion is believed to be responsible for the difference between simple salts and macroions.

In order to utilize macromolecules to decrease back-reaction rates in photoinduced electron transfer reaction systems, careful selection of the electrostatic charge of both the photosensitizer and electron acceptor is necessary to ensure that salt effects will act to selectively decrease the rate of back-reaction without significantly decreasing energy storing (forward) reaction rates.

Figure 1.2 shows a reaction system for which macroion-induced salt effects are expected to increase quantum yields. All of the experiments

reported in this thesis have been performed on this system.

Figure 1.2 Reaction Scheme Utilizing Charged Macromolecules

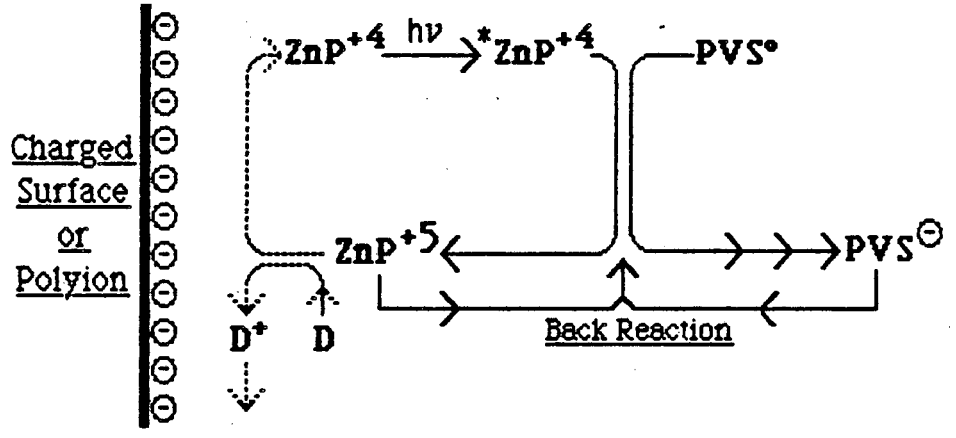

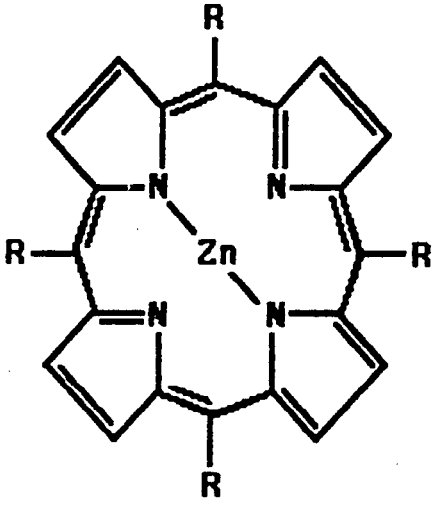

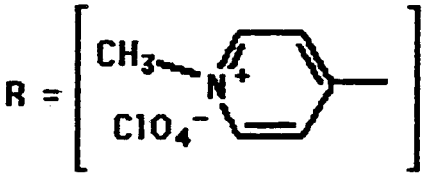

ZnP^{+4}

Zinc *meso*-tetra(4-N-methyl pyridinium) Porphyrin

Zinc tetra(4-N-methyl pyridinium) porphyrin (ZnP^{+4}) functions as the photosensitizer. It efficiently absorbs visible light, has a long-lived triplet excited state ($\tau_{1/2} \approx 3$ ms) from which electron transfer reactions can occur, and undergoes reversible redox reactions (E^0 = 1.2 V vs. NHE). The structure of ZnP^{+4} is shown above.

Propyl viologen sulfonate (PVS^0) is used as a reversible electron acceptor. PVS^0 is a neutral, zwitterionic species which becomes negatively charged upon accepting an electron from the photoexcited ZnP^{+4}. Reduced PVS^0 ($PVS^{-}\cdot$) is capable of reducing H^+ to $H_2(g)$ at neutral to acidic pH in the presence of a suitable redox catalyst. When no catalyst is present, the concentration of $PVS^{-}\cdot$ can be convieniently monitored spectrophotometrically ($\epsilon_{602} = 1.28 \times 10^4\ M^{-1}cm^{-1}$). The structure of PVS^0 is shown below.

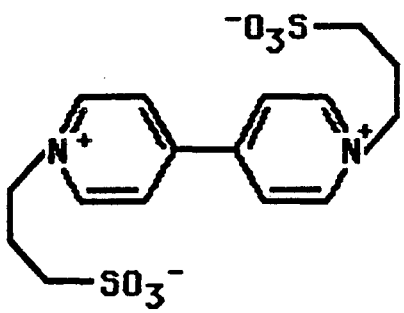

PVS^0
Propyl Viologen Sulfonate

Since an efficient catalytic system for O_2 generation has not yet been developed, sacrificial donors (D) such as EDTA, triethanolamine, or

cystine are used in continuous irradiation experiments to regenerate the oxidized photoproduct $ZnP^{+5\cdot}$ to ZnP^{+4}. The recycling of photosensitizer allows the buildup of $PVS^{-\cdot}$ to occur. $PVS^{-\cdot}$ can be convieniently monitored spectrophotometrically without resorting to time-resolved techniques. The quantum yield of $PVS^{-\cdot}$ buildup can be easily calculated by determining the moles of $PVS^{-\cdot}$ formed as a function of moles of photons (einsteins) absorbed by the photosensitizer.

By not including the H_2 generating catalyst and by using sacrifical electron donors, the reaction scheme depicted in figure 1.2 is simplified compared to the overall cyclic scheme shown in figure 1.1. This simplified reaction scheme has been developed in order to more easily study the effect of macromolecules on forward and back-reaction rates in photoinduced electron transfer reactions. The simplification allows the study of the kinetics of forward and back-reaction rates using flash photolysis and continuous photolysis experiments.

In time-resolved flash photolysis experiments both forward and back-reaction between initial photoproducts is measured. Transient absorbance changes can be monitored at different wavelengths, so the decay of inital excited state $^{3*}ZnP^{+4}$ or the buildup and decay of $PVS^{-\cdot}$ can be measured separately. Sacrificial donors are not used in flash photolysis experiments so that the back-reaction between the oxidized sensitizer and reduced acceptor does not compete with other reactions. This simplifies the kinetic analysis of the transient absorbance data obtained

The valencies of the reactants depicted in figure 1.2 have been chosen so that the salt effects of macromolecules can be used to decrease the rate of back-reaction between oxidized porphyrin ($ZnP^{+5}\cdot$) and reduced viologen ($PVS^{-}\cdot$). In the reaction scheme shown above, primary salt effect considerations lead to the prediction that salt effects on the forward electron transfer reaction between PVS° and ZnP^{+4} will be negligible, as this is an ion-molecule reaction. This implies that the forward reaction between ZnP^{+4} and PVS° will not be affected by the addition of macroions. The electron transfer reaction between the excited triplet state of ZnP^{+4} and PVS° results in the formation of initial photoproducts $ZnP^{+5}\cdot$ and $PVS^{-}\cdot$. Salt effect considerations lead to the prediction that the reaction rate between these oppositely charged species will decrease upon the addition of macroions.

Chapter 2 gives a detailed description of both flash photolysis and continuous irradiation experimental techniques which have been used to study these reactions. Both the instrumental characteristics and the operational techniques involved are described, so that future users of these home built instruments will have a convienient reference source. General experimental procedures concerning synthesis and purification techniques are also described in this chapter.

Chapters 3 and 4 describe experiments designed to study the effect of the polyelectrolyte poly(styrene sulfonate) (PSS) and other polyelectrolytes on the forward and back electron transfer reaction

between ZnP^{+4} and PVS°. Polyelectrolytes have been shown to have a profound influence on interionic reaction rates, increasing the rate of reaction between similarly charged species and decreasing the rate of reaction between oppositely charged species.[16] This so-called "polyelectrolyte "catalysis" [17] can be described in terms of kinetic salt effects, which change the activity of ionic reactants in the vicinity of highly charged macroions.

In addition to these electrostatic salt effects, hydrophobic (solvation) effects have also been shown to be important in determining how polyelectrolytes influence interionic reactions.[19] Hydrophobic interactions of reactive species with macromolecules may, in fact, be more important than electrostatic interactions, resulting in polyelectrolyte effects that are in complete disagreement with predictions based only on electrostatic salt effect considerations.

Flash photolysis experiments have shown that hydrophobic "envelopment" of ZnP^{+4} by poly(styrene sulfonate) (PSS) occurs upon addition of PSS to an aqueous solution of ZnP^{+4}. This envelopment leads to an unexpected decrease in both forward and back-reaction rates between ZnP^{+4} and PVS°. In continuous photolysis experiments, a slight increase in quantum efficiency is observed. This increase in yield, which is unexpected based on the flash photolysis results, is accounted for in terms of a polyelectrolyte-induced change in reaction rates of the sacrificial donor used in continuous photolysis experiments.

Chapter 5 describes experiments designed to probe the effect of

silica and alumina-modified silica negatively charged colliodal particles on the photoinduced electron transfer reaction between ZnP^{+4} and PVS°. Electrostatic interactions between the anionic photoproduct $PVS^{-\cdot}$ and the highly negatively charged silica surface significantly decreases the back-reaction rate between the photoproducts $PVS^{-\cdot}$ and $ZnP^{+5\cdot}$. Modification of the colloidal silica surface with Al^{+3} cations results in a significant increase in the acidity of the negative charges on the silica surface. Alumina modification of silica increases the pH range throughout which the colloid maintains its high surface charge density and resultant stability.

The effect of the mass transport and geometrical constraints imposed by anchoring one of the reactants to the surface of a colloidal particle [6] has been studied by looking at forward and back-reaction rates as a function of particle size. For the reaction system studied, the effect of particle size on rate has been found to be neglible in the particle diameter range of 6-22 nm. This result agrees with theoretical predictions that there should be be no express dependence of reaction rate on particle size for collision-controlled reactions.

1.3 References

1) Standard Oil Company of California, Econonmics Department, Report, "World Energy Outlook" (1983)

2) Briggs, C. K., Borg, I. Y., "U. S. Energy Flow-1984" Lawrence Livermore National Laboratory Report #UCID-19227-84, July 1, 1985

3) Johnston, H. J., Ann. Rev. Phys. Chem. 35, 481-505 (1984)

4) Arnon, D. I., Nitsui, A., Paneque, A. Science 134, 1425 (1961)

5) Kiwi, J., Kuppuswamy, K., Grätzel, Michael, "Structure and Bonding", Jørgensen, C. K. ed., Springer-Verlag, Berlin/Heidelberg (1982) Vol. 49, pp 37-125, (1981); b) Calvin, M., Accts. Chem. Res., 11, 369 (1978); c) Bolton, J. (ed.): Solar Power and Fuels, London, Academic Press 1977

6) Astumian, R. D., Schelly, Z. A., J. Am. Chem. Soc., 106, 304 (1984)

7) Fendler, J. H., Fendler, E. J. "Catalysis in Micellar and Macromolecular Systems", Academic Press, New York (1975)

8) a) Ford, William E., (1980) Dissertation (University of California, Berkeley, CA); b) Laane, C., Ford, W. E., Otvos, J. W., Calvin, M., Proc. Natl. Acad. Sci. USA, 78(4), 2017 (1981)

9) Atik, S., Thomas, J. K., J. Am. Chem. Soc., 105, 4515 (1983) and references therin

10) Willner, I., Yang, J. M., Laane, C., Otvos, J. W., Calvin, M., J. Phys. Chem., 85, 3277 (1981)

11) DellaGuardia, R. A., Thomas, J. K., J. Phys. Chem., 87, 990 (1983)

12) (a) Sassoon, R. E., Aizenshtat, Z., Rabani, J., J. Phys. Chem., 89(7), 1182 (1985); (b) Sassoon, R. E., Rabaini, J., Isr. J. Chem., 22(2), 138 (1982); (c)Myerstein, D., Rabani, J., Matheson, M. S., Meisel, D., J. Phys. Chem., 82, 1879 (1978)

13) Ise, N., in "Polyelectrolytes and Their Applications", Rembaum, A., Selegny, E., ed., Reidel, Dordrecht-Holland, (1975) pp 71-96.

14) Debye, P. J., Hückel, E., Physik. Z., 24, 185 (1923)

15) Brønsted, J. N., Z. Physik. Chem., 102, 169 (1922); 115, 337 (1925)

16) Morawetz, H., Acc. Chem. Res., 3, 354 (1970)

17) The term "polyelectrolyte catalysis" is a misnomer. True catalysts, according to Ostwald [18], influence forward and reverse reaction rates in the same proportion. This is not true for polyelectrolyte influenced reactions, which do not influence forward and back reaction rates equally. This is discussed in chapter 3.

18) Ostwald, W., Phys. Z., 3, 313 (1902)

19) Ise, N., Okubo, T., Kunugi, S, Acc. Chem. Res., 15, 171 (1982)

Chapter 2: Experimental Techniques

2.1 Synthesis and Purification of Reagents

Water is distilled and purified using a Millipore Milli-Q water treatment system. This system consists of an activated carbon cartridge, which removes organic impurities, and two ion exchange cartridges, which remove ionic impurities. A final filtration through a 0.45 um millipore filter to remove any particulate matter is also part of this system. Before water is removed from the milli-Q system it is allowed to circulate through the system for a few minutes, to allow any organic material which slowly leaches out of the ion exchange resin to be absorbed by the charcoal filter. The resistance of the purified water is typically <15MΩ/cm as measured by the resistivity meter incorporated into the milli-Q system. Triply-distilled water was used in some of the electrochemical experiments until it was discovered that the milli-Q water did not significantly increase the background currents measured in cyclic voltammetric experiments. Since low background currents are usually found only with highly purified solvents, it was judged that the millipore water was sufficiently pure for all photochemical and electrochemical experiments.

Triethanolamine, cysteine and sodium chloride were used without further purification.

The purification of polyelectrolytes and colloidal silica sols are

discussed in chapters 3 and 4, respectively.

2.1.1 Synthesis and Purification of Zinc tetrakis(4-N-Methylpyridinum)Porphyrin, Tetraperchlorate salt (ZnP^{+4})

Free base tetrapyridyl porphyrin was purchased from Strem and used without purification. Zinc tetrapyridyl porphyrin (ZnP) was prepared by the method of Alder,et al.[1] A stoichiometric amount (71 mg) of zinc acetate (Mallinkrodt, reagent grade) was added to 60 ml of refluxing dimethyl formamide (Mallinkrodt, reagent grade) containing 200 mg of free base tetrapyridyl porphyrin (Strem). This mixture was refluxed for 10 min. ≈30 ml of cold water was added to the reaction mixture and the mixture was concentrated using a rotary evaporator. 205 mg of precipitate was collected.

Methylation of ZnP to obtain the tetraiodide salt of ZnP^{+4} was performed by adding the 205 mg of ZnP prepared in the previous step to 25 ml of methyl iodide (Aldrich, reagent grade) and stirring overnight. The precipitate was collected and washed with $CHCl_3$ to remove any unmethylated starting material.

The tetraperchlorate salt of ZnP^{+4} was prepared by dissolving 293 mg of the tetraiodide salt of ZnP^{+4} prepared above in 1L of water, adding 100ml of 1M $NaClO_4$ and cooling overnight. The perchlorate salt of ZnP^{+4} precipitated from solution and was recovered by filtration. Elemental

Analysis: Calculated for $C_{44}H_{36}N_8O_{16}Cl_4Zn$: C, 46.36; H, 3.18; N, 9.83; Cl, 12.44; Zn, 5.73. Found: C, 47.32; H, 3.36; N, 10.04; Cl, 12.29; Zn, 5.80.

2.1.2 Synthesis of Propyl Viologen Sulfonate (PVS°)

1 g of 4,4'-dipyridine was heated together with 3 g of 1,3-propane sultone in a sealed vial for 20 h at 120 C. The white product was precipitated three times from water by the addition of acetone. Elemental analysis and NMR spectroscopy were used to determine the purity of the final product. The NMR spectrum of PVS° shown in Figure 2.1.1 was taken on the UCB-200 200 MHz NMR spectrometer using D_2O as solvent. Elemental analysis; calculated for $C_{16}H_{20}N_2O_6S_2 \cdot H_2O$ (MW=418): C, 45.92; H, 5.30: N, 6.69; S, 15.32. Found: C, 45.93; H, 4.58; N, 6.56; S, 14.86.

2.2 Laser Flash Photolysis Experiments

In flash photolysis experiments a sample is irradiated with a laser pulse and the transient absorbance behavior of the sample is monitored. The experimental apparatus for these experiments is shown in figure 2.2.1. A light pulse generated by a Candela SLL-66A flashlamp-pumped dye laser is directed into the sample compartment. Changes in absorbance are monitored by a single-beam spectrophotometer, which consists of a 75 W xenon arc light source and a monochromator or

Figure 2.1.1

NMR Spectrum of Propyl Viologen Sulfonate

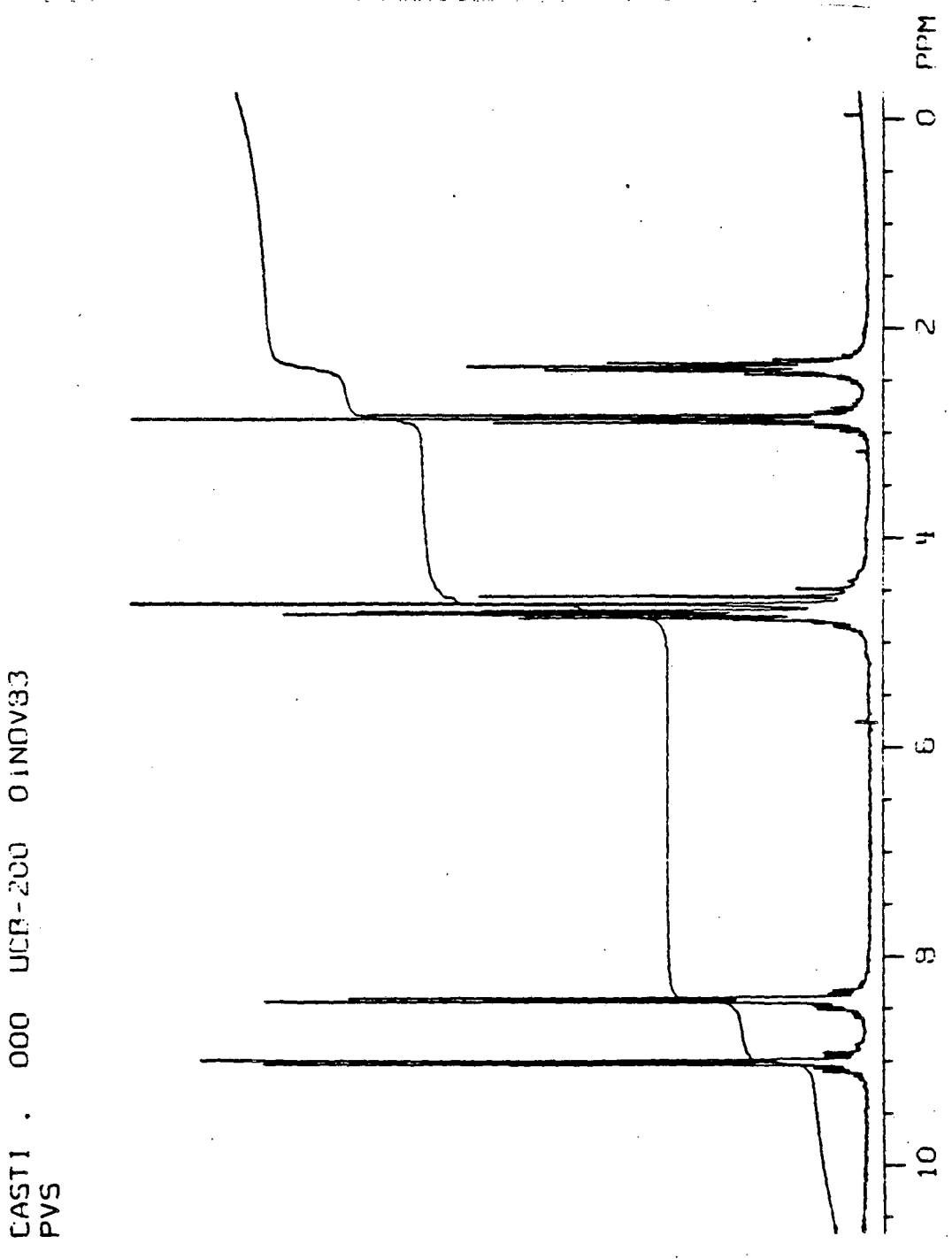

Figure 2.2.1

Flash Photolysis Spectrometer Schematic

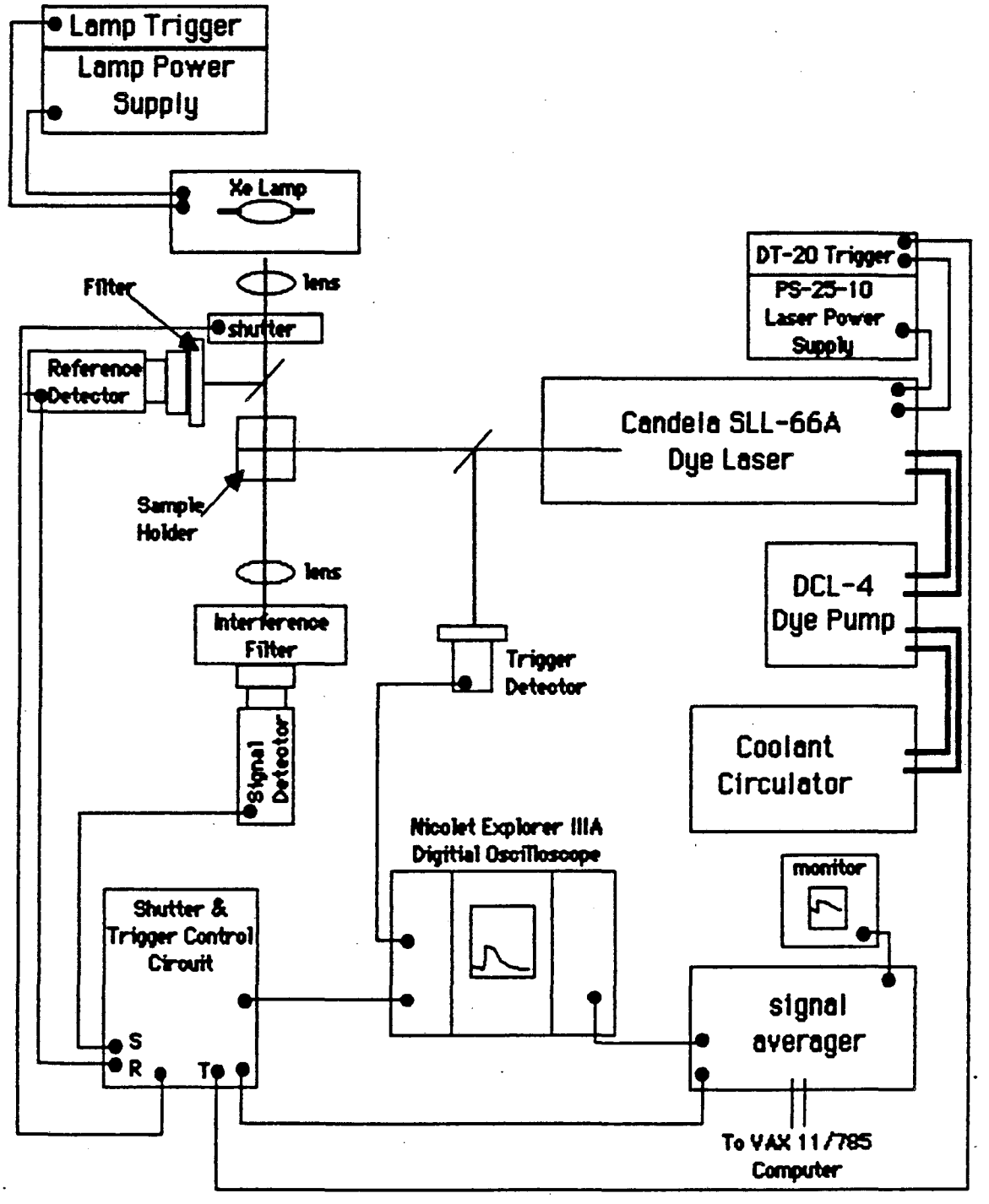

interference filter for wavelength discrimination.

Two fast photodiode detectors are used to monitor changes in intensity due to sample absorption (sample) and source intensity. A source detector monitors changes in lamp intensity, and a signal detector which monitors the change in intensity of light that is transmitted through the sample cell. The output from these two detectors is directed into a differential amplifier and subtracted. This removes the constant DC bias from the signal photodiode output voltage and corrects for any small changes in lamp intensity. The corrected output is digitized and displayed by a Nicolet digital oscilloscope. The digitized information is read by a signal averager unit (designed and built by Gary Smith). This unit collects and sums experimental time based data. The averaged data are then read by a Digital VAX 11/780 computer system for further data manipulation and storage.

Stored data are subsequently recalled and displayed on a graphics terminal which is linked to the VAX. The raw data (counts vs. channel number) are converted to absorbance change vs. time. Graphics and curve fitting methods are used to determine rate constants and other useful parameters.

The following section contains reference information and detailed operating procedures for the laser flash photolysis apparatus.

2.2.1 Candela SLL-66A Dye Laser

2.2.1.1 Operating Procedures

These procedures and suggestions in the following sections are based on the author's experience with this particular laser system. The reader is also referred to the manufacturer's operating manuals of the commercially available components, and to the Ph. D. thesis of J. M. Yang[2], who originally designed and assembled the flash photolysis system. Changes in design that have evolved during the four years since Yang's thesis are included here.

2.2.1.2 Safety Considerations:

Warning: Laser light is high intensity radiation and should always be regarded as dangerous. Laser goggles should be worn by all people in the laser room whenever there is a possibility that the laser could fire. Laser self firing is always a possibility, so goggles should be kept on until the high voltage is off and there is no possibility of the laser firing. The only laser goggles that are effective in blocking 590 nm light are Glendale Optical Co. double thickness LGS-R He-Ne goggles or broadband absorbing goggles, model # BG-1, avaliable from Fred Reed Optical Co., Albuquerque, NM.

High voltages (≈25 KV) are present in the laser housing during laser operation. These voltages are accessible when the laser is operated with the laser cover open. Another danger present when operating the laser

with the housing open is the possibility of exposure to UV light generated by the flashlamp and/or explosion of the flashlamp during laser operation. The necessity of operating the laser with the housing open has been largely eliminated by changes in the design of the laser system, which will be discussed in the following sections.

A fire hazard always exists during laser operation from the circulation of flammable dye solution through the laser housing/flashlamp. Provisions for flushing the laser compartment with N_2 gas have been made to reduce the possibility of fire. It is important to open the laser cavity and inspect for leaks while the dye is circulating before the laser is fired. Laser operators must know the locations of the nearest CO_2 fire extinguishers, and should be able to locate and turn off all the circuit breakers associated with the flash photolysis apparatus quickly in the event of a short circuit or fire.

2.2.1.3 Laser System Components

The laser system used in the flash photolysis apparatus is a Candela SLL-66A flashlamp-pumped dye laser, which consists of four integral components. The SLL-66 laser head contains the flashlamp, optics, spark gap and trigger transformer. The DT-20 control unit controls the safety interlocks and triggering circuitry. The PS-25-10 laser power supply controls the high voltage (25 KV) power delivered to

the spark gap. The DCL-4 dye circulation system provides for dye circulation, filtration and cooling. Modifications to the flash photolysis equipment have been performed over the past 4 years to improve performance and reliability. I am indebted to Mr. Richard Herrin of Candela for the valuable help he has given me during many telephone conversations in which we have discussed problems with the laser system.

2.2.1.4 Choice of Flashlamp

Three different laser flashlamp heads are available for the SLL-66A. The differences between these heads are the beam diameter (6 or 10 mm dia.) and the flashlamp configuration (triax or quadrax). Flashlamps with the triax configuration are cooled via dye circulation only, while quadrax lamps have separate coolant and dye circulation lines. The 10mm diameter triax lamp (Candela part #CL-50) is the preferred flashlamp for flash photolysis experiments. Installation and alignment is simplified because of the ruggedness of the larger diameter flashlamp. An additional advantage of using this lamp is that the10mm diameter beam width is ideal for irradiating 10mm path length sample cells. No beam expansion is necessary to completely irradiate the sample volume through which the probe beam passes.

The 10mm diameter flashlamp is only available in the triax configuration. For the repetition rate used in typical experiments using this system (≈.2 Hz), circulation of 15 C water coolant through the dye

solution during laser operation removes the excess heat generated by the flashlamp operation. If this heat is not removed the temperature of the dye solution slowly rises during the course of a series of experiments. Since the lasing efficiency of the dye decreases with increasing dye temperature, the performance of the laser system is degraded with time unless cooling is provided for. The temperature of the dye is maintained by circulating refrigerated (15 C) coolant (a glycol/water mixture) through a coil of 1/4" diameter aluminum pipe that is placed in in the laser dye reservoir in the dye circulating pump housing.

Nonuniformities in the laser beam energy are removed by homogenization of the beam as follows; The sample cells are used that have two polished and two ground glass (unpolished) sides. The unpolished sides of the cell face each other. The cell is placed in the flash apparatus so that the probe beam (used to monitor changes in absorbance) passes through the transparent sides of the cell. One of the unpolished sides is thus placed in between the cell contents and the incoming laser beam. The laser pulse is diffused and homogenized as it passes through the roughened surface, eliminating any nonuniformity in the beam profile. A small loss in beam power is observed when using frosted cells owing to back scattering from the frosted cell faces. These specially designed cells are shown in figure 2.2.2.

Figure 2.2.2

Design of Special Cells Used in Flash Photolysis Experiments

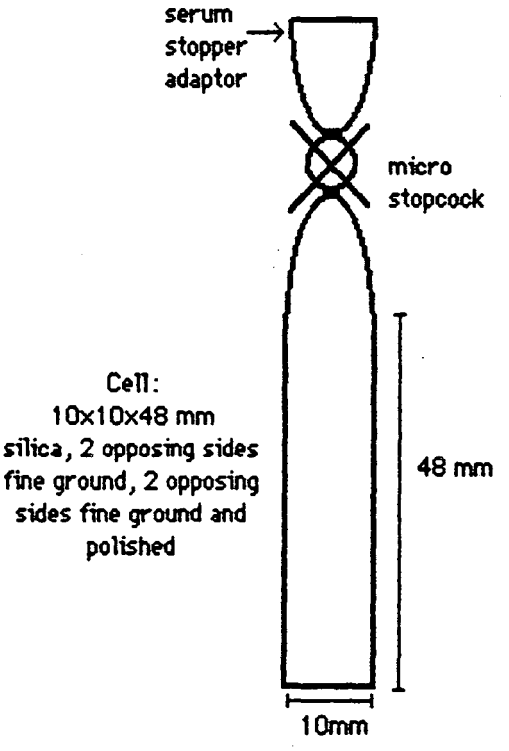

2.2.1.5 Choice of Laser Dye

The excitation source used in flash experiments is a Candela SLL-66-A flashlamp-pumped dye laser, which produces pulses in the far

UV and visible range of 150 nm duration (fwhm) at a maximum repetition rate of 0.5 Hz. The flash photolysis experiments described in this thesis were all performed using rhodamine 590 (rhodamine 6G) as the laser dye. This dye was chosen because of its superior lasing efficiency and because of the significant overlap of the emission of lasing rhodamine 590 with the absorption spectrum of the photosensitizer $ZnTMPyP^{+4}$.

The spectral overlap of rhodamine 590 with $ZnTMPyP^{+4}$ is an important consideration in the context of this work because $ZnTMPyP^{+4}$ is the only photosensitizer that has been used in the experiments reported in this thesis. Although the emission of some other laser dyes overlaps more efficiently with the absorption spectrum of $ZnTMPyP^{+4}$, rhodamine 590 is preferred because it lases efficiently and is easy to use. Rhodamine 590 is such an efficient laser dye that is frequently used by laser manufacturers as a "standard" dye solution to report operating specifications.

With the laser configured as described above, and with 5×10^{-5} M Rhodamine 590 in methanol, the maximum energy/pulse, as measured with a Scientech model #444 thermopile laser power meter is ≈0.25 J/pulse. Assuming the pulse consists entirely of 590 nm photons, the total moles of photons (einsteins) per pulse is estimated to be:

$$.25 \text{ joule/pulse} \times 4.93\times10^{-6} \text{ moles photons (590nm)/joule} = 1.23\times10^{-6} \text{ einsteins/pulse.}$$

This calculation will become important during the discussion of excited state extinction coefficients in section 2.2.5.1.

2.2.1.6 Laser Head Installation and Alignment

Laser head installation is a delicate operation. It is quite easy to break the flashlamp when connecting the dye circulation tubing. The flash tube in the lamp is pressurized with xenon gas. If the lamp breaks it is likely to explode. The danger of explosion makes it essential that protective goggles be worn during laser head installation and removal. The dye circulation tubing is attached to the flashlamp assembly before mounting the lamp in the housing so that any stress put on the lamp can be felt when tightening the hose fittings. If the lamp is secured to the laser housing before mounting, the application of excess stress might not be noticed, which could result in flashlamp breakage. Dye leakage is checked before securing the flashlamp in place by circulating dye solution through the flashlamp. Any fittings that leak are tightened before securing the lamp.

Once the fittings have been tightened and the new laser head is in place, it is aligned so that the axis of the flashlamp is parallel with the laser cavity. Dye is circulated through the flashlamp assembly during the alignment procedure to eliminate any bubbles in the flashlamp that might cause spurious reflections during alignment. A 0.5 mW He-Ne laser

(Spectra-Physics * 155) is used to align the laser head within the laser cavity. The exit slit of the alignment laser is covered with white tape and a 1mm pinhole is poked throught the tape to decrease the diameter of the alignment laser beam. This allows more accurate positioning of the optics. The entire spark gap assembly, which is attached to the flashlamp itself, is loosened in its mounting onto the laser housing, allowing the front window of the flashlamp to move about freely. Black plastic end caps are installed over the front and rear windows of the flashlamp. These caps facilitate the accurate positioning of the alignment laser beam through the center of the flashlamp.

The alignment laser is sighted through the center of the front mirror in the laser housing and the rear window of the flashlamp head. Careful adjusting of both the position of the flashlamp and the alignment laser is performed so that the alignment laser beam passes directly through the center of the flashlamp. Reflections of the aligning beam from the front and back mirrors are avoided at this time by adjusting the mirrors to deflect the reflections away from the flashlamp axis. When this procedure is completed, the spark gap is securely refastened in the laser housing.

Once flashlamp installation is completed, the front and back mirrors are aligned. The reflected image of the alignment laser beam from the mirrors is adjusted so that the reflections are directed back onto the exit slit on the alignment laser. The front mirror is adjusted first with the back mirror blocked. The back mirror is then unblocked and

aligned. The sign of good adjustment is the appearance of interference rings around the exit hole of the alignment laser. The mirrors are adjusted until the rings are completely symmetric around the exit hole of the alignment laser.

2.2.1.7 Laser Testing

Once the flashlamp and mirrors are aligned, the laser is test fired and adjusted for maximum beam and power. Beam homogeneity is tested by observing the burn pattern of the beam on unexposed, developed Polaroid prints. Adjustments are performed by making very small changes in the orientation of the rear mirror. Adjustment of the front mirror to further improve beam quality should are not recommended, as such adjustment usually results in a decrease in beam quality.

Remote back mirror adjustors are installed so that beam homogeneity can be changed while the laser housing cover is closed. This modification was necessary because beam homogeneity achieved by mirror adjustments performed with the laser housing cover open were consistently changed once the alignments performed with the laser housing cover open were consistently different than alignment with the cover closed. This modification has also decreased the hazards involved in operating the laser with the housing open. The risks of flashlamp explosion, contact with high voltage and UV radiation exposure have all been decreased considerably.

Typical burn patterns when using $5x10^{-5}$ M rhodamine 590 in EtOH are donut shaped holes that are more exposed on the outer perimeter of the hole than in the center. $5x10^{-5}$ M is the laser dye concentration recommended by the manufacturer. The operating instructions provided by Candela state that this kind of burn pattern indicates that the laser dye concentration is too high. Studies in this lab, however, have indicated that decreasing the dye concentration does not change the burn pattern significantly, but that it does result in a significantly lower peak laser power. These donut-shaped holes are only observed when using the 10mm diameter dye cell flashlamps. Beam non-homogeneity is not a significant problem in our experiments, however, since the beam is homogenized before it reaching the sample.

The condition and placement of the spark gap electrode is critical to the reliable operation of the laser. The electrode must be inspected frequently for signs of burning and arcing. A dirty electrode causes erratic laser firing. The electrode can be cleaned by grinding the surface of the electrode flat with a mechanical sander. After grinding, the electrode surface is cleaned and polished by sandblasting the surface. The mechanical sander and sandblaster are both available in the chemistry department machine shop. It is recommended that the spark gap electrode be sandblasted each time it is inspected in order to minimize the occurance of electrode damage. In addition to polishing the surface, sandblasting insures that the electrode will be clean and dry when replaced in the spark gap chamber.

When replacing the spark gap electrode, it is necessary to position the electrode tip flush with the inside surface of the spark gap end plate. If extensive grinding of the electrode has been performed, the side of the spark gap must be removed so that the electrode can be visually aligned with the inside surface of the spark gap end plate. Whenever the spark gap is disassembled, it should be thoroughly flushed with dry nitrogen gas prior to operation.

Spark gap pressure is also critical to reliable laser firing. The spark gap functions as a capacitor to store the charge to fire the flashlamp. If the pressure is too low, laser self-firing will occur. If the pressure is too high, the laser will not fire at all. Dry nitrogen is recommended for pressurizing the gap. The present setup uses a N_2 tank with an in-line Drierite™ canister for gas drying. A bleeder valve has been incorporated into the spark gap so that the N_2 in the gap is constantly flowing through the gap at a slow rate. This configuration allows the spark gap pressure to be monitored and adjusted using the pressure regulator on the nitrogen tank. Pressure adjustments can be performed during laser operation without having to turn off the high voltage or having to open up the laser housing cover.

A modification to the trigger transformer of the laser system has been performed to improve laser firing. The standard trigger transformer which was supplied with the SLL-66A has been replaced with a higher powered trigger transformer from a Candela SLL-500 laser. With this

modification, triggering of the laser is much more efficient at high spark gap pressures. The laser can now be consistently triggered while using significantly higher spark gap pressures. By being able to operate the laser using a higher spark gap pressure, laser misfiring is markedly reduced.

The modifications to the spark gap and triggering circuitry mentioned above have greatly reduced the occurance of laser misfiring. The sensitivity of laser triggering to spark gap pressure has also been reduced. Any spark gap pressure between 10 and 20 psi holds off laser self firing at moderate laser power supply voltages (20-23 KV). Optimum performance is obtained in the power range of 20-23 KV. At higher voltages (24-25 KV), slightly more pressure is needed to prevent self firing. At lower laser power (17-19 KV), less pressure is necessary in order to maintain consistent triggering.

The effect of laser voltage on pulse power is shown in figure 2.2.3

Figure 2.2.3

Effect of Laser Voltage on Laser Pulse Power

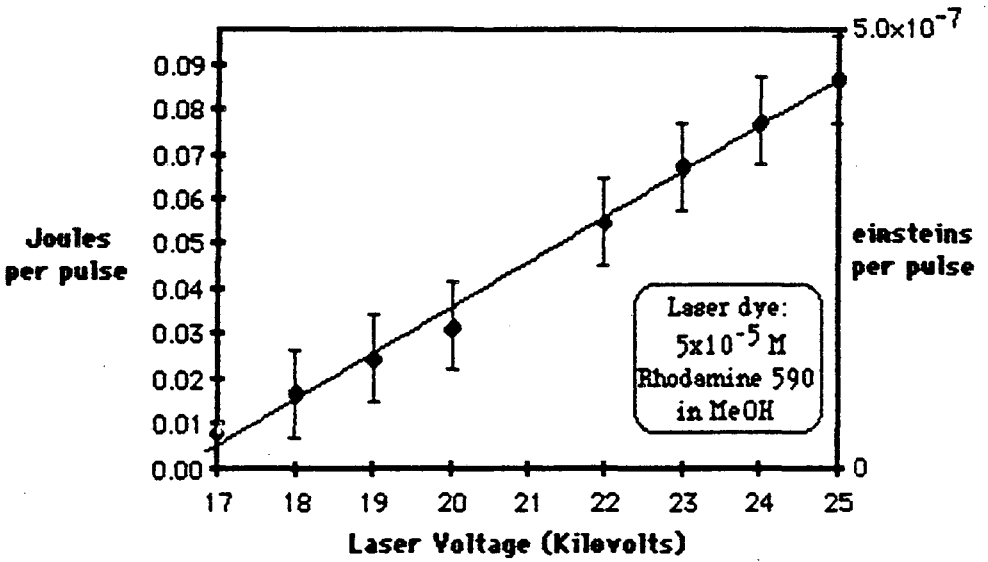

Laser power increases linearly with laser spark gap voltage. Pulse to pulse fluctuation of laser power is ≈0.02 joules/pulse, and is independent of the spark gap voltage. At lower laser voltage settings, however,this fluctuation is significant relative to the laser power, even if the spark gap pressure is adjusted for constant triggering. This fluctuation in laser power can have a significant effect on reaction rate determinations if the reaction kinetics depend on initial concentration excited state species. The recommended method of obtaining low power pulses with small relative power fluctuations is to operate the laser at ≈20 KV laser

voltage (or greater) and to decrease beam intensity using neutral density filters in the laser beam path., The fluctuation in beam intensity then decreases proportionally with beam intensity. The relative fluctuation in beam intensity, however, remains constant.

2.2.2 Transient Absorbance Spectrometer

Absorbance changes induced by the laser pulse are monitored with a single-beam spectrophotometer, which is shown in detail in figure 2.2.1. The following sections will outline the performance and operating procedures associated with the optics and signal detection components of the flash photolysis system.

All of the optical components shown in figure 2.2.1 are mounted on an Oriel precision benchtop optical platform to simplify the alignment procedure. This platform is in turn mounted on an Oriel optical table which provides vibrational stability for the entire apparatus. A 75 W xenon arc lamp is used as the probe beam source. Silica lenses collimate the output of the lamp and direct the beam through the sample compartment, which intersects the laser beam at right angles. Wavelength discrimination of the probe beam is focused onto either the entrance slit of an Oriel 7275 grating monochromator or through an Oriel narrow bandpass interference filter. The monochromatic light passing through the wavelength discriminator (filter or monochromator) is detected by a United Detector Technologies PIN-8-LC fast response photodiode. A beam

splitter partitions off a fraction of the probe beam into another fast photodiode detector which monitors source intensity and provides a baseline signal for background correction. An electromechanical shutter is placed between the probe beam source and the photolysis sample. The shutter is closed between laser pulses to minimize photolysis damage by the probe beam. Various filter holders are also placed in the probe beam for the placement of cutoff or attenuating filters. The characteristics of the individual components are discussed in greater detail in the following sections.

2.2.2.1 Probe Beam Source

A 75 W Xenon arc lamp (Xenon Corp, model K-1) is used as the probe beam source in this apparatus. The original power supply supplied by the manufacturer used two 12V rechargable automobile batteries as a constant voltage source. This power supply has been replaced due to problems with the battery recharging and lamp ignition systems. A Lambda model #LK 343A FM constant voltage power supply is being used in place of the battery system. A homebuilt lamp ignitor unit has replaced the original ignitor circuit that was in the battery operated lamp power supply.

Batteries were used as a DC voltage source in the original power supply to eliminate the AC voltage ripple present in most AC powered DC voltage supplies. The DC power supply now used in the flash photolysis

system was chosen because of its extremely low ripple voltage (<1mVAC), which is negligible as compared to the noise level of the system (≈20 $mVAC_{rms}$). The new power supply is considerably more reliable than the old battery system, and does not need to be recharged overnight before use. Long term voltage drift associated with battery discharge has been completely eliminated in converting to the AC powered voltage supply.

Igniting the probe beam lamp requires that both the lamp DC voltage supply and ignitor circuit be turned on for a few minutes before trying to ignite the lamp so that these circuits have a chance to warm up. The lamp is ignited by quickly pressing and releasing the ignitor button on the front of the ignitor circuit housing. This button should not be held down continuously, as doing so will damage the both the lamp and the triggering circuit. If the lamp does not ignite immediately, visually inspect the lamp to determine if a small arc has been struck across the triggering electrode and one of the main electrodes. If this has occured, as it often does if the lamp fails to ignite, the ignitor circuit must be switched off and on to stop the arcing. If repeated attempts to ignite the lamp fail, the lamp must be replaced. Note: Xenon arc lamps generate ozone, therefore adequate ventilation of the lamp must be provided for whenever the lamp is in operation.

2.2.2.2 Wavelength Discrimination: Monochromator vs. Interference Filters

In the experiments described in this thesis, wavelength discrimination has been performed using either Oriel 10 nm band pass (fwhm) interference filters or an Oriel 7420 grating monochromator. The use of interference filters increases the probe beam throughput compared to a monochromator, even if the monochromator slits are adjusted for a bandwidth comparable to the bandwidth of the interference filter. Most experiments have been performed using interference filters because of the increased sensitivity available due to the increased probe beam throughput. Excited state extinction coeffients are determined by performing excitation saturation experiments , which are discussed in section 2.2.5.1.

2.2.2.3 Time-Resolved Detection

Two fast phodiode detectors based on United Detector Technology PIN-8LC devices are used in the flash apparatus. Descriptions and circuit schematics of these detectors are included in J. M. Yang's thesis. [2] Originally both AC and DC coupled detectors were both used in flash experiments, the AC detector for short lived transients (≈100us) and the DC detector when monitoring longer lived species (≈1 sec). Risetime measurements were performed on the DC detector using a Berkeley

Nucleonics Corp. Model 6020 light pulse generator, which generates 5ns (fwhm) or longer visible light pulses. Response time of the DC detector as measured using the light pulse generator have shown that the response of the DC detector follows the rise of the light pulse, which indicates that the response time of the DC detector is better than 5 ns. Since the minimum time resoluton of the flash system is 50 ns (limited by the time resolution of the Nicolet digital oscilloscope), the DC detector can be used throughout the entire time domain of flash photolysis experiments possible with this instruments ranging from microseconds to seconds. Because of the limitation of the AC detector to short time ranges, it has not been used in any of the experiments discussed in this work.

2.2.2.4 Correction of Sample Detector Bias

When using the DC detector, changes in sample transmittance cause small changes in the intensity of light striking the sample detector. The fluctuation in light intensity causes a change in the photodiode current that is proportional to the change in light intensity. The photodiode current converted to voltage by a current-voltage converting circuit. The voltage is proportional to the photocurrent. The voltage flutuation induced by the change in light intensity is a small transient voltage that is superimposed on a large, constant DC bias voltage. This bias must be subtracted from the signal so that the small, transient voltage fluctuations can be accurately monitored.

A reference detector is mounted so that part the probe beam is split off into it before the beam strikes the sample. The reference detector monitors the intensity of the light beam before it reaches the sample, so changes in light intensity induced by absorbance changes in the sample do not effect the reference detector voltage. The reference detector is only sensitive to changes in the lamp intensity.

The constant output voltage from the reference detector is amplified and then subtracted from the sample detector voltage to back out the voltage bias in the sample detector output. This subtraction is performed by a high level signal processing circuit in the shutter and laser trigger control unit. A variable gain differential amplifier is used to vary the reference voltage that is subtracted from the signal voltage. A potentiometer on the front of the control unit is used to vary the amplifier gain. The gain is adjusted until the bias voltage is eliminated.

Setting the bias voltage potentiometer near the maximum reference signal gain should be avoided, as the preamp in the control unit induces an 60 Hz AC voltage ripple in the output when to potentiometer is turned up to maximum gain. If the sample bias is too high to be subtracted without inducing this ripple, neutral density filters should be placed in the probe beam to decrease the sample detector baseline voltage.

Additional control of the intensity of the reference signal is provided by a variable neutral density filter (Oriel part * 28600) which is placed in front of the reference detector. It is best to adjust the bias voltage to zero with this filter, rather than using the potentiometer on

the trigger and shutter control to adjust the differential amplifier gain. This helps to avoid the situation described above in which the bias subtraction amplifier in the trigger/shutter control induces an AC ripple in the bias-corrected signal.

Note: Short lived transients can be monitored by the oscilloscope directly without subtracting a bias voltage. The output of the sample detector can be input directly into the oscilloscope, i.e., the bias correcting circuit in the shutter/laser control can be removed from the detection circuit. In this configuration, the DC bias can be eliminated by setting the coupling switch on the signal channel of the oscilloscope tosignal scope to AC. When the scope is set this way the incoming signal is filtered trough a 1MΩ. 50pf RC circuit. In this mode the scope will filter out all of the DC components of the incoming signal. Because this filtering would seriously distort any transient signals with a rise (or decay) time of greater that 500μs, this method of bias correction can only be used on rapidly decaying signals. The advantage of this method over the subtraction method previously described is that this method eliminates the increase in noise that the sample signal picks up upon being modified by the bias correcting circuit in the shutter/laser control. A factor of 5 improvement in signal/noise can be realized by bypassing the bias correcting circuit.

2.2.2.5 Adjustment of Optics

In order to optimize the signal-to-noise ratio of the sample signal, the intensity of light striking the sample photodiode must be maximized. This is achieved by adjusting the positions of the lamp, lenses, detector and sample compartment. This maximization procedure is an iterative process, i.e., adjustment of one component changes the adjustment of all the rest. Small adjustments to each component should be performed in a cyclic pattern until the photovoltage (voltage difference between shutter closed and shutter open configurations) is a maximum.

2.2.2.6 Data Collection and Storage

This section describes the series of operations which must be performed in order to collect and store data. Once the user initiates data collection, a trigger signal fron the signal averager is sent to the trigger/shutter control. The following steps then occur in the order specified. The electromechanical shutter is opened to enable ΔI (t) measurement. A user-adjustable delay occurs between the opening of the shutter and the firing of the laser. The interval between these events is typically $\approx$1 s, but may be programmed to be as short as 200 ms. After the laser is fired and before the shutter closes, another variable time delay, (200 ms – 2 s) occurs to allow time for data collection to occur before the shutter closes.

Laser pulses are detected for oscilloscope triggering purposes by a photodetector mounted to receive scattered laser radiation from the mirror which directs the laser beam into the sample compartment (see figure 2.2.1). The output of this detector triggers the digital oscilloscope to begin collecting data. Once data collection is complete, the signal averager reads the data from the scope and sums it with previously collected data. This sequence of events is then repeated until a preset number of pulses are collected.

When data collection and averaging is completed, the data are read from the signal averager onto the VAX 11/780 computer system in the Calvin lab. Experimental information necessary for signal processing, i.e, number of pulses, photovoltage, time per point, etc., is also read into the data file containing the averaged transient data. This additional information is used to convert the raw data into absorbance vs. time data.

2.2.4 Experimental Procedure

This section details the exact procedures for performing flash photolysis experiments.

2.2.4.1 Startup

Before proceeding with startup, make sure the data acquisition software is up and running on the VAX, and that the link between the VAX

and the signal averager is in good working order. This is done by logging into the VAX, turning on the signal averager unit and running the data acquisition/retrieval program PHOTO2.COM in the Calvin group directory. Problems with data acquisition hardware and software should be brought to the attention of the VAX system operator. All of the instrumentation should then be turned on and allowed to come to operating temperature. This is especially necessary for the probe beam lamp, the dye circulation system and the dye coolant system.

2.2.4.2 Preparation of Laser

The laser cavity must be checked for dye leaks when the dye circulation system is first turned on. When the cavity is open for inspection the N_2 gas pressure in the spark gap should be turned on and adjusted to ≈15-20 PSI.

Once these inspections have been completed, the laser cavity door is closed and the cavity is flushed with N_2 gas for 10 min to minimize the danger of fire from a possible flashlamp explosion. Before the laser power is turned on, the probe beam throughput must be optimized in order to maximize the signal-to-noise ratio of the spectrometer.

Before the laser power is turned on, the door to the laser room should be closed. Users and observers present must be wearing laser safety goggles while the high voltage to the laser is on. With the laser

power set to ≈23 kV, the beam homogeneity is checked as oulined in 2.2.1.7, and adjusted until an even, circular spot is burned into a sheet of unexposed, developed Polaroid film. The laser beam is directed to irradiate the same volume of solution that the probe beam passes through. This is done by changing the orientation of the mirror which directs the laser beam into the sample compartment.

2.2.4.3 Optics and Electronics Adjustments

The controls on the front panel of the digital oscilloscope should be set as follows:

Storage Control: live

Trigger:

Mode:	Auto	Coupling:	DC
Cursor:	in	HF Reject:	norm
Lock:	out	Source:	Channel A (trigger detector input)
Slope:	out		
Coupling:	DC		

View:

Autocenter:	off	Expansion:	off (optional)
Memory	all	Function:	numeric reset
View:	Y/T		

The scope triggering is adjusted so that scattered laser light impinging on the trigger detector consistently triggers the oscilloscope when the laser fires. One of the input channels of the scope is used to observe the trigger detector signal. The other channel is used for the experimental signal.

Once consistent triggering is established, the correct bandpass interference filter is selected and placed in the probe beam. The photovoltage is now determined. Manual control of both the laser firing and shutter are obtained by setting the laser and shutter control switches located on the shutter/trigger control to the manual positions. With the shutter open, the bias voltage gain control and the variable neutral density filter in the reference detector beam are used to zero the signal voltage. It is very important to check that the scope crosshair used to set the zero is itself positioned at zero volts. Not setting the crosshair correctly will result in an incorrect determination of the photovoltage. Once the zero is set, the shutter is closed and the photovoltage is read as the difference in voltage between shutter open and shutter closed readings.

Volts full scale (VFS) is determined by test firing the laser (with the shutter open) and observing the resultant signal. The VFS is adjusted to utilize as much of the digitizing capability of the scope as possible, i.e., the VFS is adjusted to the minimum scale that will still show all the experimental data. Adjustment of the baseline to a point below 0 V usually allows a lower VFS setting. The constant baseline bias this induces is not a problem since it is corrected for later by the data

analysis software.

The time per point (TPP) and trigger position are set according the the speed of the rise and decay of the transient species that is being studied. The trigger position is the time cursor setting that determines how much time data collection is allowed to occur prior to the firing of the laser. It is set by moving the time cursor on the scope to the first data point in the field and using the scope reset button to set that time point to zero. Without triggering the scope, the cursor is then moved to the right using the cursor mover toggle switch on the scope until the desired trigger position time is reached. It is important that the scope triggering is set in the cursor mode so that laser triggering will coincide with the cursor time setting. The minimum allowable trigger position is determined by the data analysis software, which presently uses the average of the first 200 data points to determine a baseline to subtract from all data points in the set. This operation sets the absorbance change before laser firing to zero.

It is important to set the trigger position so that the laser does not fire during the collection of the first 200 data points. A convienient setting for the trigger position is 1000 times the TPP, i.e., when using a 5 us TPP, the trigger position would be set to 5 ms. Note: The trigger position changes whenever the cursor is moved, so it is important to always move the cursor back to the correct setting if it is changed for any reason during an experimental run.

2.2.4.4 Data Collection and Storage

Once the above procedures have been completed, data collection can begin. The three switches on the trigger/shutter control should be set to the automatic operation position, and the delay time potentiometers adjusted for the maximum time between pulses. This adjustment is performed by turning both delay control potentiometers to the fully clockwise position and pressing both of the time selector buttons so that a 2 s delay time is indicated. If the limit light appears after performing this operation, open and close the front panel shutter and trigger control switches. This will usually remove the limit indication.

To begin data collection, press the reset button on the signal averager. A message on the signal averager monitor will read:

CAL SYSTEM SIGNAL AVERAGER
NUMBER OF SHOTS?

Enter the number of shots that the signal averager should collect by punching the keys on the signal averager unit and the "E" (enter) key. If an error is made in entry, the "D" (delete) key can be used to remove the incorrect number as long as the "E" key has not been punched.

The signal averager will respond "READY TO START". To begin data collection, press the start button.

Data collection can be temporarily halted using the pause button.

Changing the number shots per run is accomplished by first pausing and then pressing the change button.

Note: The signal-to-noise ratio (s/n) increases as the square root of the number of shots. This means, for example, that changing the number of pulses collected from 10 to 20 only results in a factor of 0.707 decrease in s/n. Clearly, increasing the number of pulses to more than ≈50 only leads to a small relative increase in s/n unless a very large number of pulses are collected. Damage to the sample by the laser pulses must be considered when signal averaging for long periods of time.

Once data collection is complete, the averaged data are read by the VAX for further manipulation and long-term storage. The data acquisition and manipulation software is accessed by running the program PHOTO2.COM, located in the Calvin group directory on the Biodynamics Division VAX. This program prompts the user to enter all the experimental parameters which are needed to process the raw data into transient absorbance data. This program is also used to recall and view the experimental data. The program can edit, smooth, display and curve fit the data. The next section describes the routines used to transform the raw data into absorbance data.

2.2.4.5 Data Manipulation

In a flash experiment, a laser induced changes in the absorption of light by the sample cause a change in the intensity of light striking the sample photodiode. Since the output voltage of the photodiode is linear with light intensity, the change in photodiode voltage (ΔV) is directly proportional to the change in sample transmittance (ΔI). The relationship between ΔV and ΔA and the data manipulation techniques necessary to calculate ΔA are outlined below.

2.2.4.5.1 Transformation of Raw Data

Experimental data read into the VAX from the signal averager are stored in CALDAF files in the directory named [CALEXPLIB.AVERAGER]. The basic structure of the data file is such that header information necessary for signal processing is included in the beginning of the file. The actual experimental data are stored in an 4096 x 4096 array after the header information. This raw data are read by the data manipulation program and transformed into signal (counts) vs. channel number. Channel number is converted to time by multiplying the channel number by the time per point. The trigger position is used to set the zero of time to the time when the laser fired.

Signal (counts) are converted to absorbance by a two step process. The counts are normalized by subtracting the average of the first 200

points from all of the data points. This sets the count value of the data before the laser pulse to zero. Counts are converted to voltage by performing the following operation:

$V(t) = (count) \times VFS/4096$

Where VFS = volts full scale setting used in experiments, and 4096 = total number of channels used in data acquisition.

Absorbance changes are calculated using the following formula:

$$\Delta A = A(t) - A(t=0)$$

$$A(t) = -\log(I(t)/I_0)$$

$$A(t=0) = -\log(I(t=0)/I_0)$$

Because of the additive property of logarithms, i.e., log(A/B)= log(A)-log(B), the above expressions can be combined to give:

$$\Delta A = -\log(I(t)/I(t=0)) = -\log(V(t)/V(t=0))$$

Note that I_0 has been eliminated from this expression. Since transmittance and voltage are directly proportional in this situation, the result can be expressed in terms of voltage:

$\Delta A = -\log(V(t)/PV)$ where PV = photovoltage = $V(t=0)$ = the signal detector voltage at t=0. The photovoltage is determined by measuring the signal detector voltage when the shutter is closed and subtracting the voltage reading obtained when the shutter is opened.

The advantage of measuring ΔA over measuring absolute absorbance is that a small ΔA superimposed on a large absorbance can be accurately detected as long as the sample absorbance does not attenuate the probe

beam too much. When the sample absorbance is large, the accuracy of the photovoltage determination is limited by the instrumental noise. When interference filters are used for wavelength discrimination, this limit is reached when the sample absorbance is ≈2.

2.2.4.5.2 Signal-to -noise ratio

The noise levels associated with the PIN-8-LC photodetectors and related current-voltage conversion circuitry is ≈10 mV RMS. Superimposed on this background noise is an ≈2.5 mV rms, 60Hz multicomponent AC signal which originates from the high level signal processing circuit in the trigger/shutter control. When the differential amplifier of the bias subtracting amplifier is used at full gain, this AC component increases in intensity to ≈8 mV. It is possible to minimize this AC noise by avoiding using the bias subtracting amplifier at full gain. By decreasing the sample beam intensity with neutral density filters, it is usually possible to eliminate the need to use the high-gain settings of the bias-correcting amplifier.

Signal-to-noise ratios for transient absorbance measurements (typical photovoltage = 1.5V) $\Delta I(noise)/I$ = .005V/1.5V = .0033 (0.33%). This corresponds to a ΔA error of .0015 absorbance units.

2.2.5 Specific Experimental Procedures

2.2.5.1 Determination of Excited State Extinction Coefficients

Kinetic analysis of experimental data depends upon the accurate determination of the concentrations of reactants and products. Transient absorbance experiments thus depend upon the knowledge of the extinction coeffients (ϵ_λ) of the absorbing species present in the reaction system. In most cases these can be determined simply by determining the absorbance of a stock solution of known concentration and using Beer's law ($A=\epsilon_\lambda lC$). Short lived species ϵ_λ's cannot be determined in this way; the use of time-resolved techniques is necessary.

Excited state ϵ_λ's are measured by performing an excitation saturation experiment. A sample with an unknown extinction coefficient is pulsed with laser light into an excited electronic state. If the laser power is sufficient to excite 100% of the ground state species into its excited state, the change in absorbance is proportional to the difference in extinction between the ground and excited states. The excited state extinction coefficient is calculated from the following equation:

$$\Delta\epsilon_\lambda = \epsilon_{\lambda(\text{ex. state})} - \epsilon_{\lambda(\text{gnd. state})} = \Delta A_{\lambda(t=0)} / C_b$$

$\epsilon_{\lambda(\text{gnd. state})}$ = extinction coefficient of ground state

$\Delta A_{\lambda(t=0)}$ = maximum absorbance change (occurs at t=0)

C_b = concentration of ground state before flash

This method depends upon 100% conversion of the ground state to the excited state. Excitation saturation is obtained by increasing laser pulse power until no further increase in $\Delta A_{\lambda(t=0)}$ is observed.

This method has been used to determine the excited state triplet extinction coefficient of ZnP^{+4} in deoxygenated water solution. A 1×10^{-5} M degassed solution of ZnP^{+4} was pulsed with 590 nm light, and the initial absorbance change at 480 nm was monitored as a function of laser power. The effect of laser power on $\Delta A_{480(t=0)}$ is shown in figure 2.2.4. Saturation of the sample does not occur completely, but $\Delta A_{480(t=0)}$ asymtotically approaches a limiting value of ≈ 0.28 , which corresponds to a $\Delta\epsilon_{480}$ of $2.8 \times 10^5\ M^{-1}\ cm^{-1}$.

Figure 2.2.4

Effect of Laser Power on Initial Absorbance Change at 480 nm

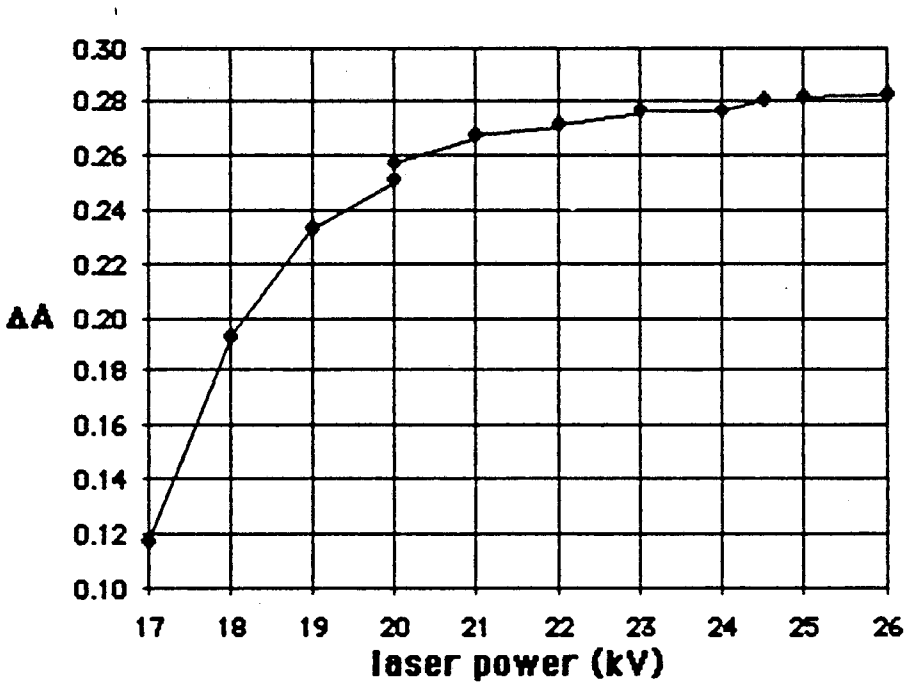

1×10^{-5} M ZnP^{+4} in H_2O, degassed by argon bubbling.

2.2.5.2 Determination of Oxygen Concentration in ZnP^{+4} Samples Using Excited-State Quenching Methods

Quenching of excited triplet state aromatic molecules by oxygen is a well known phenomenon.[3] The presence of oxygen in flash photolysis samples was first suspected when the apparent triplet state lifetime of ZnP^{+4} was observed to increase upon exposing the sample to either laser light or sunlight. It was thought that exposure of the samples to light scavenged the samples of residual dissolved oxygen through some kind of photoprocess. The argon-bubbling technique used to purge flash samples of oxygen is discussed in section 4.2.3.2. While this technique is not as efficient as freeze-pump-thaw techniques normally used, sample sensitivity to freezing precluded use of the more efficient method.

In order to determine the quenching rate constant and absolute concentration of oxygen in argon-bubbled solutions, triplet excited-state ZnP^{+4} lifetime measurements were performed on solutions containing varying concentrations of added oxygen.

$^{3*}ZnP^{+4}$ decay in flash photolysis experiments can be modeled by the following differential equation:

$$d[^{3*}ZnP^{+4}]/dt = (k_{uni} + k_{O_2}[O_2] + k_{qi}[Q]_i)\,[^{3*}ZnP^{+4}]$$

where k_{uni} (s^{-1}) is the unimolecular triplet decay rate constant, k_{O_2}

($M^{-1}s^{-1}$) is the bimolecular oxygen quenching rate constant, and k_{qi} and $[Q]_i$ are the rate constants and concentrations, respectively, of any other excited state quenchers in solution. Triplet-triplet and triplet-ground state quenching also occur in ZnP^{+4} solution, but these reactions are not significant in dilute solutions such as were used in this study.

Oxygen quenching can be treated a pseudo-first order reaction rate since the vibrational excitation transferred to oxygen from $^{3*}ZnP^{+4}$ during the quenching process is rapidly removed from the excited oxygen through collisions with solvent molecules. Even if the concentration of oxygen is less than that of $^{3*}ZnP^{+4}$, quenching of $^{3*}ZnP^{+4}$ by oxygen does not deplete the concentration of oxygen, therefore pseudo-first order kinetics apply.

Rate constants are determined by the following method: The initial slope of a ΔA vs. t plot is normalized by dividing by the initial $^{3*}ZnP^{+4}$ concentration. Typically the first 300 μs of data from a 15 ms decay curve are sufficiently linear to reliably determine the initial slope. The normalized slope is plotted as a function of the added oxygen concentration. According to the kinetic scheme outlined in equation 1 above, rate/$[^{3*}ZnP^{+4}]$ vs. $[O_2]$ plots should be linear with a slope of k_{O_2}.

In order to determine the oxygen concentration in degassed samples, the trace oxygen is removed by exposing the degassed sample to sunlight for brief (10 min) intervals until no further increase in excited state lifetime is observed upon further illumination. Assuming all trace

oxygen has been photoreacted, the normalized slope for the oxygen-free solution is equal to k_{uni}. Once both k_{uni} and k_{O_2} are determined, the trace oxygen concentration in the degassed sample (before oxygen addition) is determined from the normalized slope of the sample containing no added oxygen.

The experimental procedure described above was performed on 3 ml samples of 1×10^{-5} M ZnP^{+4} solutions degassed by 30 min of argon bubbling in anerobic flash photolysis cells with a total volume of ≈5.5 ml. Oxygen addition was performed by injecting aliquots of air-saturated water followed by vigorous shaking. Injections of air-saturated water proved to be much more reproducible than air injections. The calculation of the concentration of oxygen in the liquid phase of the photolysis sample was based on the solubility of oxygen in water [4] and the volume of liquid and gas in the sample cell. At 20 C and 25 C, the concentration of oxygen in air saturated water is 0.276 μmoles/ml and 0.253 μmoles/ml, respectively.

Table 2.2.1 lists the calculated concentration of oxygen and the values of the normalized slope of ΔA vs. t plots for a $[ZnP^{+4}]=1\times10^{-5}$ M .

The data in table 2.2.1 are plotted and the least square fit to a straight line is shown in figure 2.2.5. The correlation coefficient of the fit is 0.993 The slope of the fitted line gives k_{O_2} as determined by the slope of the fitted line is 1.29×10^{9} $M^{-1}s^{-1}$. The Y-intercept of the fit gives k_{uni}, which is 317 s^{-1}. The concentration of residual oxygen in the

degassed sample before irradiation is calculated by using k_{O_2} and k_{uni} in the rate equation above. $[O_2]_{liquid}$ was determined to be $(635-317)s^{-1}/1.38\times10^{9}\ M^{-1}s^{-1} = 2.3\times10^{-7}$ M.

Table 2.2.1

Kinetic Data Used to Calculate Oxygen Quenching Rate and Concentration in Argon-Bubbled Degassed Solutions

µL air-sat'd water added	$[O_2]$ added $M/10^{-7}$	slope/$[^{3*}ZnP^{+4}]$ s^{-1}	
0	0	635(±10%)	degassed, but contains trace $[O_2]$
0	0	317	trace O_2 removed by sunlight irradiation
10	0.46 (±0.05)	431	
20	0.92	470	
50	2.33	640	
100	4.68	935	
150	7.44	1220	
200	10.2	1730	
250	13.2	2220	
300	16.4	2330	

Experiments performed at 20 C. $[O_2]_{liquid}$ calculated using published values for the oxygen content of air-saturated water at 20 C (0.276 µmoles/ml).[4]

Figure 2.2.5
Effect of Oxygen addition on the Excited State Triplet Lifetime of ZnP^{+4}: Determination of Residual Oxygen Concentration and and k_{O_2}

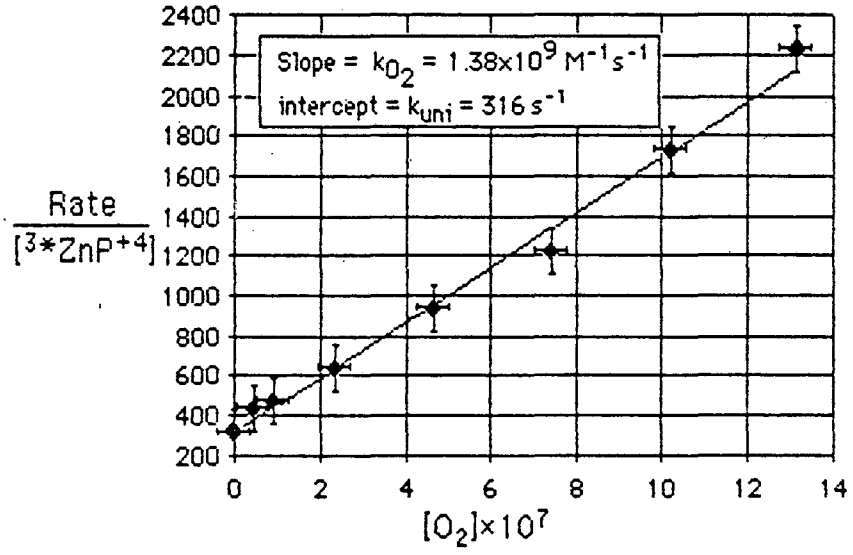

Rate = $-d[^3*ZnP^{+4}]/dt$ at t=0 determined by laser flash photolysis of 1×10^{-5} M ZnP^{+4} solution. Oxygen concentration was varied by serial additions of oxygen-saturated water.

2.3 Continuous Photolysis Experiments

This section describes the design and construction of a continuous photolysis apparatus which is used to perform continuous photolysis experiments. These experiments are performed by continuously irradiating a stirred sample with visible light from a 450 W xenon lamp. The actinic light is directed through a fiber optics cable and impinges on the sample. A specially designed cell holder is used to hold the irradiated sample in the cell compartment of a Hewlett-Packard 8450A UV/visible spectrophotometer. This allows for simultaneous irradiation and spectrophotometric monitoring of the sample.

The use of this specially designed cell holder in conjunction with chemical and/or thermopile actinometery allows changes in sample absorbance to be monitored as a function of the number of photons absorbed by the sample. Provisions for sample stirring and temperature control are included in the design of the cell holder. Integration of both irradiation and detection capability into the same cell holder in conjunction with the rapid data acquisition and storage of spectral data using the HP 8450 make spectral data collection as rapidly as one complete spectrum every 2 seconds possible.

2.3.1 Design and Construction

2.3.1.1 Actinic Source and Fiber Optics Connection

Figure 2.3.1 shows the assembly used to direct light into the sample holder. Actinic radiation from a 450 W xenon lamp is focused by a collimating lens into an Oriel model #6194 water filter, which is mounted onto the lens assembly with a specially designed adaptor. The water filter absorbs the IR radiation of the beam, which reduces the heat load on optical components along the light path. The IR filtered beam is directed through a manual shutter (Oriel #7143), an adjustable diaphram (Oriel #6203) and an Oriel narrow bandpass interference filter. This filter is used for wavelength selection. A specially designed fiber optics collimator lens (Oriel #77800) focuses the filtered beam onto the end of an Oriel model #77525, 36 in. long, 0.125 in diameter silica fiber optics cable. The silica fiber optics cable transmits approximately 60% of the visible light (λ>350 nm).

2.3.1.2 Cell Holder Assembly

The fiber optics cable delivers the filtered light beam into a specially designed cell holder, shown in figure 2.3.2. This cell holder fits into the sample compartment of an HP 8450A diode array spectrophotometer. The actinic beam is perpindicular to the spectrophotometer probe beam. The fiber optics cable is butted up against

Figure 2.3.1
Light Input Assembly for
Continuous Photolysis Apparatus

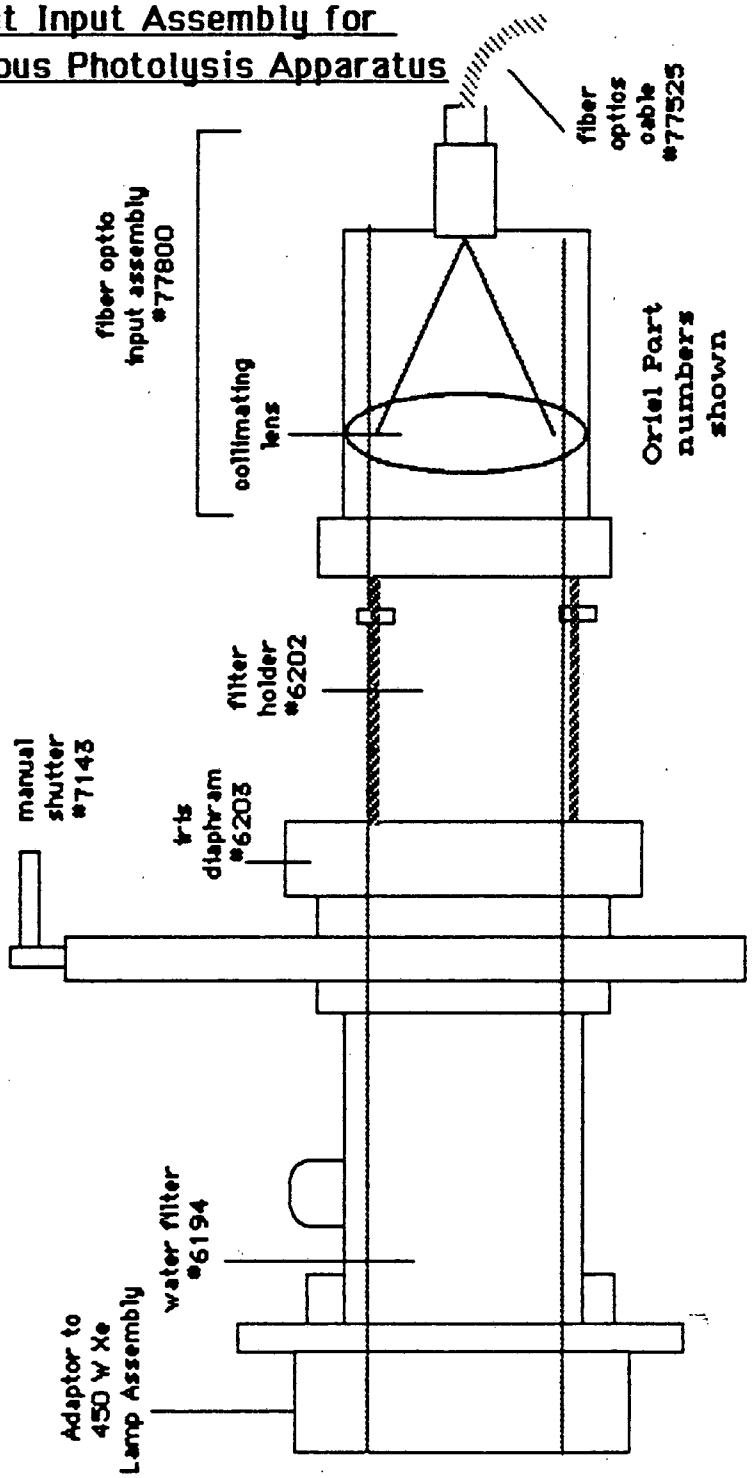

Figure 2.3.2
Cell Holder Assembly for Continuous Photolysis Experiments

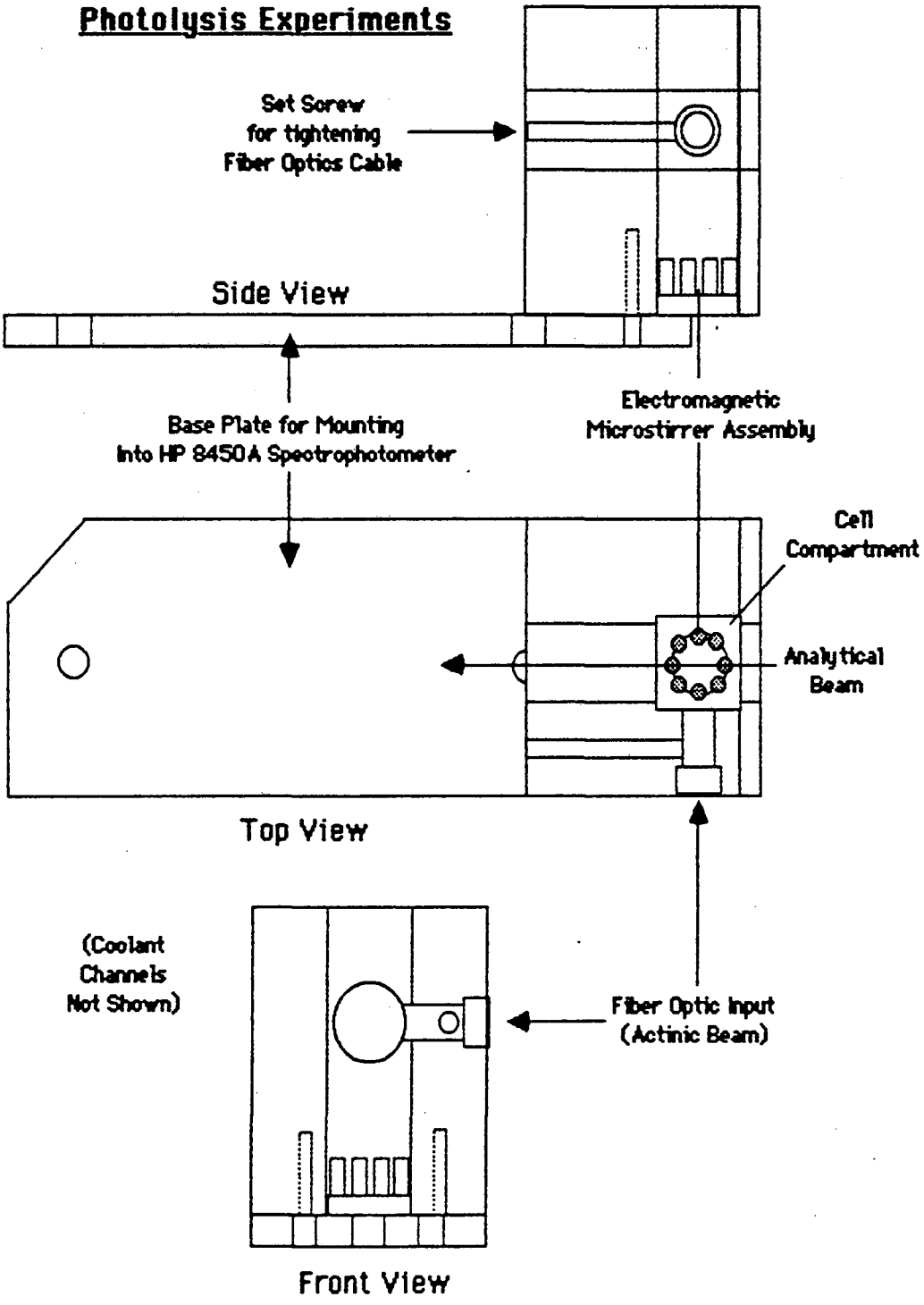

the side of the sample cell and tightened in place with the set screw. This secures the cell in place during irradiation experiments.

The cell holder temperature is controlled by the circulation of water/ethylene glycol coolant through channels that have been incorporated into the main body of the cell holder assembly. The range of temperatures obtainable using this cooling system is limited by the cooling capacity of the coolant circulating system and/or the freezing/boiling points of the coolant used. At temperatures significantly lower that freezing, condensation of moisture on the sample cell surfaces interferes with the measurement of absorbance changes with time. A stream of dry N_2 gas must be used to keep the cell windows free of moisture when performing experiments below room temperature.

Sample irradiation is not uniform throughout the sample volume, so sample stirring is provided so that absorbance measurements will give a quantitative analysis of reaction kinetics. An electromagnetic stirrer is incorporated into the bottom of the cell holder assembly. Current pulses are driven through the electromagnets using a specially designed microstirrer controller. The circuit diagram for the stirrer controller is shown schematically in figure 2.3.3. These current pulses are sequenced to cause the rotation of a teflon covered magnetic stirbar in the sample cell.

2.3.1.3 Design of Continuous Photolysis Cell

Continuous photolysis experiments are performed under oxygen-free conditions using specially designed gastight fluorimeter cells equipped with magnetic stirbars. Two different designs have been used, which are both shown in figure 2.3.4. While both cells are gastight, the two piece cell is easier to clean since it can be disassembled for easy access to the stirbar and inside cell surfaces. Sample degassing is performed by bubbling deoxygenated argon gas through the sample solution for 30 minutes. The circuit diagram for the stirrer controller is shown in Figure 2.3.3.

Argon is deoxygenated by passing the gas stream through a 2cm diameter by 0.5 meter long column containing activated BASF copper on carbon catalyst pellets heated to 150 C. After the gas has passed through the catalyst column, it is bubbled through distilled H_2O to saturate the gas in water vapor so that deoxygenation of the sample solution does not cause sample evaporation.The catalyst pellets are periodically inspected for O_2 saturation (indicated by a change in color from black to greenish-black) and regenerated by passing H_2 gas through the heated column for 30 min.

Oxygen concentration in degassed samples has been determined to be $\approx 2 \times 10^{-7}$ M by excited state O_2 quenching experiments. These experinments are described in section 2.2.5.2.

Figure 2.3.3.

Circuit Diagram for Stirrer Controller Used in Continuous Photolysis Apparatus

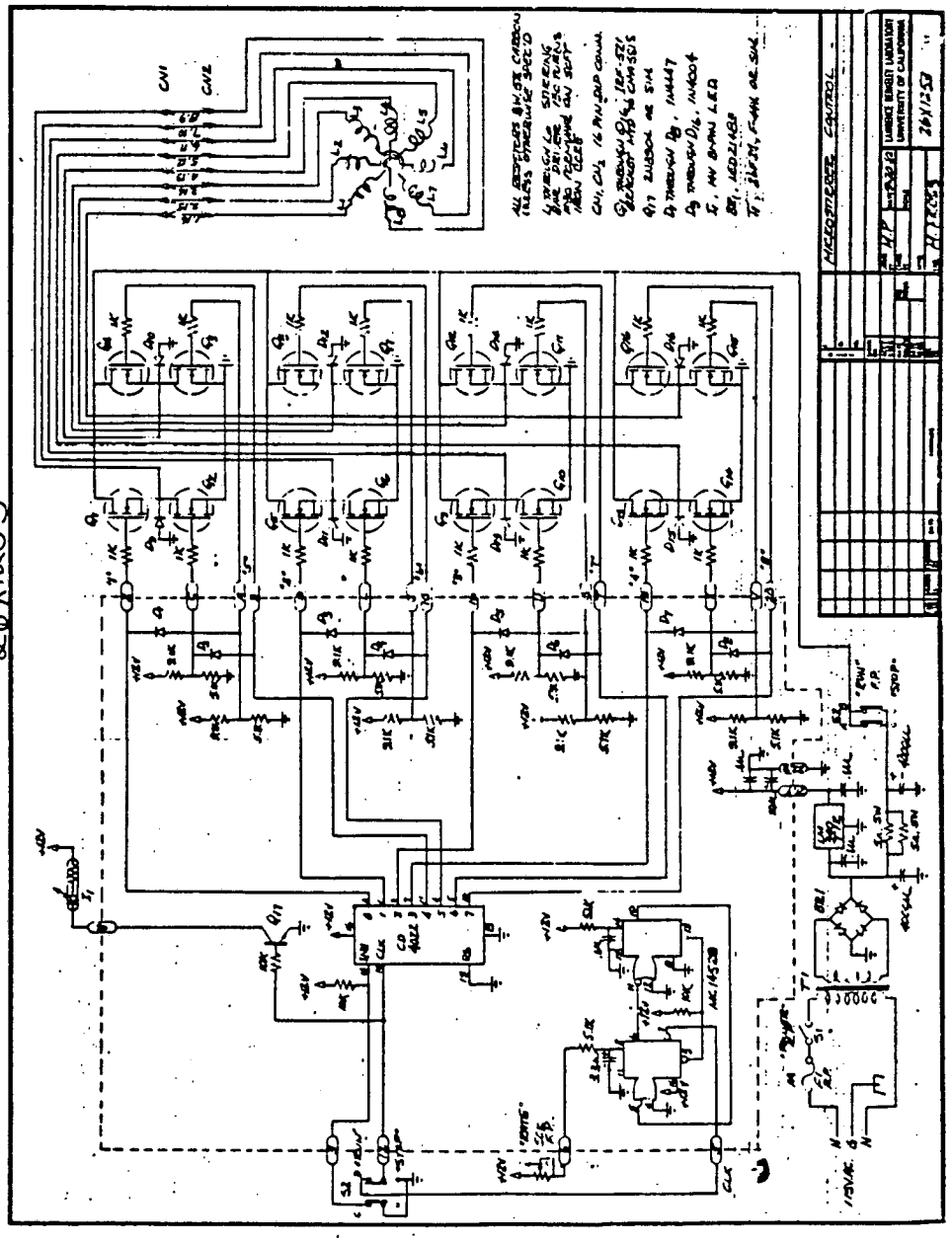

Figure 2.3.4

Continuous Photolysis Cell Design

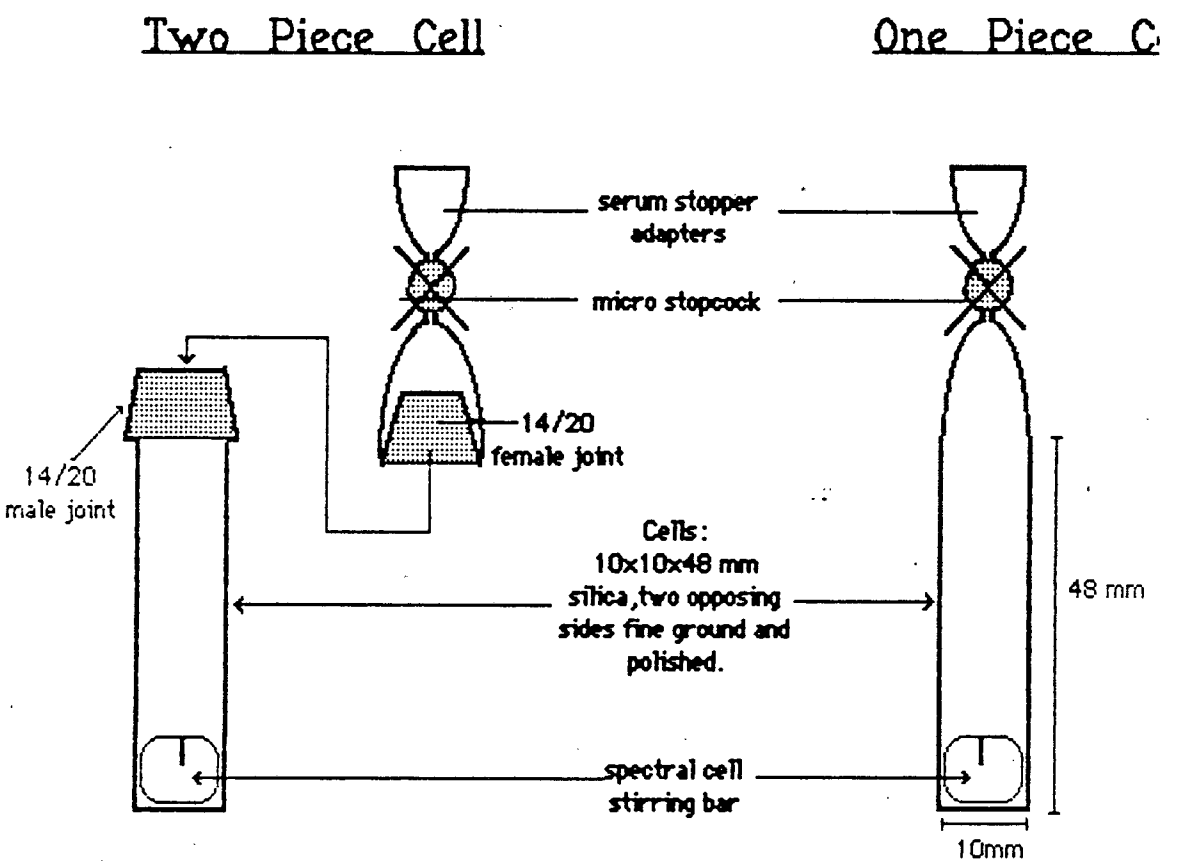

2.3.2 Experimental Procedure

In a typical continuous photolysis experiment the aqueous sample that is irradiated contains a photsensitizer,ZnTMPyP^{+4}, a reversible electron donor, PVS° ,and an irreversible electron donor , Cysteine, TEA or EDTA. These components are placed in the specially designed cell described above and degassed by argon bubbling for a minimum of 30 minutes. The cell is placed in the holder and secured by pressing the fiber optics cable end against the cell and tightening the set screw which holds the cable in place in the holder. The holder assembly is placed in the sample beam path of the HP 8450 spectrophotometer. Sample stirring is initiated, and temperature equilibration occurs between the cell contents the holder. Usually the sample is photoreactive, so a black cloth is draped over the sample holder to block out room light (the cloth must not block the spectrometer beam paths). The photolysis experiment is initiated by simultaneously opening the shutter in the actinic beam and beginning the data acquisition routines of the spectrophotometer.

2.3.2.1 Data Storage

In experimental run in which more than ≈10 spectra will be measured, the absrobance data must be stored onto floppy disks during the run. The microfloppy disk drive attached to the spectrometer is capable of storing up to 150 full spectra per disk. The spectrometer can measured

and store spectra in consecutively numbered files on the floppy disk. A complete description of the methods of operation of the spectrometer is given in the spectrometer manual, and should be consulted for further information about data acquisition and manipulation techniques.

Initialization of the disk file number that data collection will begin from is accomplished by entering the keystrokes:

TAPEFILE N TO TAPEFILE N

Where N is the number of the last occupied tapefile on the disk. This sets the counter in the spectrophotometer so that subsequent experimental data storage will not erase any previously collected data. The command keystroke sequence to begin data acquisition is as follows:

MEASURE TO TAPEFILE * ABSORBANCE TIME P1,P2, P3 TO P4

This command causes the spectrometer to measure a spectrum every P2 seconds, integrating over a P1 second interval (P2 must be greater than P1). The measured spectra are stored on disk in the next highest numbered file. The first spectrum is measured P3 seconds after the EXECUTE button is hit, and the last spectrum is measured at P4 seconds.

2.3.2.2 Actinometery and Spectral Convolutive Techniques

Incident photon flux (I_0) of the actinic beam is determined using Reinecke's salt actinometery[3] or by using a thermopile radient energy meter (Scientech model #224). Photon flux using these two methods are consistent with each other to within 10%. Typical photon flux using a 10 nm bandpass interference filter is $\approx 1 \times 10^{-8}$ einsteins/sec (1 einstein = 1 mole of photons).

2.3.2.2.1 Reinecke's salt actinometery

The technique of Wegner and Adamson for the purification and use of Reinecke's salt as an actinometer has been used.[5] Reinecke's salt ($K[Cr(NH_3)_2(NCS)_4]$) was recrystallized in the dark from the sodium salt. 3.0 ml samples of a filtered 0.02M (0.357 g/50 ml) reinecke's salt solution in 0.1N H_2SO_4 is irradiated with stirring in the specially designed cell holder described above. The concentration of reinecke's salt used depends on the irradiation wavelength, i.e., the solution should be high enough in concentration so that complete absorption of the actinic beam occurs. A blank solution is kept in the dark for the same period of time the sample solution is irradiated to correct for the thermal (dark) reaction of the reinecke's salt. After 1 minute irradiation intervals, 50 µL aliquots of the irradiated solution is added to 3 mL solutions of 0.1M

$Fe(NO_3)_3$ in 0.5N $HClO_4$, and the concentration of SCN^- released due to aquation of the reinecke's salt (in the $[Fe(H_2O)_5(SCN)]^{+2}$ form) is measured spectrophotometrically ($\epsilon_{450} = 4.3 \times 10^3\ M^{-1}\ cm^{-1}$). The $[SCN^-]$ yield of the blank solution is determined using the same procedure. Dilution(0.0125), dark reaction and quantum yield (0.300) factors are included in the following equation to determine the incident photon flux (I_0) in units of einsteins/second (1 einstein = 1 mole photons).

$$I_0 = \frac{[A_{450}(\text{sample}) - A_{450}(\text{blank})] \times 0.003L\ (\text{volume}) \times 80.0\ (\text{dilution})}{4.3 \times 10^3\ M^{-1}\ cm^{-1}(\epsilon_{450}) \times 0.300\ (\varphi_{SCN^-}) \times t,\text{sec}\ (\text{irradiation time})}$$

2.3.2.2.2 Thermopile Actinometery

Light exiting the fiber optics cable of the continuous photolysis apparatus is directed into a Scientech model *624 laser power energy meter. Power , reported in watts, is converted into einsteins/sec. by determining the joules/mole of photons incident on the thermopile and performing a unit conversion. The wavelength of maximum transmittance of the interference filter in the actinic beam determines the photon energy, which is calculated using the following equation:

2.3.1)

$$\frac{1}{\frac{1}{\text{wavelength (cm)}} \times \frac{11.963 \text{ J/mole}}{\text{cm}^{-1}}} = \frac{\text{moles of photons}}{\text{joule}} = N_\lambda$$

Incident power in watts is converted to photons/sec using the following equation:

2.3.2) $$\text{Watts (J/sec)} \times N_\lambda \text{ (moles of photon/J)} = I_0 \text{ (moles of photons /sec)}$$

2.3.2.2.3 Spectral Convolutive Techniques

Spectral convolutive techniques are used to determine the rate of photon absorption by a photosensitizer in solution. Rougee, et. al.,[6] have derived the following equation to calculate the fraction of the incident photons that are absorbed by the photosensitizer:

2.3.3)

$$F_{(p,x)} = \frac{\int_{\lambda_1}^{\lambda_2} \frac{dI_0}{d\lambda} \frac{A_\lambda(p)}{A_\lambda(p) + A_\lambda(x)} [1 - 10^{-(A_\lambda(p) + A_\lambda(x))}] \, d\lambda}{\int_{\lambda_1}^{\lambda_2} \frac{dI_0}{d\lambda} \, d\lambda}$$

λ_1 and λ_2 are determined by the transmittance range of the interference filter. $A_\lambda(p)$ corresponds to the absorbance of the photosensitizer, and $A_\lambda(x)$ correspond to the combined absorbance of all absorbing species in solution other than the photosensitizer. When the photosensitizer is the only absorbing species, this equation simplifies to:

$$2.2.4) \quad F_{(p)} = \frac{\int_{\lambda_1}^{\lambda_2} \frac{dI_0}{d\lambda} [1-10^{-(A_\lambda(p))}]\, d\lambda}{\int_{\lambda_1}^{\lambda_2} \frac{dI_0}{d\lambda}\, d\lambda}$$

$dI_0/d\lambda$,the intensity of the actinic beam, does not change significantly throughout the wavelength range of a narrow bandpass interference filter (≈10 nm fwhm).[4] The wavelength dependence of the intensity of the actinic beam once it has passed through the filter is therefore completely determined by the transmission characteristics of the filter. The absolute lamp intensity is not important in determining $F_{(p,x)}$ or $F_{(p)}$, as $dI_0/d\lambda$ appears in both the numerator and denominator of both expressions. Since the spectral intensity of the probe beam is directly proportional to the transmittance of the interference filter,the transmission spectrum of the filter can by used instead of the absolute lamp intensity in equation 2.2.3 and 2.3.4, thus simplifying the

determination of photon fluxes given below.

Equation 2.3.3 and 2.3.4 can be integrated convieniently using the data manipulating ability of the HP 8450A. It is first necessary to measure and store as standards the transmittance of the interference filter (STD 0), the absorbance of the photosensitizer (STD 1) and the irradiated solution (STD 2). STD 1 and STD 2 must contain equal concentrations of photosensitizer. If the only absorbing species in the irradiated solution is the photosensitizer, STD 1 is the absorbance spectrum of the solution before irradiation.

The integrated transmittance of the interference filter, $I_f = {}_{\lambda_1}\int^{\lambda_2} dI_0/d\lambda$, is calculated by first displaying the transmittance of the filter (STD 0) over the wavelength range λ_1 to λ_2. The keystroke sequence AVERAGE EXECUTE performs the integration and displays the averaged value.

$F_{(p,x)}$ can now be calculated by displaying STD 3 and entering the following sequence of commands:

(STD 0*STD 1/ABS)*(1-10**-ABS)/I_f EXECUTE

AVERAGE EXECUTE

To calculate $F_{(p)}$, STD 2 and the following commands are entered:

(STD 0 *(1-10**-ABS)/I_F EXECUTE

AVERAGE EXECUTE

The rate of photon absorption by the photosensitizer I_{abs} is given by:

2.3.5) $$I_{abs} = I_0 F_{(p,x)}$$

The integrated photon flux (total photons absorbed = $Q_{I,t}$) is given by:

2.3.6) $$Q_{I,t} = I_{abs}\, t$$

where t is the total irradiation time. If photoproducts are formed which absorb light in the same spectral region as the photosensitizer, then $F_{(p,x)}$ decreases with time. The following correction must be performed in order to account for the decrease in light intensity absorbed by the photosensitizer.

2.3.7) $$Q_{I,t+\Delta t} = Q_{I,t} + I_0 \Delta t[F_{(p,x)}(t) + F_{(p,x)}(t+\Delta t)]/2$$

2.4 References

1) Adler, A. D., Longo, F. R., Kampas, F., Kim, J. J. Inorg. Nucl. Chem. 32 2443 (1970)

2) Yang, J. M., Ph. D. Thesis, University of California, Berkeley CA (1981): LBL Report # LBL-13650

3) Birks, J. B., "Photophysics of Aromatic Molecules" Wiley-Interscience, London (1970) pp. 496-502

4) Seidell, A., Linke, W. F., "Solubilities of Inorganic and Metal Organic Compounds" Vol. 2, American Chemical Society, Washington, D.C. (1965), pg 1228

5) Wegner, E. E., Adamson, A. W., J. Am. Chem. Soc. 88, 394 (1968)

6) Rougee, M., Ebbeson, T., Ghetti, F., Bensasson, R. V., J. Phys. Chem. 86, 4404 (1982)

Chapter 3: Effect of Polyelectrolytes on Photoinduced Electron Transfer Reactions

3.1 Introduction

As discussed in chapter 1, the overall goal of the research outlined in this thesis is to find chemical systems capable of efficiently utilizing solar photons to drive the production of stable, high energy species via photoinduced electron transfer reactions. The prevention of the back-reaction between initial photoproducts is necessary to obtain high overall quantum efficiencies. Macromolecular systems capable of selectively altering intermolecular reaction rates between charged species have been investigated by researchers in the Calvin group and other research groups[1,2]. These charged interfacial systems have been used to increase quantum yields in photoinduced electron transfer reaction schemes such as the one shown below.

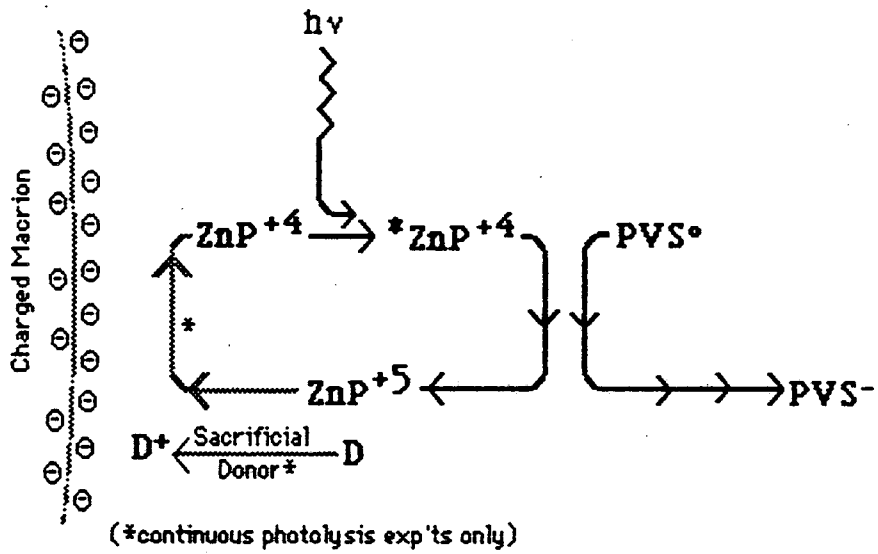

The individual reactions involved in this scheme are:

	Reaction	Rate Constant	Units
3.1.1)	$ZnP^{+4} + h\nu \longrightarrow {}^{1*}ZnP^{+4}$	I_0	einsteins $M^{-1}s^{-1}$
3.1.2)	${}^{1*}ZnP^{+4} \longrightarrow {}^{3*}ZnP^{+4}$	k_{isc}	s^{-1}
3.1.3)	${}^{3*}ZnP^{+4} \longrightarrow ZnP^{+4} + \text{heat}$	k_{uni}	s^{-1}
3.1.4)	${}^{3*}ZnP^{+4} + Q \longrightarrow ZnP^{+4} + Q^*$	k_q	$M^{-1}s^{-1}$
3.1.5)	${}^{3*}ZnP^{+4} + PVS^\circ \longrightarrow ZnP^{+5\cdot} + PVS^{-\cdot}$	k_f	$M^{-1}s^{-1}$
3.1.6)	$ZnP^{+5\cdot} + PVS^{-\cdot} \longrightarrow ZnP^{+4} + PVS^\circ$	k_b	$M^{-1}s^{-1}$
3.1.7)	$ZnP^{+5\cdot} + \text{Donor} \longrightarrow ZnP^{+4} + \text{products}$	k_d	$M^{-1}s^{-1}$

ZnP^{+4} is excited to the first excited singlet state upon visible photon absorption. Rapid, quantitative intersystem crossing to the lowest excited singlet state occurs. $^{3*}ZnP^{+4}$ undergoes unimolecular decay or the excited state is quenched through collisional quenching with PVS , residual O_2 or other impurity quenchers. These energy wasting quenching reactions compete with the forward reaction, which is the electron transfer quenching of $^{3*}ZnP^{+4}$ by PVS°. Forward reaction results in the formation of the initial photoproducts, $ZnP^{+5\cdot}$ + $PVS^{-\cdot}$. Back-reaction of the initial photoproducts competes with the sacrificial donor reaction. The donor reaction regenerates ZnP^{+4} and allows for the buildup of $PVS^{-\cdot}$.

back-reaction leads to no net $PVS^{-\cdot}$ production. A decrease in k_b leads to an increase in the quantum yield of $PVS^{-\cdot}$ formation (moles of $PVS^{-\cdot}$ formed per moles of photons absorbed by ZnP^{+4}). Note that the only reaction that occurs between <u>oppositely</u> charged species is the back-reaction between $ZnP^{+5\cdot}$ + $PVS^{-\cdot}$

Polyelectrolytes have been shown to decrease the rate of reaction between oppositely charged species in solution.[3] Reaction between similarly charged species is accelerated by the addition of polyelectroltyes. Interionic reactions are more strongly influenced by polyelectrolytes than by corresponding low molecular weight electrolytes. These features make polyelectrolytes potential candidates for use in selectively decreasing back-reaction rates in artificial photosynthetic systems.

In the reaction scheme shown above, the back-reaction is the only

reaction between oppositely charged species, therefore it should be possible to use the rate-retarding influence of polyelectrolytes to selectively decrease the back-reaction rate without changing other reaction rates in solution.

The influence of polyelectrolytes on reaction rates and the selectivity of polyelectrolyte effects is analogous to the influence of enzymes in biological systems. Since enzymes are essentially complex biological polyelectrolytes, this analogy is not unreasonable. Although the effects of polyelectrolytes are not nearly as dramatic as those of enzymes, polyelectrolytes can be used in artificial photosynthetic systems in much the same way as enzymes and other complex biological molecules are used in natural photosynthesis.

The mechanism of polyelectrolyte effects on interionic reactions is discussed in section 3.2. The electrostatic and hydrophobic interactions of polyelectrolytes with ionic and nonionic reactive species and the influence of these interactions on reaction rates are outlined.

Previous reports in the literature concerning the use of polyelectrolytes to control back-reaction rates in photoinduced electron transfer reaction systems are reviewed in section 3.3.

3.2 Macroion Effects on Interionic Reactions

It has been well established that interionic reaction rates can be strongly accelerated or decelerated by the addition of polyelectrolytes. Reactions between similarly charged ionic species can be accelerated by

addition of oppositely charged macroions. For example, the two reactions depicted in equations 1 and 2 are both accelerated by the addition of poly(ethylene imine), poly(styrene sulfonate) or poly(ethylene sulfonate).[4]

3.2.1) $CH_2BrCOO^- + S_2O_3^{-2} \rightarrow CH_2(S_2O_3)COO^{-2} + Br^-$

3.2.2) $2[Co(NH_3)_5Br]^{+2} + Hg^{+2} + 2H_2O \rightarrow 2[Co(NH_2)_5H_2O^{+3} + HgBr_2$

Reactions between oppositely charged species can be decelerated by the addition of either cationic or anionic macroionic species. Equation 3 depicts Wöhler's synthesis of urea, which is retarded by the addition of poly (acrylic acid).[5]

3.2.3) $NH_4^+ + OCN^- \rightleftarrows (NH_2)_2CO$

Macromolecular species have a much larger effect on interionic reaction rates than corresponding low molecular weight species. Both electrostatic and hydrophobic interactions between the polyelectrolyte and reactants are important considerations in determining how polyelectrolytes influence reaction kinetics. The observed changes in reaction rates can be accounted for in terms of the Brønsted equation for reactions that occur via an activated complex intermediate.[6] Primary and secondary salt effects are principally responsible for the observed influence of polyelectrolytes (and simple electrolytes) on interionic reactions. Salt effects of simple electrolyte solutions are discussed in sections 3.2.1.1 and 3.2.1.2. Deviations of polyelectrolyte solutions from

ideal solution behavior are responsible for the enhanced salt effects observed in polyion-containing solutions. These deviations are discussed in section 3.2.2.

It is noted here that the mechanism of the influence of polyelectrolytes discussed in this chapter is completely applicable to the discussion of the effect of charged colloidal particles, which are discussed in chapter 5. The major difference in theoretical models is that polyelectrolytes are considered to be "lines" of charge, whereas charged colloids are considered to be spheres with surface charges. The basic effects described in the following sections, however, apply to both polyelectrolytes and charged particles.

3.2.1 Salt Effects of Simple Electrolytes and Polyelectrolytes

3.2.1.1 Primary Salt Effects of Simple Electrolytes

For simple electrolytes, the change in interionic reaction rates due to electrostatic interactions has been described by Brønsted using Debye-Hückel theory and an activated complex theory[6,7]. For a reaction between two ions, $A+B \rightleftarrows X \rightarrow$ products, where X is the activated complex, the bimolecular rate constant is

$$3.2.3) \quad k_2 = \frac{kT}{h} K \frac{f_a f_b}{f_X} = \frac{kT}{h} \frac{f_a f_b}{f_X} e^{\Delta S^{\ddagger}/R} e^{-\Delta H^{\ddagger}/RT},$$

where K is the equilibrium constant for $A + B \rightleftarrows X$, $\int$ the activity coefficient of the species indicated by the subscript, $\Delta S^{\ddagger}$ and $\Delta H^{\ddagger}$ are the entropy and enthalpy of activation, h is the Planck constant, k the Boltzmann constant and T the temperature in degrees kelvin.

The Debye-Hückel theory of dilute electrolyte solutions[7] can be applied to determine the changes in $\int_a$, $\int_b$ and $\int_X$. For dilute aqueous solutions at 25 C, The Debye-Hückel limiting law for water is

3.2.4) $$\log \int_i = -.509\, z_i^2\, I^{1/2}$$

where $\int_i$ is the mean activity coefficient of ionic species, I is the the ionic strength, and z_i is the charge of the reactive species. Substituting the result of equation 3.2.4 into equation 3.2.3 gives

3.2.5) $$\log k_2 = \log[(kT/h)K] + 1.018\, z_a z_b\, [I]^{1/2}.$$

For reactions between similarly charged species, a rate enhancement is observed when ionic strength is increased. Reactions between oppositely charged species, however, are decelerated by the addition of electrolyte. For simple electrolytes in moderately dilute solutions ($I < 10^{-3}$ M) there is excellent agreement between this theory and experimental observations. This effect is commonly referred to as the

primary salt effect or the kinetic salt effect.

3.2.1.2 Secondary Salt Effects of Simple Electrolytes

Primary salt effect induced changes in reaction rates result from changes in the activity coefficients of the reactants and/or the critical complex. Interations of reactants and/or intermediates with ionic species in solution may cause a solvation-induced change in the free energy of reactive species. If solvation changes the relative free energies of the reactants and intermediate, the equilibrium constant for the reaction A + B$\rightleftarrows$ X will vary with ionic strength changes.

The reaction rate X$\longrightarrow$products is proportional to the concentration of the intermediate X. Since the difference in free energy between reactants and intermediate determines the concentration of the X, reaction rates can be influenced by a change in the equilibrium constant. The solvation-induced change in equilibrium constant (and reaction rate) is known as the secondary salt effect.

Solvation of ionic species generally increases in increasing ionic strength media through increased interactions with the ionic atmosphere. The stabilizing energy of solvation is proportional to the charge of the ionic species. For interionic reactions, the net charge of the intermediate is always different than the net charge of the reactants.

For reactions between oppositely charged species, the intermediate is less charged than the reactants, therefore solvation interactions of the

reactants are greater than that of the intermediate. The solvation-induced free energy change in the reactants is decreased relative to the intermediate, causing a shift in the equilibrium between reactants and intermediate and a corresponding decrease in reaction rate. For reactions between similarly charged species, the converse is true, i.e., solvation effects shift the equilibrium in favor of the highly charged intermediate. This leads to an increase in the observed reaction rate.

For ion-molecule reactions, the charge of the intermediate is the same as that of the charged reactant. Solvation effects are expected to stabilize reactants and intermediate equally. This should not result in a change in the relative free energy between reactants and intermediates, therefore no shift in equilibrium or change in reaction rate is expected to occur.

Secondary salt effects are observed only when solvation significantly changes the activation energy of intermediate formation. For reactions with large positive or negative activation energy barriers , solvation-induced changes in equilibrium constanst are neglible, so secondary salt effects are not observed.

3.2.2 Salt Effects of Polyelectroytes

Salt effects of simple ionic species cannot account for the dramatic effect that polyelectrolytes have on interionic reactions. An example of the large influence of polyelectrolytes is found in the reaction

between the anionic species $Fe-(CN)_6^{4-}$ and $S_2O_8^{2-}$, which is accelerated by a factor of 10^5 in the presence of the cationic polyelectrolyte polybrene (poly[(dimethylimino)-1,3-propanediyl(dimethyl--imino)-1,6-hexanediyl dibromide]).[8] This dramatic polyelectrolyte-induced acceleration cannot be accounted for in terms of simple primary salt effects alone. The deviations from ideality that occur in macroionic solutions that lead to the enhanced salt effects of polyions are discussed below.

3.2.2.1 Deviation of Macromolecular Solutions from Ideality

Brønsted and Debye-Hückel theories are successfully used to predict the influence of simple electrolytes on the equilibrium and kinetic properties of aqueous solutions. These theories fail to predict the effect of macromolecular species on interionic reactions. The failure of these theories to predict polyelectrolytes behavior lies in the fact that the assumptions implicit in the derivation of the equations shown above are not true for polyelectrolyte solutions. These assumptions are outlined in the following section.

3.2.2.2 Assumptions of Brønsted Theory

According to the Brønsted theory, the local concentration of

reactants throughout the solution is assumed to be uniform throughout the solution, i.e., no ion-pairing of reactants with any other soluton species occurs. In the model used to derive Debye-Hückel theory, the electric field surrounding charged species in solution induces a local enhancement in the concentration of oppositely charged counterions around ions in solution. The Brønsted treatment does not account for the nonuniform distribution of counterions since local ionic concentration fluctuations are insignificant compared to the primary salt effect-induced changes in activities of reactant species. As long as the net charge of ionic species in solution is low, these local fluctuations can be ignored. The Brønsted theory can then be successfully used to predict changes in equilibrium and kinetics.

The assumption that there is a uniform distribution of reactive ionic species throughout solution is incorrect in macrion-containing solutions owing to the high charge density of macroionic species. Counterion condensation of oppositely charged reactants by the highly charged macroion occurs. This "concentrates" reactant species on the surface of the macroion. The concentration effect of charged macromolecules creates a nonhomogeneous distribution of charged reactant species in solution. The local concentration of oppositely charged species is consequently increased in the vicinity of the macroion and decreased in the bulk solution.

Reactions between similarly charged species are increased in the presence of an oppositely charged macroion because both reactive species

are concentrated by the macroion. Oppositely charged species react more slowly with each other in the presence of macroions since the concentration of one of the reactants by the macroion decreases the concentration of that reactant in the bulk solution.

These concentration effects alone cannot account for the great influence that polyelectrolytes have on interionic reaction rates. Molecules and ions occupy a definite excluded volume, therefore the concentration of a reactant can only be increased to a certain limiting value.[9] Calculations of Koshland predict that intramolecular reaction rates are only 4.6 times faster than intermolecular reaction rates in water when reactants have the same excluded volume as water and the coordination number of the solvation structure is 12.[10] This factor of 4.6 is clearly insufficient to account for changes in rate constants in polyelectrolyte solutions of $\approx 10^5$. Additional electrostaic and hydrophobic aspects of polyelectrolyte solutions that contribute to the large influence of polyelectrolytes are discussed below.

3.2.2.3 Assumptions of Debye-Hückel Theory

A basic assumption implicit in the derivation of Debye-Hückel theory is that the term for the coulombic potential surrounding an ion, $\exp[-e\Psi/kT]$ (Ψ=electrostatic potential, q=electric charge), can be approximated by a truncated series expansion ($\exp[-q\Psi/kT] \approx (1-q\Psi/kT-...)$).[11] This linear approximation is crucial to the derivation of

a simple expression for the relationship between ionic strength and ion activity. In dilute solutions of simple ions the approximation that $q\Psi/kT<<1$ is valid.

In contrast to the case of simple ionic species, the local charge density of polyions is higher than that of simple ions. Electrostatic repulsion of like charges prevents the aggregation of similarly charged ions in simple ionic solutions. The charges on the polyion are covalently bound to a polymer backbone, therefore electrostatic repulsion forces cannot inhibit the aggregation of similar charges on a polyion. Highly charged macroionic species have correspondingly high values of Ψ. The linear approximation, $q\Psi/kT<<1$, is invalid for macroions and charged polymers with high surface charge densities. Debye-Hückel theory is not applicable in these cases. The use of the linear approximation gives too small a value for Ψ and consequently predicts too small an effect of macroions on activity coefficients and reaction rates.

A limiting law for determining mean activity coefficients in polyelectrolyte solutions has been developed by Manning.[12] The model used in Manning's theory is an infinite linear charge, rather than a point charge as is used in Debye-Hückel theory. This is a more physically realistic approximation of the ionic atmosphere around a charged polyion. Calculations of polyelectrolyte effects using Manning's theory and Brønsted's activated complex theory agree quite well with experimental data for a number of polyelectrolyte-influenced reactions.[13] This demonstrates that in most cases, the influence of polyelectrolytes can be

accounted for in terms of macroion induced changes in ionic activities.

3.2.3 Hydrophobic Effects of Polyelectrolytes

In addition to electrostatic influences of macroionic species described above, non-electrostatic interactions of polyelectrolytes with reactive species may also induce changes in reactivity in solution. These "hydrophobic" solvation interactions are completely different than the salt effects described in section 3.2.1.2.

The importance of hydrophobic interactions depends on the nature of the reactants and macroion being studied. Hydrophobic polyelectrolytes have been found to exert prounounced and sometimes unexpected influence on reactions between hydrophobic reactants. Hydrophobic interactions between a polyion and reactants may, in fact, be so strong that reactions between oppositely charged species are accelerated by the addition of polyion. This effect is observed in the kinetics of the alkaline-induced fading of triphenylmethlyene dyes.[14] Cationic triphenylmethane dyes are hydrophobic molecules having three benzene rings and bulky alkyl groups, as shown below.

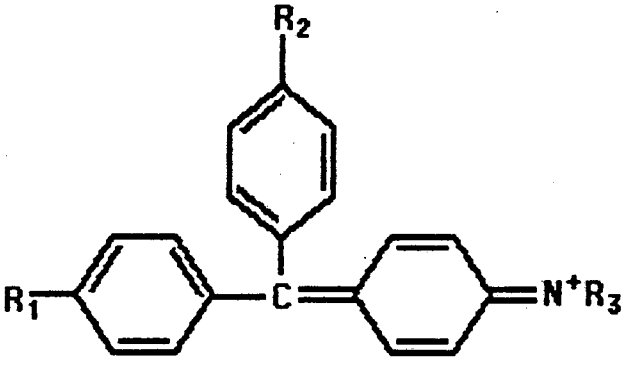

In the presence of a polyelectrolyte with hydrophobic aromatic moieties such as poly(styrene sulfonate), the reaction rate of triphenylmethane dyes with OH^- is increased relative to solutions containing no polyelectrolyte. This effect is opposite to the expected influence of polyelectrolytes on reactions between oppositely charged species. Obviously electrostatic interactions are not determining the effect of poly(styrene sulfonate) on this reaction rate. Non-hydrophobic cationic polyelectrolytes exhibit the expected polyelectrolyte effect on this reaction system, i.e., polyelectrolyte addition leads to a deceleration in reaction rate. This observation further demonstrates the importance of hydrophobic interactions in this reaction system.

As will be shown in section 3.5, it turns out that these hydrophobic interactions determine the effect of the anionic polyelectrolytes poly(styrene sulfonate) on the electron-transfer reaction between ZnP^{+4} and PVS°.

3.2.4 Pressure Influences on Solvation and Desolvation in Polyelectrolytes Systems

A study of the effect of pressure on the kinetics of interionic reactions demonstrates that the driving force responsible for the influence of polyions on reaction rates is sometimes involved with changes in hydration of the reactants and/or the activated complex upon association with the polyelectrolyte. According to transition-state theory, the pressure dependence of the rate constant is related to the volume of activation ($\Delta V^{\ddagger}$) by

$$3.2.6)\left[\partial \ln (\text{rate constant})/\partial P\right] = \Delta V^{\ddagger}/RT.$$

The volume of activation is related to the change in volume and electrostrictional solvation (or hydration) of the reactants and activated complex. For interionic reactions, the change in volume of the reactive species involved is neglible compared to the changes in solvation that occur during reaction,[15] so $\Delta V^{\ddagger}$ is due exclusively to changes in hydration of reactive species.

The study of the pressure dependence of the Ag^{+} induced aquation of $Co(NH_3)_5Br^{+2}$ demonstrates the importance of hydration in determining polyelectrolyte effects on interionic reactions.[16] In homogeneous solution, the reaction rate increased with increasing pressure. This is indicative of a negative $\Delta V^{\ddagger}$ (-5.3±2 ml/mol). This is reasonable considering that the activated complex is triply charged $[Ag^{+}\cdots Co(NH_3)_5Br^{+2}]$ therefore its hydration should be stronger than that of the reactants. A negative $\Delta V^{\ddagger}$

leads to a corresponding negative $\Delta S^{\ddagger}$ for this reaction. Addition of $5x10^{-4}$ equiv L^{-1} of poly(styrene sulfonate) leads to an increase in reaction rate by a factor of 91 and a large increase in $\Delta V^{\ddagger}$ (+76 ml/mol).

The increase in $\Delta V^{\ddagger}$ (and $\Delta V^{\ddagger}$) upon polyelectrolyte addition indicates that that the activated complex is more extensively dehydrated by macroions than the reactants. This dehydration leads to an increase in entropy due to the increase in disorder caused by the release of water molecules by the activated complex. The increase in reaction rate upon PSS addition must therefore be attributed to entropic factors which influence $\Delta G^{\ddagger *}$, $\int_X$, and reaction rate.

3.2.4 Conclusions

Section 3.2 has described the electrostatic and hydrophobic interactions between charged macromolecules and ions responsible for the influence of polyelectrolytes on interionic reactions. Both electrostatic and hydrophobic effects can be described in terms of activated-complex theory.

Primary and secondary salt effects are responsible for the influence of a macroion's electric field on the activity coefficients and free energies of reactive species in solution. Macroion-induced changes in activity and free energy are reflected in an induced change in reaction rate.

Hydrophobic interactions of macromolecules that are responsible for

changes in reaction rate arise from changes in solvation of reactants and/or intermediate induced by interaction of these species with a hydrophobic polyion.

3.3 Polyelectrolyte Influences on Photoinduced Electron-Transfer Reactions: A Review

The dramatic influence that polyelectrolytes have on interionic reactions has been demonstrated in the previous section. It seemed reasonable that these effects could be utilized in artificial photosynthetic systems to decrease back-reaction rates and increase quantum efficiencies.

The use of polyelectrolytes to decrease back-reaction in photoinduced electron transfer reactions has been studied by Sasoon and Rabani[2 a-d]. When uncharged molecules such as iron (III) nitriloacetate or cobalt (III) acetylacetonate are used to quench the luminescence of the photosensitizer $Ru(bpy)_3^{2+}$ by electron transfer, the addition of poly(vinyl sulfate) causes a decrease in the geminate recombination rate of the positively charged oxidized $Ru(bpy)_3^{+3}$ and the negatively charged reduced acceptor.[2e] These results are explained by the in terms of the electric field of the polyelectrolytes "repelling" the reduced acceptor away from the photochemical cage, thus enhancing the charge separation yield. The polyelectrolyte field also acts to slow the back-reaction of the oppositely charged separated photoproducts. The observed decrease in back-reaction

rate is less than a factor of ten in all cases studied. The magnitude of the observed effect does not compare favorably to back-reaction deceleration factors of $\approx 10^3$ observed in other macroionic systems, e.g. silica sols and micelles.

In another experiment by Sassoon and Rabani, forward (quenching) and back-reaction rate constants have been determined for the reaction system consisting of $Ru(bpy)_3^{+3}$ photosensitizer and N,N'-bis (4-sulfanoatlyl)-4,4'- bipyridinium (BSV^0) electron acceptor both in homogeneous solution and in the presence of poly(vinyl sulfate).[3a,b] These experiments are particularly relevant to the work described in this thesis because of the similarity of the components of the reaction system to the system exclusively studied and discussed herein.

To show the correspondance between this reaction system and the reaction system studied in this thesis, note that both $Ru(bpy)_3^{+2}$ and $ZnTMPyP^{+4}$ are positively charged, visible-light photosensitizers of electron transfer reactions. Note the similarity of the electron acceptors, PVS^0 and BSV^0 in the structural drawings below.

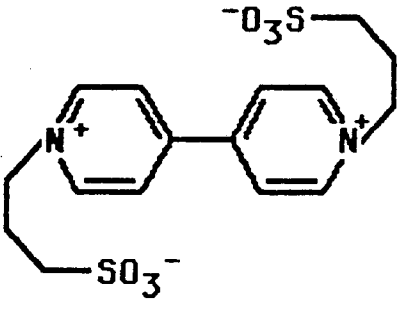

PVS^0
Propyl Viologen Sulfonate

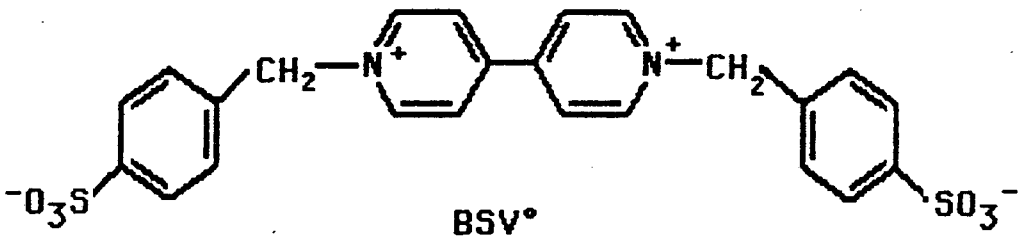

BSV°
N,N'-bis-(4-sulfonatolyl)-
4,4'-bipyridinium

PVS° and BSV° both contain the 4,4' bipyridinium structure. Both of these molecules are zwitterionic, neutral species with sulfonate groups acting as intramolecular counterions for the cationic pyridinium groups. The dipole moment of BSV° is probably slightly greater than that of PVS° owing to the greater separation of charges on BSV°. The less flexible sulfonatolyl group separating the charges in BSV° presumably do not allow as close an association of sulfonate and pyridinium charged groups as is possible in the PVS° molecule. The exact correspondence of the charges of the photosensitizers and electron acceptors between these two systems indicates that the polyelectrolyte effects observed for the two systems should be similar.

Fluoresence quenching experiments determined that the rate of quenching of $^*Ru(bpy)_3^{+2}$ by BSV° increases upon addition of 3×10^{-4} M poly(vinyl sulfate) from $1.4\pm0.3\times10^{9}$ $M^{-1}s^{-1}$ to $\approx6\times10^{10}$ $M^{-1}s^{-1}$ ($[Ru(bpy)_3^{+2}]= 4\times10^{-5}$ M). The back-reaction rate between $Ru(bpy)_3^{+3}$ and

$BSV^{-\cdot}$ decreased from $2.1\pm0.3\times10^{10}\ M^{-1}s^{-1}$ to $3.2\pm0.3\times10^{9}\ M^{-1}s^{-1}$ in 4×10^{-3} M poly(vinyl sulfonate). The increase in forward reaction is attributed to ion-dipole attraction of BSV° by the electric field surrounding the polyelectrolyte. This leads to an increase in the frequency of collision between BSV° and polyelectrolyte-bound $^{*}Ru(bpy)_3^{+2}$. The observed decrease in back-reaction rate is attributed to electrostatic repulsion of $BSV^{-\cdot}$ away from the negatively charged polyion. This results in a decreased collisional encounter frequency between the back reacting species, $Ru(bpy)_3^{+3}$ and $BSV^{-\cdot}$.

Our studies of polyelectrolytes originally resulted from the need to find a charged interfacial system with a more acidic charge functionality than the weakly acidic silanol group on colliodal silica (see chapter 4). The use of a charged polymer with a highly acidic sulfonic acid group such as poly(styrene sulfonate) was investigated, as this polymer was available commercially in highly purified form. The encouraging results of Sassoon and Rabani using poly(vinyl sulfate) further suggested that polyelectrolyte effects might act to decrease the rate of the back-reaction between $ZnP^{+5\cdot}$ and $PVS^{-\cdot}$ in the photochemical reaction scheme outlined in section 3.1, equations 1-7. The effect of the polyelectrolytes poly(styrene sulfonate) and poly(N-N-dimethyl-3,5- dimethylene piperidinium chloride) on the kinetics of forward and back-reaction electron transfer between ZnP^{+4} and PVS° are reported in the next chapter.

3.4 References

1) (a) Willner, I., Yang, J. M., Laane, C., Otvos, J. W., Calvin, M., J. Phys. Chem., 85, 3277 (1981) (b) Willner, I., Otvos, J. W., Calvin, M., J. Am. Chem. Soc., 103, 2507-2513 (1981)

2) (a) Sassoon, R. E., Aizenshtat, Z., Rabani, J., J. Phys. Chem., 89(7), 1182-1190 (1985); (b) Sassoon, R. E., Rabani, J., Isr. J. Chem., 22(2), 138-141 (1982); (c)Myerstein, D., Rabani, J., Matheson, M. S., Meisel, D., J. Phys. Chem., 82, 1879-1885 (1978); (d) Meisel, D., Matheson, M., Rabaini, J., J. Am. Chem. Soc., 100, 117 (1978)

3) a) Ise, N., Okubo, T., Kunugi, S., Acc. Chem. Res., 15, 171 (1982); b) Ise, N., Okubo, T., Macromolecules, 11, 439 (1978); c) Ise, N., J. Poly. Sci. Polym. Symp., 62,205 (1978); d) Ise, N. in "Polyelectrolytes and their Applications", Rembaum, A., Selegny, Eds., Reidel, Dordrecht, Holland (1975) p.71

4) Ise, N., Matsui, F., J. Am. Chem. Soc., 90, 4242 (1868)

5) Okubo, T., Ise, N., Proc. R. Soc. London, Ser. A, 327, 413 (1972)

6) Brønsted, J. N., Z. Phys. Chem. 102, 169 (1922); 115, 337 (1925)

7) Debye, P. J., Hückel, E., Physik. Z., 24, 185 (1923)

8) Enokida, A., Okubo, T., Ise, N., Macromolecules, 13, 49 (1980)

9) Morawetz, H., Gordimer, G., J. Am. Chem. Soc., 92,7532 (1970)

10) Koshland, D. E., J. Theoret. Biol. 2,75 (1962)

11) For a discussion of Debye-Hückel theory, see Atkins, P. W. "Physical Chemistry, W. H. Freeman, San Francisco (1978) pp 314-326.

12) (a)Manning, G. S. in "Polyelectroltyes", E. Selegny, Ed., Reidel

Publishing Co., Dordrecht, Holland (1974); (b) Manning, G. S., Zimm, B. H., J. Chem. Phys. 43, 4250 (1965); (c) Manning, G. S., J. Chem. Phys. 43, 4260 (1965); (d) Manning, G. S. J Chem. Phys. 51, 924 (1969)

13) Ise N., Okubo, T, Macromolecules 11(3), 439-447 (1978)

14) (a) Okubo, T., Ise, N. J. Am. Chem. Soc. 95, 2293 (1973); (b) Maruno, T., Okubo, T., Ise, N., Ber. Bunsenges. Phys. Chem. 85, 667 (1981)

15) Weale, K. B. "Chemical Reactions at High Pressures", E. And F. N. Spon Ltd., London (1967) chapters 5 and 6.

16) Ise, N., Maruno, T., Okubo, T., Proc. R. Soc. London, Ser. A, 370,485 (1980)

Chapter 4: Polyelectrolyte Effects on the Photoinduced Electron Transfer Reaction Between ZnP^{+4} and PVS°.

4.1 Introduction

The previous chapter discussed the mechanism of the influence of polyelectrolytes and other macroionic species in decreasing back-reaction rates between oppositely charged photoproducts in photoinduced electron transfer reactions. The encouraging results of other investigators in using polyionic systems led us to the study of the effect of the polyelectrolyte poly(styrene sulfonate) (PSS) on the reaction between ZnP^{+4} and PVS°.

Kinetic salt effect considerations lead to the prediction that the rate of back-reaction between the oppositely charged initial photoproducts $ZnP^{+5\cdot}$ and $PVS^{-\cdot}$ would be decreased upon addition of polyelectrolyte to the reaction system. These considerations also predict that the forward reaction between the cationic photosensitizer ZnP^{+4} and the neutral, zwitterionic electron acceptor PVS° would be unaffected (or slightly accelerated) by the addition of polyelectrolyte. The predicted decrease in back-reaction rate should lead to an increase in overall quantum yield of $PVS^{-\cdot}$ formation. An increase in the quantum yield of $PVS^{-\cdot}$ is desirable, as $PVS^{-\cdot}$ is capable of reducing H^+ to H_2 (g) in neutral or acidic solution ($E°_{PVS/PVS^-}$ = -0.41V vs. NHE) in the presence of a suitable redox catalyst. An increase in $PVS^{-\cdot}$ yield would lead to an increase in the theoretical efficiency of solar energy storage reactions utilizing artificial

photosynthetic systems of this kind.

This chapter describes experiments designed to probe the influence of the polyelectrolytes poly(styrene sulfonate) (PSS) and poly(N-N-dimethyl-3,5- dimethylene piperidinium chloride) (PolyP) on forward and back-reaction rates in photoinduced electron transfer reactions.

4.2 Experimental Section

4.2.1 Materials

Unless otherwixe noted, chemicals were obtained from commercial suppliers and were used without further purification. The synthesis and purification of ZnP^{+4} and PVS° are described in chapter 2.

High purity, molecular weight standard grade poly(styrene sulfonate, sodium salt) (PSS) was purchased from Polysciences, Inc. This high purity grade is specially purified and fractionated by the manufacturer for use as secondary molecular weight standards in electrophoresis experiments. The criteria used to determine the suitability of these PSS samples in photolysis experiments was to determine the effect of PSS on the lifetime of the excited triplet state of ZnP^{+4} in water. Samples that did not significantly decrease the lifetime of $^{3*}ZnP^{+4}$ were judged to be sufficiently pure. If significant amounts of impurity quenching was induced upon addition of a polyelectrolyte, that polyelectrolyte sample

was not used. Samples of molecular weight 2000 and/or 35000 were used in all experiments. The initial pH of all freshly prepared PSS solutions was consistently ≈2.5. NaOH was added to these solutions to neutralize this residual acidity. The high acidity is most likely due to incomplete neutralization of sulfonic acid groups on the polyion during manufacture.

PolyP(poly(N-N-dimethyl-3,5- dimethylene piperidinium chloride)) was obtained from Scientific Polymer Products, Inc., and was used without further purification. $^{3*}ZnP^{+4}$ lifetime measurements in polyP solutions indicated that there was no significant concentration of excited state quenchers in the polyP samples used. The approximate molecular weight of PolyP as supplied is $\approx 1 \times 10^6$. The structures of PSS and PolyP are shown below.

Polyelectrolyte Structures

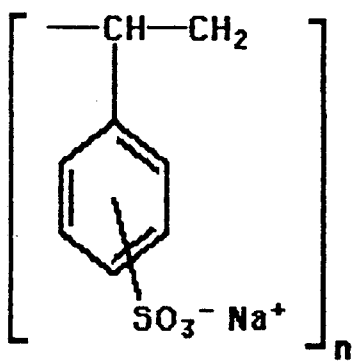

PSS
Poly(styrene sulfonate)

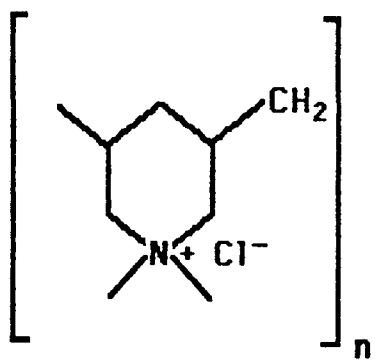

PolyP
Poly(N,N-dimethyl-3,5-dimethylene piperidine chloride

Polyelectrolyte concentrations are expressed in terms of

equivalents of monomer units/liter.

4.2.2 Measurements

Experimental procedures of flash photolysis and continuous photolysis experiments are discussed in chapter 2.

Visible spectra were recorded on a Hewlett-Packard HP-8450A UV/visible diode array spectrophotometer. Typical porphyrin concentration was 1×10^{-5} M. The extinction coefficient of ZnP^{+4} at 434 nm was determined to be 2.05×10^{5} $M^{-1}cm^{-1}$ by measuring the absorbance of a 1×10^{-5} M stock solution of ZnP^{+4}.

4.2.3 Methods

4.2.3.1 Spectrophotometric Titration of ZnP^{+4} by PSS and Poly(vinyl sulfate)

3 ml of a 1×10^{-5} M ZnP^{+4} was prepared by dilution of a 1×10^{-4} M ZnP^{+4} stock solution, and was placed in 1×1 cm silica cuvette. The cuvette was equipped with a spectral cell stirring bar and placed in the specially designed thermostatted cell holder described in chapter 2. The sample cell and holder were placed in the analytical beam path of the HP-8450A spectrophotometer, the sample was stirred and temperature equilibrated to 25 C. 10-100 µL aliquots of a 2.75×10^{-3} eq/L solution of

PSS or 4.25×10^{-3} eq/L of poly(vinyl sulfate) were added to the ZnP^{+4} solution and spectra were measured. The effect of polyelectrolyte addition on the extinction coefficient of ZnP^{+4} was determined by correcting for dilution by polyelectrolyte solution addition and converting to extinction using Beer's law ($A = \epsilon lC$, ϵ= extinction coefficient, l = cell path length, C= concentration of absorbing species).

4.2.3.2 Sample Preparation for Flash Photolysis Experiments

1×10^{-4} M ZnP^{+4}, 1×10^{-2} M PVS°, and 1.25×10^{-2} eq/L PSS and PolyP stock solutions were prepared within 24 hr of flash photolysis experiments. The pH of each stock solution was adjusted to ≈7 before use. 10 ml of sample solutions were prepared by combining 1 ml each of the polyelectrolyte, PVS°, and ZnP^{+4} stock solutions into a 10 ml volumetric flask and diluting to a final volume of 10 ml. Polyelectrolyte stock solution was added to the flask before the ZnP^{+4} stock solution to prevent precipitation of PSS by ZnP^{+4}, which occurs when $[ZnP^{+4}]>>[PSS]$. Homogeneous solutions containing no polyelectrolyte were prepared in a similar manner but without the addition of the polyelectrolyte stock solution to the final dilution. PVS° concentration was varied between $0.25-1.0\times10^{-3}$ M by adding differing amounts of PVS° stock solution to the final dilution. The pH of these final dilutions was adjusted to 7.0 prior to degassing. 3 ml aliquots of the final dilutions were measured into

specially designed airtight flash photolysis cells (see chapter 2) using a disposable 5 ml plastic syringe. Samples were deoxygenated by flushing the cell contents with purified argon gas for 30 min (Ar flow rate ≈ 100ml/min). Argon gas scrubbing methods are described in chapter 2. The residual O_2 concentration is estimated to be $\approx 2\times10^{-7}$ M.

4.2.3.3 Sample Preparation for Continuous Photolysis Experiments

1×10^{-4} M ZnP^{+4}, 2×10^{-2} M PVS°, 3.0×10^{-3} eq/L PSS, 1.0×10^{-2} M triethanolamine (TEOA) and 2.0 weight percent colloidal silica (Nalco chemical company #1115, 40Å diameter) stock solutions were prepared freshly prepared within 24 hr of experiments. Photolysis samples were prepared and degassed as described in the previous section. Final concentrations were as follows: [ZnP^{+4}] = 1×10^{-5} M, [PVS°]=2×10^{-3} M, [TEOA] = 1.0×10^{-3} M, [PSS]=3.0×10^{-4} M, silica (expressed as equivalents of surface SiO^-/L)=9.76×10^{-3} eq/L.

4.2.3.4 Determination of the Viscosity of PSS-Containing Aqueous Solutions

Viscosity measurements of polyelectrolyte solutions were performed by measuring the rate of gravity-induced flow of standard and polyelectrolyte solutions through a capillary. According to Poiseuelle's

Formula for the flow of fluid through a tube of radius R,

$$dV/dt = (p_1^2 - p_2^2)\pi R^4/16 l\eta p_0,$$

where V is the volume flowing, p_1 and p_2 are the pressures at each end of the tube of length l, and p_0 is the pressure at which the volume is measured.[1] By comparing the flow rates of different viscosity solvents, the relationship between flow rate and viscosity can be determined. The flow rates of water, methanol, acetonitrile and a 2×10^{-3} eq/l solution of PSS, MW=4000, were measured. These results are reported below:

Table 4.3.1
Effect of Solvent Viscosity on Capillary Flow Rate

Solvent	Flow Rate (ml/min)	Viscosity (millipoise)
Acetonitrile	9.37	3.45
Methanol	6.38	5.45
Water	4.76	8.90
1×10^{-3} eq/L PSS	4.91	

The negligible difference between the flow rates of water and PSS solution indicates that there is no signifiant increase in the bulk solution

viscosity of water upon the addition of up to 3×10^{-3} eq/L PSS.

4.2.3.5 Electrochemical Methods

Cyclic voltammetry experments were performed on an IBM Instruments Inc. EC-224 potentionstat using a glassy carbon working electrode, a saturated calomel reference electrode and a platinum wire counter electrode. 0.1 M KCl (Aldrich, gold label 99.99% purity) was used as supporting electrolyte in all experiments.

4.3 Experimental Results

4.3.1 Spectral Change of ZnP^{+4} in PSS Solutions

3 ml of a 1×10^{-5} M solution of ZnP^{+4} was titrated with 10-50 µL aliquots of a 2.75×10^{-3} eq/L solution of PSS. Visible spectra were recorded after each PSS addition by an HP 8450A UV/Vis spectrophotometer. Figure 4.3.1 shows the spectral titration data for the Soret band of ZnP^{+4} caused by addition pf 4K MW PSS. The spectra shown have been corrected for the dilution effect caused by PSS addition and are reported in units of extinction rather than absorbance.

Changes in the spectrum of ZnP^{+4} occur upon the addition of PSS. Extinction coefficient (ϵ) and wavelength maxima (λ_{max}) are shifted by addition of PSS. These spectral changes indicate that there is significant

Figure 4.3.1

Spectral Titration of ZnP^{+4} with PSS

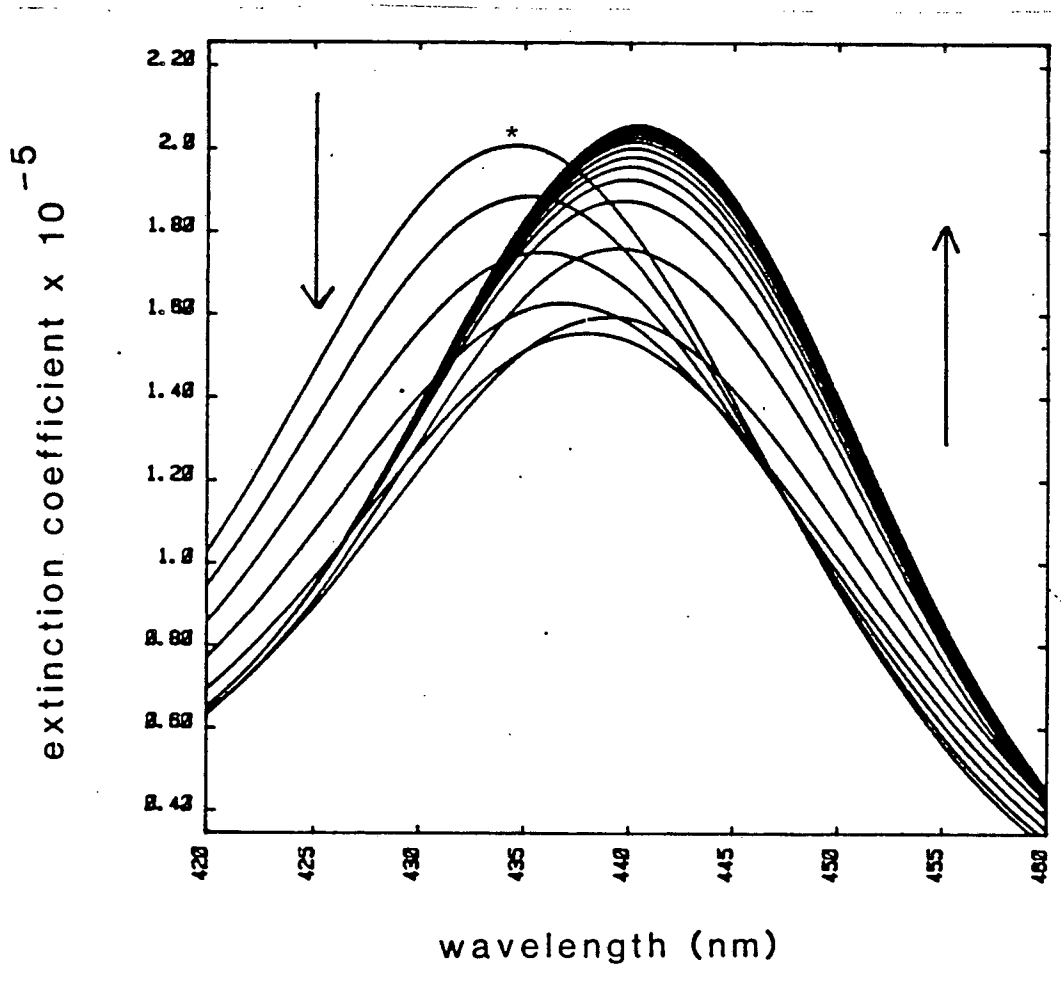

Spectral changes in the Soret band of ZnP^{+4} occuring during titration of 3.0 mL of a 1×10^{-5} M solution of in 0.09 M acetate buffer, pH 5.0, with 10µL aliquots of 3.6×10^{-3} eq/L PSS, MW = 4000. Spectra have been corrected for dilution. Arrows indicate the direction of titration. The first spectra (no PSS added) is denoted with an asterick.

ZnP^{+4} – PSS interaction. Although the change in ϵ and λ_{max} are both caused by additon of polyelectrolyte to aqueous solutions of ZnP^{+4}, the mechanism of these two effects is different in both cases. These mechanisms are discussed seperately in the following sections

4.3.1.1 Spectral "Flattening of ZnP^{+4} Induced by Aggregation of ZnP^{+4} onto PSS

The change in molar extinction of the soret band maxima (434-440 nm) which occurs upon addition of PSS is shown in figure 4.3.2.

The extinction coefficients of ZnP^{+4} initially decrease upon PSS addition, but as more PSS is titrated into solution, ϵ begins to increase. A minimum in ϵ_λ occurs when exactly 4 equivalents of polyelectrolyte per mole of ZnP^{+4} have been added. This point in the titration corresponds to exact charge neutralization of the 4 positive charges on ZnP^{+4} by the anionic sites of added PSS.

The observed decrease in ϵ_λ observed in PSS solution is ascribed to binding of the cationic ZnP^{+4} by the anionic polyelectrolyte PSS. The correspondance of charge between ZnP^{+4} and PSS at the observed minimum in ϵ_λ indicates that electrostatic interactions are important in this binding process. For both molecular weight PSS samples, addition of excess PSS causes the ϵ_λ to asymptotically approach a value somewhat

Figure 4.3.2

Effect of PSS Addition on Extinction Coefficient of ZnP^{+4}

Soret Band ϵ_λ

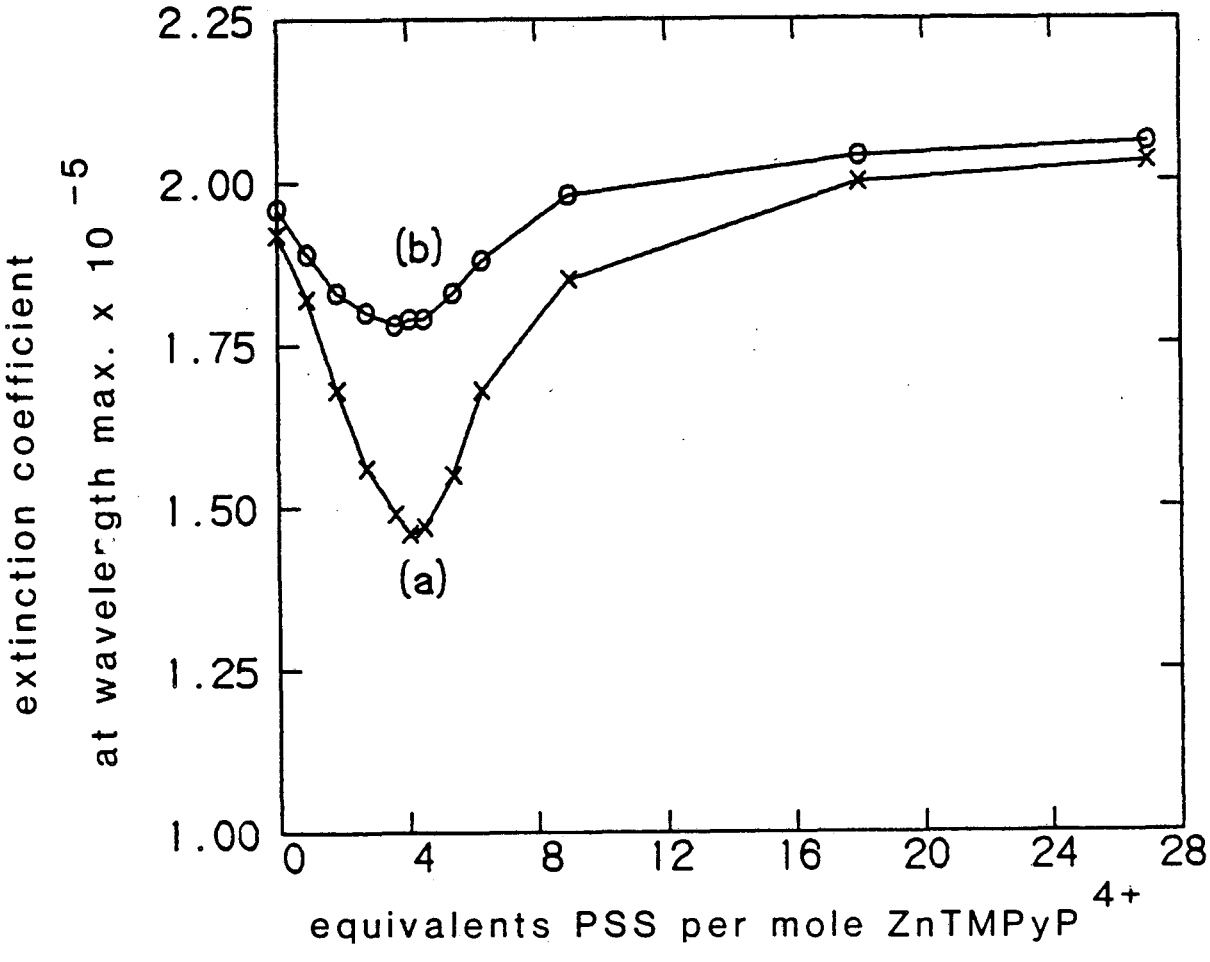

XBL 839-11395

Spectral data used to generate plot b derived from data shown in figures 4.3.1 a) PSS MW = 34,500. b) MW = 4000. ϵ_λ measured at Soret band absorption maximum.

higher than the ϵ_λ in solutions containing no PSS. The spectral change accompanying addition of PSS to ZnP^{+4} solutions is consistent with

higher than the ϵ_λ in solutions containing no PSS. The spectral change accompanying addition of PSS to ZnP^{+4} solutions is consistent with

polyion-binding. Reverse titrations performed by titrating aliquots of ZnP^{+4} into PSS solutions exhibit exactly the same spectral change as forward titrations, indicating that the association phenomenon is reversible.

The change in ϵ accompaning binding of ZnP^{+4} to PSS is believed to be due to "flattening" of the spectrum of ZnP^{+4}. Association of ZnP^{+4} by PSS results in a non-homogeneous distrubution of ZnP^{+4} in solution. ZnP^{+4} is concentrated in the vicinity of PSS polyanions. Complete absorption of light by PSS-bound ZnP^{+4} closest to the light source prevents the rest of the bound ZnP^{+4} molecules bound to the polyion from contributing to the total absorbance of ZnP^{+4}. This leads to a decrease in the absorbance compared to a solution in which the absorbing species are evenly distributed in solution. The masking effect is greatest in the spectral regions where extinction coefficients are large, so spectral features are "flattened" as a result.[2]

It is easy to envision the limiting case of flattening, i.e., the aggregation of all absorbing species in solution into a single crystal sitting on the bottom of the spectrophotometer cell. In this limiting case the absorbance of the solution would be zero. This is, of course, an

extreme case of spectral flattening. The relationships between aggregate size and the magnitude of the "flattening effect" have been derived by Duysens[3] and by Otvos, Stone and Harp.[4]

Note in figure 4.3.2 that the flattening effect of PSS on the absorbance of ZnP^{+4} is greatest when exactly 4 equivalents of PSS have been added. This indicates that at this point in the titration,the concentration of binding sites for ZnP^{+4} on PSS equals the concentration of ZnP^{+4}. Upon addition of more than 4 equivalents of PSS, redistribution of ZnP^{+4} on the increasing number of PSS molecules dilutes the observed flattening effect by decreasing the relative number of ZnP^{+4} molecules associated per PSS molecule. When [PSS]>>[ZnP^{+4}], no flattening is observed since aggregation of more than one or two ZnP^{+4} molecule on a single PSS molecule is extremely unlikely.

The flattening effect of the 35K PSS sample is greater than that observed for the 4K molecular weight sample. This is consistent with the spectral flattening mechanism. While the two molecular weight samples are equal w.r.t. charge equivalents/L, the concentration of polyion species is less for the higher molecular weight sample. The greater aggregation that occurs with the higher molecular weight species causes a correspondingly higher flattening effect.

The relationship between the flattening effect and aggregation size is derived below for a model system consisting of homogeneously distributed cubical, absorbing particles. The result of this calculation can be used to determine the effective particle size of the absorbing particles

once the flattening effect is determined.

For completely dispersed absorbing species, Beer's law can be applied to obtain

$$4.3.1) \qquad A=\epsilon l C$$

where A is the absorbance of the solution, l corresponds to the path length of the optical cell in cm, and C the concentration of absorbing species in molecules /cm^3 . ϵ is the optical cross section of the absorbing species expressed in units of cm^2/molecule.

For a suspension of absorbing cubical particles, Beer's law gives

$$4.3.2) \qquad A' = \epsilon' \, l \, C'$$

where A',ϵ' and C' correspond to the absorbance, cross-section and concentration of absorbing particles, respectively. For absorbing species bound to a particle, C' can be expressed in terms of the concentration of absorbing species if the number of absorbing molecules/particle (n) is known. The relationship between C and C' is simply

$$4.3.3) \qquad C' = C/n.$$

Equation 2 can now be expressed in terms of C.

4.3.4) $A' = \epsilon' \, l \, C/n$

The observed ϵ of the particulate system, ϵ_{app}, can be expressed in terms of the absorbing molecule concentration.

4.3.5) $\epsilon_{app} \equiv \epsilon'/n \equiv A'/Cl$

The ratio of the extinction coefficients of the homogenous and particulate systems is a measure of the flattening effect. This ratio, R, can be expressed as

4.3.6) $R \equiv \epsilon_{app}/\epsilon = \epsilon'/n\epsilon.$

R is an experimentally measurable quantity. ϵ' can be related to the dimensions of the absorbing cubical particle if the assumption is made that the orientation of the cubical particles is such that one of the faces of the cube lies perpendicular to the incoming light beam. In this case, ϵ', the cross section of absorbance of a particle is given by

4.3.7) $\epsilon' = a_p \, (1-\theta)$

where a_p is the area of one of the faces of the cubical particle, and θ is the fraction of light transmitted by the particle. $(1-\theta)$ corresponds

the the fraction of light absorbed by the particle. Application of Beer's law to a cube with dimensions d×d×d gives

$$4.3.8) \qquad \epsilon' = d^2 (1-e^{-\epsilon C_p d})$$

C_p corresponds to the concentration of absorbing species in the particle expresses as molecules/cm^3. $\epsilon C_p d$ corresponds to the absorbance of a particle, A_p. Equation 4.3.8 can be incorporated into equation 4.3.6, which gives

$$4.3.9) \qquad \epsilon_{app}/\epsilon = \epsilon'/n\epsilon = d^2/n\epsilon \ (1-e^{-A_p}).$$

This expression can be simplified by noting that n, the number of absorbing molecules/aggregate, can be expressed in terms of C_p and d.

$$4.3.10) \qquad n = C_p d^3$$

Substituting equation 10 into equation 9 gives

$$4.3.11) \qquad \epsilon_{app}/\epsilon = 1/C_p d\epsilon \ (1-e^{-A_p})$$

Since $C_p d\epsilon = A_p$, equation 4.3.11 can be expressed as

4.3.12) $$R \equiv \epsilon_{app}/\epsilon = (1-e^{-A_p})/A_p$$

A_p can now be determined using R. Since ϵ is known and C_p can be calculated if n is known, the determination of A_p allows the calculation of d, the effective dimension of the absorbing particle.

Assuming complete binding of ZnP^{+4}, the minimum in ϵ' which occurs during spectral titration of ZnP^{+4} by PSS corresponds to complete occupation of ZnP^{+4} binding sites on PSS. Calculations of the quantities derived in the treatment above have been performed based on the spectral titration data for 4K and 35K molecular weight PSS samples.

Table 4.3.2

Calculations of Molecular Aggregate Dimensions Based on Flattening Effects for 4K and 35K MW PSS Samples

Molecular Weight	4000	35,000
n	4.81	41.95
$R \equiv \epsilon_{app}/\epsilon$ *	.868	.709
A_p	.290	.733
ϵ' (cm^2/molecule)	2.96×10^{-16}	2.43×10^{-16}
d	75 nm	140 nm

* ϵ_{app} measured at 4 equivalent of PSS/mole of ZnP^{+4}.

The ratio of the calculated volumes of the 4K and 35K molecular weight samples should correspond to the ratio of the calculated molecular weights for polymer/ZnP^{+4}-complexes for these two molecular weight samples, since volume and mass are directly proportional. The experimentally determined ration of volumes, d^3_{4K}/d^3_{35K}, is 0.153. The calculated molecular weight ratio of 4K and 35K molecular weight PSS samples is $MW_{4K\ PSS}/MW_{35K\ PSS} = 0.114$. The calculated volume ratio based on spectral flattening data is therefore higher than expected based on the ratio of molecular weights.

The observed spectral behavior of ZnP^{+4} upon addition of PSS is, however, basically consistent with the proposed model of spectral "flattening". The observations of an increase in flattening effect with increased aggregate size and the maximum in flattening effect observed upon addition of exactly 4 equivalents of PSS charges/mole of ZnP^{+4} are both consistent with the flattening mechanism.

While the spectral flattening mechanism is consistent with the observed change in porphyrin extinction coeffiecients upon addition of PSS, this mechanism does not explain the observed red shifts in the spectrum of ZnP^{+4} in PSS solution. Interactions of ZnP^{+4} with the hydrophobic interior of PSS macroions are proposed to be responsible for the spectral shifts observed. Environmental influences on porphyrin spectra are discussed in the next section.

4.3.1.2 PSS-Induced shifts in λ_{max} of ZnP^{+4}

Electrostatic considerations are important in the binding of ZnP^{+4} by PSS, as evidenced by the correspondance of charge equivalents of ZnP^{+4} and PSS at the point of minimum ϵ_{λ}. The red shift in the absorption maxima of ZnP^{+4} upon PSS addition is evidence that electrostatic interactions are not the only factors which influence the spectrum of ZnP^{+4} in the presence of PSS.

Porphyrin spectra are sensitive to the environment in which the porphyrin is situated. The solvent environment influences metalloporphyrin spectra by ligation[5], complexation[6], and by inducing porphyrin self-aggregation.[7] A change in the solvent polarity can also bring about changes in porpyrin spectra.[8] These factors bring about a variety of spectral changes, e.g., red or blue shifts in λ_{max} or an increase or decrease in ϵ. These factors do not influence all porphyrin spectra in the same way, which makes it difficult to assign observed spectral changes to any one of these effects. Most of these factors can be ruled out as the cause of the spectral changes observed when PSS is added to ZnP^{+4}.

Association of ZnP^{+4} and PSS certainly occurs, as evidenced by the spectral flattening discussed in the previous section. This complexation alone is not sufficient to explain the spectral shifts observed in PSS solution, as the addition of an equivalent concentration (equivalents/L) of

a monomeric analog of PSS, sodium benzene sulfonate, does not result in any change in the spectrum of ZnP^{+4}. The shift in λ_{max} in PSS solutions must be due to additional interactions of ZnP^{+4} with the polyionic species.

If self-aggregation of ZnP^{+4}on the polyelectrolyte chain were responsible for the shift in the λ_{max} , then the addition of other anionic polyelectrolytes to ZnP^{+4} solutions would be expected to induce similar spectral shifts. A spectral titration of ZnP^{+4} by a solution of the anionic polyelectrolyte poly(vinyl sulfate) does not exhibit the polyelectrolyte-induced red shift in the soret band of ZnP^{+4}, even though poly(vinyl sulfate) is expected to form a complex with the cationic ZnP^{+4} through electrostatic interactions.

Addition of poly(vinyl sulfate) does induce a decrease in ϵ_λ in much the same way as PSS does, which indicates that association of ZnP^{+4} with poly(vinyl sulfate) occurs. As in PSS solutions, the minimum in ϵ_λ occurs when exactly 4 equivalents of poly(vinyl sulfate) per mole of ZnP^{+4} have been added, after which further addition of polyion gives rise to an increase in ϵ_λ. The spectral flattening phenomenon believed to be responsible for this behavior is discussed in section 4.3.1.1. No corresponding shift in the porphyrin λ_{max} is observed in poly(vinyl sulfate) solutions. If electrostatic binding of ZnP^{+4} by PSS induced porphyrin self aggregation, poly(vinyl sulfate) addition to ZnP^{+4} solutions would also be expected to induce aggregation behavior in a similar way.

The major difference between PSS and poly(vinyl sulfate) is the absence of a aromatic benzene moiety in poly(vinyl sulfate). This implies that the red shift in the λ_{max} of ZnP^{+4} in PSS solution is not caused by polyelectrolyte-induced self-aggregation, but is instead due to interactions between polyion-bound ZnP^{+4} and the aromatic, hydrophobic "interior" of PSS.

In the above argument,the PSS-induced red shift in the spectrum of ZnP^{+4} is ascribed to hydrophobic interaction between ZnP^{+4} and the aromatic moieties of PSS. The spectrum of ZnP^{+4} in a solution of a monomeric analog of PSS, sodium benzene sulfonate, does <u>not</u> exhibit the spectral change observed upon addition of an equivalent amount of PSS,which indicates that some kind of cooperative effect of the aromatic moieties of PSS is necessary to induce the observed change in the spectrum of ZnP^{+4} in PSS solutions.

The effect of different solvents on the spectrum of ZnP^{+4} was studied in order to better understand the role of envronment on spectral shifts. It is already well known that porphyrin spectra are influenced strongly by solent polarity. To investigate the spectral behavior of ZnP^{+4} as a function of solvent polarity, the spectrum of ZnP^{+4} was measured in a variety of solvents. The results of these measurements are shown in figure 4.3.3, which indicates that for all solvents tested, the soret band of ZnP^{+4} shifts to longer wavelengths in less polar solvents. The variation of λ_{max} in different solvents is indicative of the complexity of ZnP^{+4} interactions with solvent species. The large scatter in this plot is

due to the variety of interactions that are possible between ZnP^{+4} and solvent species.

The observation of a red shift in less polar solvents is consistent with the conclusion that hydrophobic interactions of ZnP^{+4} with the aromatic interior of PSS is responsible for the red shift of λ_{max} in PSS solution. The hydrophobic aromatic groups of PSS are certainly less polar than water.

Figure 4.3.3

Effect of Solvent Dielectric on ZnP^{+4} Soret Band λ_{max}

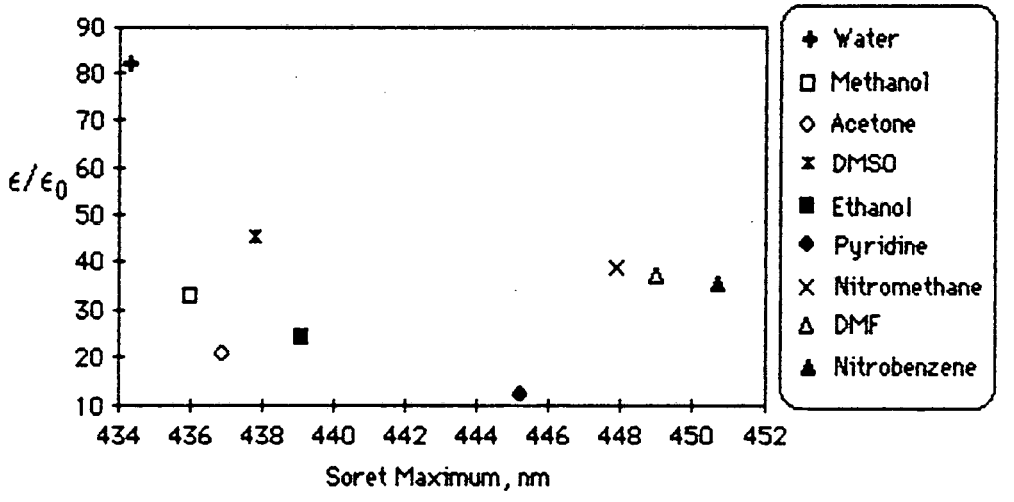

Variation of ZnP^{+4} Soret band maximum in a variety of solvents plotted as a function of solvent dielectric constant. Solutions were prepared by injection of 0.1 ml of a 1×10^{-4} M aqueous stock solution of ZnP^{+4} into 3.0 ml of solvent.

The energetic basis of these hydrophobic interactions is generally attributed to the tendency to preserve hydrogen bonding in the water structure in the vicinity of a hydrophobic portion of a solute in an aqueous solution.[9] In other words, the disruption of hydrogen bonding of water molecues with each other is lessened when two hydrophobic moieties are associated with each other. Considering the general insolubility of uncharged porphyrin species in water, this kind of association is not unreasonable.

4.3.1.3 Conclusions

Spectral changes that are observed upon addition of PSS to aqueous solutions of ZnP^{+4} indicate that strong binding of ZnP^{+4} onto PSS occurs. Both electrostatic and hydrophobic forces influence this binding phenomenon.

Interactions of ZnP^{+4} with the hydrophobic interior of PSS are responsible for the observed red shift in the porphyrin soret λ_{max}. The interactions are dependant of the presence of the hydrophobic benzene moieties of PSS and the geometric arrangement of the aromatic groups imposed by the polymer structure. Without both of these factors present, no red shift in the spectrum of ZnP^{+4} is observed.

"Flattening" of the spectrum of ZnP^{+4} is observed upon addition of PSS or other polyelectrolyte to ZnP^{+4} solutions. This flattening is a result of the nonhomogeneous distribution of ZnP^{+4} in solution which is induced

by binding of ZnP^{+4} to the polyelectrolyte via electrostatic and hydrophobic interactions.

The two effects of PSS on the spectrum of ZnP^{+4} described above indicate that strong ZnP^{+4}-PSS binding occurs in solution. This binding does influence the effect of PSS on photoinduced electron transfer reactions, as will be shown in the following sections.

4.3.2 Continuous Photolysis Experiments

4.3.2.1 Introduction

Section 4.3.1 described the change in the spectrum of ZnP^{+4} that occurs upon PSS addition. These changes indicate that ZnP^{+4} is tightly associated with PSS in solution. In order to probe the effect of PSS on the overall quantum efficiency of photoinduced electron transfer reactions between ZnP^{+4} and PVS°, continuous photolysis experiments were performed using ZnP^{+4} as photosensitizer, PVS° as reversible electron donor, and triethanolamine (TEA) as irreversible electron donor. The overall reaction scheme is described in detail in section 3.1.

4.3.2.2 Results of Continuous Photolysis Experiments

Figure 4.3.4 shows the yield of PVS^- as a function of the number of photons absorbed by the photosensitizer ZnP^{+4} for solutions containing no polylelectrolyte or macroions, 6.7×10^{-4} eq./L PSS, or 0.1% (2.5×10^{-3} equivalents SiO^-/L) colloidal silica sol. The concentration of ZnP^{+4} used, 3.5×10^{-6} M, is such that [PSS]>> [ZnP^{+4}]. In this case, porphyrin-porphyrin interactions and shadowing effects induced by condensation of the cationic porphyrin onto the anionic PSS macroions are not significant. TEOA (1×10^{-3} M) is used as the sacrificial electron donor. The PVS° concentration in all experiments is 2×10^{-3} M. All experiments were performed at pH 10.2.

To date, colloidal silica sols have been shown to be the most effective interfacial system for preventing back-reaction in photoinduced electron transfer reactions.[1] Control experiments using Nalco #1115, 40Å diameter silica particles have been included herein order to compare the effect of PSS to that of a charged macromolecular system which causes a significant <u>increase</u> in the quantum yield of this reaction system. The use of colloidal silica sols will be more fully discussed in chapter 4.

The results of these continuous photolysis experiments show that the overall quantum yield of $PVS^{-\cdot}$ ($\Psi_{PVS^-\cdot}$) is increased upon addition of PSS. This observed increase in $\Psi_{PVS^-\cdot}$ is, however, not nearly as significant as the increase in $\Psi_{PVS^-\cdot}$ that is observed upon addition of colloidal silica to solutions.

Figure 4.3.4

Effect of PSS and Colloidal Silica on The Quantum yield of PVS- Formation in Continuous Photolysis Experiments

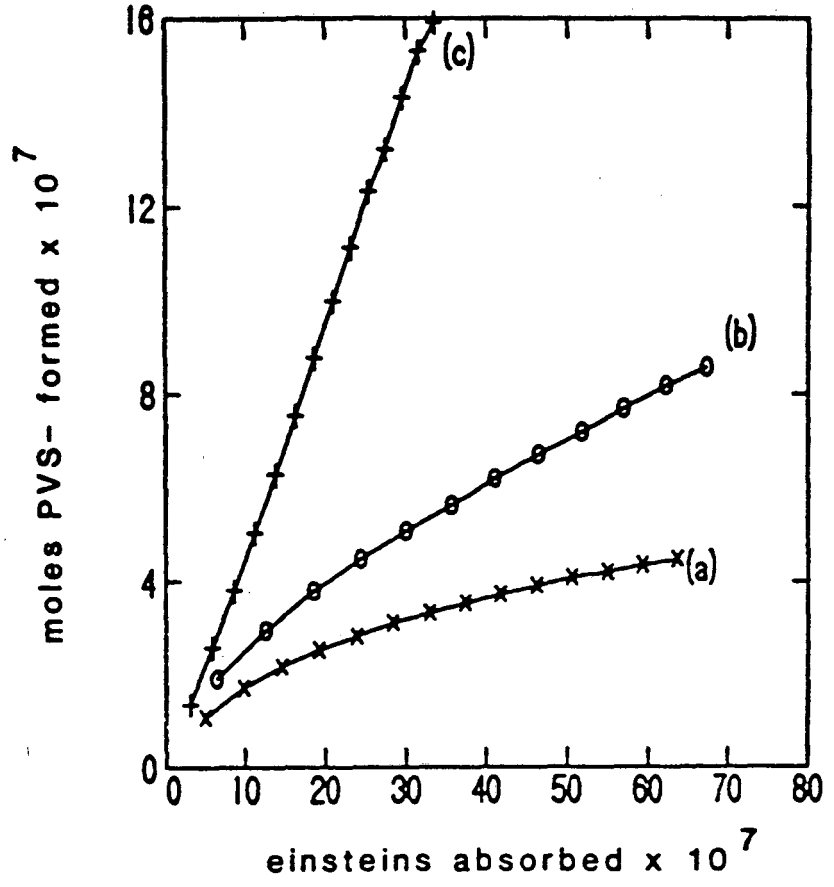

$PVS^{-\cdot}$ formation as a function of light quanta absorbed by ZnP^{+4} under continuous photolysis conditions described in section 2.3. Conditions: $I_0 = 7.8\times10^{-8}$ einsteins/sec; $[ZnP^{+4}] = 3.5\times10^{-6}$ M; $[PVS^{\circ}] = 2.0\times10^{-3}$ M; [TEOA] = 1.0×10^{-3} M. All experiments were performed at pH 10.2.

a) homogeneous, no macroions added

b) with 6.7×10^{-4} eq/L PSS, MW = 4000

c) with 0.1% w/v Nalco silica sol #1115 (2.5×10^{-3} eq. SiO^{-}/L)

Because of the complexity of the reaction system involved in continuous photolysis experiments, it is impossible to directly relate the results obtained from these experments in terms of individual forward and back-reaction rate constants. The observed reaction rate ($\partial[PVS^-]/\partial t$) is a result of the combination of all the individual reaction rates in solution. The complexities associated with sacrificial electron donor reactions are discussed in the following section.

4.3.2.3 Sacrificial Donor Reactions

In section 3.1, the reaction involving regeneraton of oxidized ZnP^{+5} via reaction with a sacrificial electron donor is represented by:

4.3.13) $ZnP^{+5\cdot} + \text{Donor} \longrightarrow ZnP^{+4} + \text{products}$

The decomposition reactions of most of the species used as sacrificial electron donors is not as simple as equation 4.3.13 depicts; the initial decomposition products of donor oxidation usually have reducing capability. The extra reducing equivalent that is available from donor oxidation results in a theoretical maximum overall quantum yield of 2 in photoreduction systems using sacrificial electron donors.

The existence of a second reduction step in donor reaction schemes has been assumed recently in studies of similar systems using the

sacrificial donors EDTA,[10] Triethanolamine,[11] triethylamine,[12] and cystine.[13] The overall reaction sequence proposed for the photoreduction of methyl viologen (MV^{+2}) by $Ru(bpy)_3^{+2}$ using triethanolamine as a sacrificial electron donor is shown below.

4.3.14) $$*Ru(bpy)_3^{+2} + MV^{+2} \longrightarrow Ru(bpy)_3^{+3} + MV^{+\cdot}$$

4.3.15) $$Ru(bpy)_3^{+3} + (C_2H_5OH)_3N: \longrightarrow Ru(bpy)_3^{+2} + (C_2H_5OH)_3N^{\cdot+}$$

4.3.16) $$(C_2H_5OH)_3N^{\cdot+} + MV^{+\cdot} \longrightarrow (C_2H_5OH)_3N: + MV^{+2}$$

4.3.17) $$(C_2H_5OH)_3N^{\cdot+} + (C_2H_5OH)_3N: \longrightarrow (C_2H_5OH)_3\ddot{N}{-}H^{+} + (C_2H_5OH)_2N{-}\dot{C}H{-}CH_2OH \text{ or } (C_2H_5OH)_2N{-}CH_2{-}\dot{C}HOH$$

4.3.18) $$(C_2H_5OH)_2N{-}\dot{C}H{-}CH_2OH \text{ or } (C_2H_5OH)_2N{-}CH_2{-}\dot{C}HOH + MV^{+2} \longrightarrow MV^{+\cdot} + (C_2H_5OH)_2NH + CH_3CHO$$

The TEOA reaction products of equation 4.3.18 have been determined by pulse radiolysis experiments.[14] The limiting quantum yield for photoreactions using sacrificial electron donors is <u>two</u>. The reaction products are diethanolamine and acetaldehyde. In all cases, two electron oxidation of the donor species occurs, resulting in a maximum production of two reduced species for each photon absorbed.

In addition to the extra reducing equivalent available from

sacrificial donors, additional reactions occur which further complicate the use of a simple kinetic model to determine reaction rate constants in continuous photolysis experiments. For example, in a study of the porphyrin-photosensitized reduction of methyl viologen, Rougee, et al. [13] determined that the following complex series of reactions of the sacrificial electron donor, cysteine, were responsible for the reported kinetics of reduced viologen photoproduction.

4.3.19) $P^{+}\cdot + CysSH \longrightarrow P + CysSH^{+}\cdot$

porphyrin regeneration

4.3.20) $CysSH^{+}\cdot + MV^{+}\cdot \longrightarrow CysSH + MV^{+2}$

reoxidation of MV^{+2}

4.3.21) $CysSH^{+}\cdot \longrightarrow CysSH\cdot + H^{+}$

deprotonation

4.3.22) $CysSH\cdot + MV^{+}\cdot \longrightarrow CysS^{-} + MV^{+2}$

reoxidation of MV^{+2}

4.3.23) $CysSH\cdot + CysS^{-} \rightleftarrows CysS\text{–}S\text{–}Cys^{-}\cdot$

dimer equilibrium

4.3.24) $CysS-S-Cys^{-\cdot} + MV^{+2} \longrightarrow CysS-S-Cys + MV^{+\cdot}$

second MV^{+2} reduction

The rate of reaction 4.3.24 has been measured by pulse radiolysis to be $k_6 = 8\times10^8\ M^{-1}\ s^{-1}$. [13]

The simplified reaction depicted in equation 1 cannot be used to describe the complex behavior of the sacrificial donor cysteine in this reaction scheme. When reactions 4.3.19-4.3.24 are incorporated into the reaction scheme proposed for this system, reaction rate parameters can be derived which agree well with experimental data.

The main point of this discussion is that reaction kinetics of continuous photolysis experiments using sacrificial donors are complicated by the reactions of donor species. Although these reactions can be accounted for in kinetic schemes, no simple relationship exists between the overall quantum yield of $PVS^{-\cdot}$ and back-reaction rate. In additon to the complications inherent in using sacrificial donors, the effect of charged interfaces and polyelectrolyte on the rates of these donor reactions is unknown. Certainly, any change in the rates of reactions 4.3.14 - 4.3.18 in the donor reaction scheme above would be reflected in a change in the observed quantum yield.

In order to probe the effects of PSS on the individual forward and back-reaction rate constants of the photoreduction of PVS° by $^{3*}ZnP^{+4}$, time-resolved laser flash photolysis experiments were performed. These experiments are described below.

4.3.3 Laser Flash Photolysis of the Photoinduced Forward and Back-electron Transfer Reaction Between ZnP^{+4} and PVS°

4.3.3.1 Introduction

The relative complexity of photoreaction systems containing sacrificial donors discussed in the previous section makes kinetic analysis of continuous photolysis experiments difficult. The experimentally determined rate constants depend on the rate constants of sacrificial donor reactions. The uncertainties associated with these donor reaction rate constants add to the uncertainty of the experimentally determined rate constants. Addition of polyelectrolytes or charged macroions is likely to alter the donor reaction rates as well as forward and/or back electron transfer reaction rates.

Continuous photolysis experiments are therefore not a good way to quantitate the effect of macroions on the individual forward and back-reaction rate constants in photoinduced electron transfer reactions. Simplification of the kinetic scheme allows the quantitative determination of these rate constants. The individual forward and back-electron transfer rates of the photoreaction between ZnP^{+4} and PVS° are such that time-resolved techniques are necessary to measure these

rates individually. Laser flash photolysis experiments are particularly suited to the measurement of these rates.

In flash photolysis experiments, no sacrificial electron donor is added. This simplifies the reaction scheme considerably. With no donor present, the only reaction of primary photoproducts is back-reaction with each other. The concentration of primary photoproducts, $PVS^{-\cdot}$ and $ZnP^{+5\cdot}$, are equal throughout the course of the reaction. This greatly facilitates kinetic analysis of transient data. Time-resolved techniques can monitor short-lived species at a varitety of wavelengths, allowing the simultaneous measurement of the temporal behavior of more than one reactive species in solution.

Flash photolysis experiments have been performed to determine the effect of PSS and PolyP on the forward and back electron transfer reaction between PVS° and ZnP^{+4}. Kinetic analysis of the flash data indicates that selective reduction of back-reaction rates is achieved upon addition of PolyP, a cationic polyelectrolyte. This result is consistent with the proposed mechanism of polyelectrolyte salt effects on interionic reactions discussed in chapter 3. The theory of primary salt effects in polyelectrolyte solutions predicts that the forward reaction (an ion-molecule reaction) should be unchanged upon the addition of the polyion, while back-reaction between oppositely charged photoproducts is expected to decrease in polyelectrolyte solution.

In PSS solution, however, flash photolysis results are inconsistent with the simple picture of electrostatic polyelectrolyte effects. Kinetic

analysis of the data indicates that both forward and back-reaction rates are decreased by the addition of PSS.

The decrease in both forward and back-reaction rate is attributed to hydrophobic "envelopment" of ZnP^{+4} by PSS, which decreases the rates of all bimolecular reactions involving ZnP^{+4}. This kind of envelopment effect has also been observed by Turro, et al., in PSS solutions containing cationic fluoresence probes.[15] Because forward reaction rates are decreased concurrently with back-reaction rates, the usefulness of PSS in increasing quantum yields in this photoreaction is not as great as expected.

4.3.3.2 Results

4.3.3.2.1 Fitting of Transient Data to Kinetic Model

The simplified reaction scheme used to model the kinetics of flash photolysis experiments is shown below.

Reaction Scheme for Flash Photolysis Experiments

	Reaction	rate constant	units
4.3.24)	$ZnP^{+4} + h\nu \longrightarrow {}^{1*}ZnP^{+4}$	I_0	einsteins·s^{-1}
	light absorption		
4.3.25)	${}^{1*}ZnP^{+4} \longrightarrow {}^{3*}ZnP^{+4}$	k_{isc}	s^{-1}
	singlet-triplet intersystem crossing		
4.3.26)	${}^{3*}ZnP^{+4} \longrightarrow ZnP^{+4}$	k_d	s^{-1}
	unimolecular triplet decay		
4.3.27)	${}^{3*}ZnP^{+4} + PVS^{\circ} \longrightarrow ZnP^{+4} + PVS^{\circ}$	k_q	$M^{-1}s^{-1}$
	collisional quenching of ${}^{3*}ZnP^{+4}$ by PVS°		
4.3.28)	${}^{3*}ZnP^{+4} + O_2 \longrightarrow ZnP^{+4} + O_2$	$k_{q'}$	$M^{-1}s^{-1}$
	collisional quenching of ${}^{3*}ZnP^{+4}$ by O_2		
4.3.29)	${}^{3*}ZnP^{+4} + PVS^{\circ} \longrightarrow ZnP^{+5\cdot} + PVS^{-\cdot}$	k_f	$M^{-1}s^{-1}$
	electron-transfer quenching of ${}^{3*}ZnP^{+4}$ (forward reaction)		
4.3.30)	$ZnP^{+5\cdot} + PVS^{-\cdot} \longrightarrow ZnP^{+4} + PVS^{\circ}$	k_b	$M^{-1}s^{-1}$
	back-reaction of initial photoproducts		

Light absorption and singlet-triplet intersystem crossing (4.3.24 and 4.3.25) are effectively instantaneous reactions compared to the time scale of transient measurements. This is demonstrated by the fact that the duration of the laser pulse is ≈150 ns, the fluoresence lifetime of $^{1*}ZnP^{+4}$ is 1.4 ns.[16] These times are compared to the minimum time resolution of the digital oscilloscope used to collect transient data, 50 ns per point.

The differential equation describing the evolution of $^{3*}ZnP^{+4}$ with time is

$$4.3.31) \quad -d[^{3*}ZnP^{+4}]/dt = (k_d + k_{q'}[O_2] + (k_f+k_q)[PVS^\circ])\,[^{3*}ZnP^{+4}]\,.$$

In all experiments performed, $[PVS^\circ] >>> [^{3*}ZnP^{+4}]$, i.e., ($[PVS^\circ] > 2.5\times10^{-4}$ M, $[^{3*}ZnP^{+4}] < 3.5\times10^{-6}$ M), so the reactions 4.3.27 and 4.3.29 are pseudo-first order in $[PVS^\circ]$. The assumption of pseudo-first order kinetics for oxygen quenching is also valid, as discussed in section 2.2.5.2. Triplet quenching experiments described in chapter 2 have been used to calculate $k_{q'}$ and $[O_2]$ in homogenous solution. The values determined for these two quantities are $k_{q'} = 1.3\times10^{9}\ M^{-1}s^{-1}$ and $[O_2] = 3.0\times10^{-7}$ M. k_d has been determined to be ≈ 350.[16]

Assuming pseudo-first order kinetics hold for $[PVS^\circ]$, and $[O_2]$, equation 4.3.31 can be integrated to give

4.3.32) $[^{3*}ZnP^{+4}]_{(t)} = [^{3*}ZnP^{+4}]_0 \exp-((k_d+k_q'[O_2]+ (k_q+k_f)[PVS^\circ])t,$

where $[^{3*}ZnP^{+4}]_0$ is the initial concentration of $^{3*}ZnP^{+4}$ immediately after the laser pulse , and t is the time after the laser pulse. By making the substitutions $k_d+k_q'[O_2] = k_1$ and $(k_q+k_f)= k_2$, equation 4.3.32 can be simply expressed as

4.3.33) $[^{3*}ZnP^{+4}]_{(t)} = [^{3*}ZnP^{+4}]_0 \exp-(k_1+ k_2[PVS^\circ])t.$

$[^{3*}ZnP^{+4}]_0$ is determined by monitoring the initial absorbance change at 480 nm, where $^{3*}ZnP^{+4}$ absorbs strongly.

Based on reactions 4.3.24 to 4.3.30, the time rate of change of $[PVS^-]$ can be expressed as

4.3.34) $d[PVS^-]/dt = k_f[PVS^\circ][^{3*}ZnP^{+4}] - k_b[PVS^{-\cdot}][ZnP^{+5\cdot}]$.

Reactions 4.3.29 and 4.3.30 are the only reactions leading to the buildup and decay of both $PVS^{-\cdot}$ and $ZnP^{+5\cdot}$, therefore $[PVS^{-\cdot}]=[ZnP^{+5\cdot}]$, and equation 4.3.34 can be expressed as

4.3.35) $d[PVS^-]/dt = k_f[PVS^\circ] [^{3*}ZnP^{+4}] - k_b[PVS^{-\cdot}]^2.$

Substituting the expression for $[^{3*}ZnP^{+4}]$ in equation 4.3.33 into

equation 4.3.35 gives

$$4.3.36) \quad d[PVS^{-}]/dt = k_f[PVS^{\circ}][^{3*}ZnP^{+4}]_0 \exp-(k_1 + k_2[PVS^{\circ}])t - k_b[PVS^{-\cdot}]^2.$$

This nonlinear differential equation does not have a simple analytical solution. Numerical techniques must be used to integrate this expression to obtain $[PVS^{-\cdot}]$ vs. time data. In addition to the contribtution of $PVS^{-\cdot}$, $^{3*}Zn^{+4}$ also contributes to the absorbance change at 600 nm. $[^{3*}ZnP^{+4}]$ can be calculated using equation 4.3.33, so the contribution of $^{3*}ZnP^{+4}$ absorbance can be added to the numerically integrated determination of $[PVS^{-\cdot}]$ to obtain the time dependant behavior of the total absorbance change at 600 nm. By comparing the experimentally observed data with data simulations, values of all the individual rate constants in the expression above can be varied in the numerical integration until there is good agreement between observed and simulated data.

Appendix 4.1 gives the listing of the FORTRAN program INT.FOR, which was used to perform the numerical integration of equation 4.3.36. This program uses Euler's method to perform the integration. The three variables used in INT.FOR, k_q'', k_q', and k_b correspond to $k_1/[PVS^{\circ}] + k_q$, k_f, and k_b, respectively, used in equations 3.33 and 3.36.

Table 4.3.2 lists the extinction coefficients used in the kinetic analysis of flash photolysis exerimental data. Excited-state extinction coefficients for $^{3*}ZnP^{+4}$ in homogeneous solution and in 1.0×10^{-3} eq/L

PSS solution were determined using excitation saturation techniques described in chapter 2.

Table 4.3.3

Extinction Coefficicents Used in Kinetic Analysis of Flash Photolysis Experimental Data

Species	ϵ_{480}	ϵ_{600}	notes
$^{3*}ZnP^{+4}$	32000	1300	*
$^{3*}ZnP^{+4}$ in PSS sol'n	26500	1000	*
$PVS^{-\cdot}$		12800	ref. 1a
$ZnP^{+5\cdot}$		5000	ref. 17

* note: Excited state species ϵ are reported as $\Delta\epsilon \equiv (\epsilon\ ^{3*}ZnP^{+4} - \epsilon\ ZnP^{+4})$

4.3.3.2.2 Results of Data Simulations of Transient Absorbance Data

Figure 4.3.5 shows the transient absorbance change in solutions containing 1×10^{-5} M ZnP^{+4} and 1.0×10^{-3} M PVS°. The change in absorbance at 600 nm follow a 300 ns duration, 590 nm laser pulse. The sample that

exibits the transient behavior labeled "with PSS, MW=4000" also contains 1.0×10^{-3} eq/L PSS (MW = 4000). Both solutions were adjusted to pH 7.0 before flashing.

The absorbance change at 600 nm is primarily due to buildup and decay of $PVS^{-\cdot}$. Figure 4.3.5 depicts the influence of PSS on both the buildup and decay of $PVS^{-\cdot}$, indicating that both forward and back-reaction rates are decreased upon addition of PSS. The influence of PSS and PolyP on individual forward and back-reaction rates was determined using data simulation and curve fitting techniques outlined in the next section.

Figures 4.3.6 and 4.3.7 again show the experimental transient data for solutions both with and without added PSS. The time scale of the homogeneous solution data has been expanded to show the time behavior of the signal in more detail. Note the similarities in the temporal behavior of the homogeneous and PSS containing samples. This indicates that both the buildup of $PVS^{-\cdot}$ (forward reaction) and its subsequent decay (back-reaction) are depressed by roughly the same amount in PSS solution.

Superimposed on the experimental data are data simulations which are derived from integration of equation 4.3.36. The fits shown in figures 4.3.6-4.3.8 are representative of the quality of fit of the kinetic model to the data. There are several distinct features of the data, i.e., the initial absorbance, the height of the maximum and the time after the

Figure 4.3.5

Effect of PSS on The Transient Absorbance Behavior of PVS^{-}.

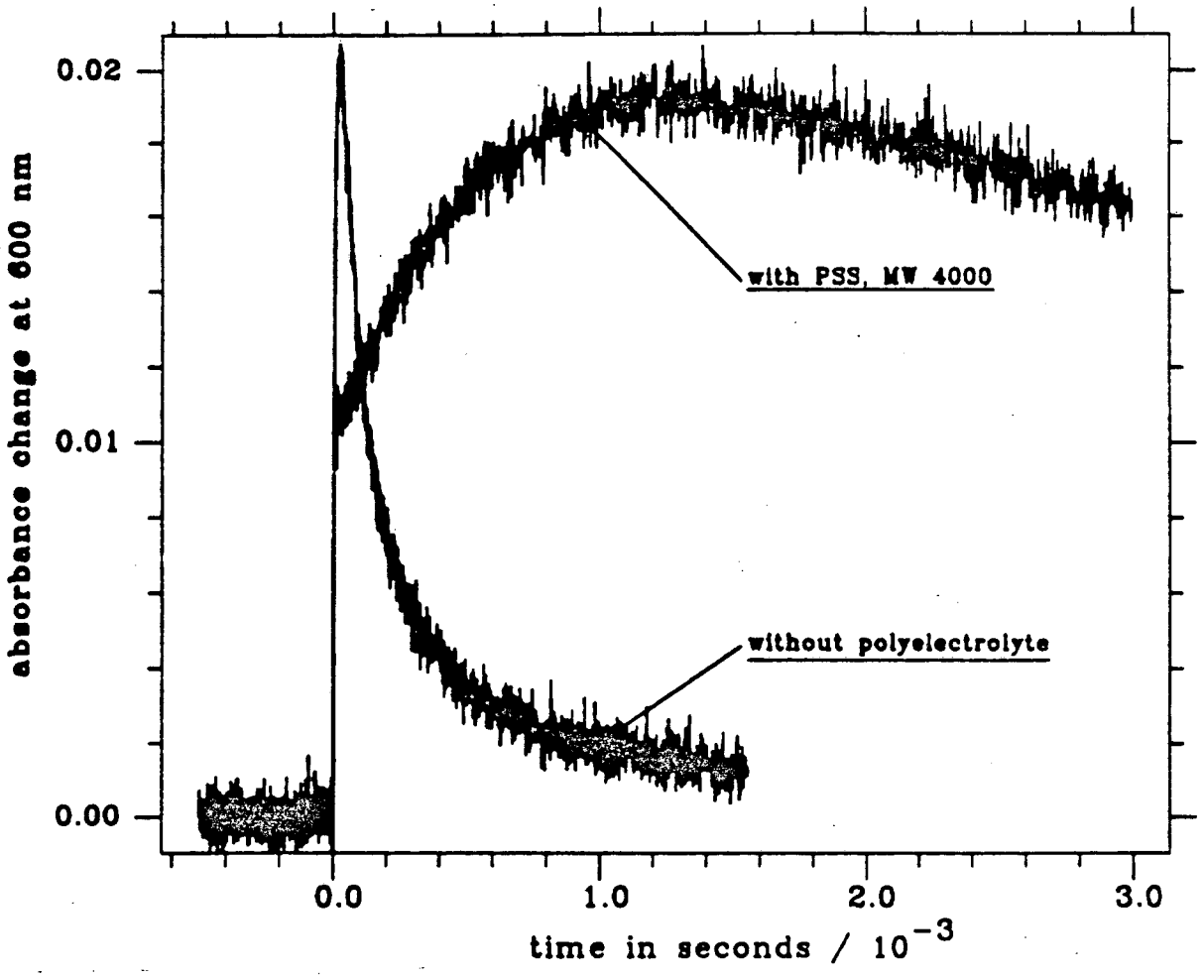

Transient absorbance change at 600 nm. $[ZnP^{+4}] = 1\times10^{-5}$ M, $[PVS^{\circ}] = 1.0\times10^{-3}$ M, ph 7.0. a) no polyelectrolyte; b) with 1×10^{-3} M PSS.

Figure 4.3.6

Calculated Vs. Experimental Transient Absorbance Change at 600 nm, Homogeneous Solution

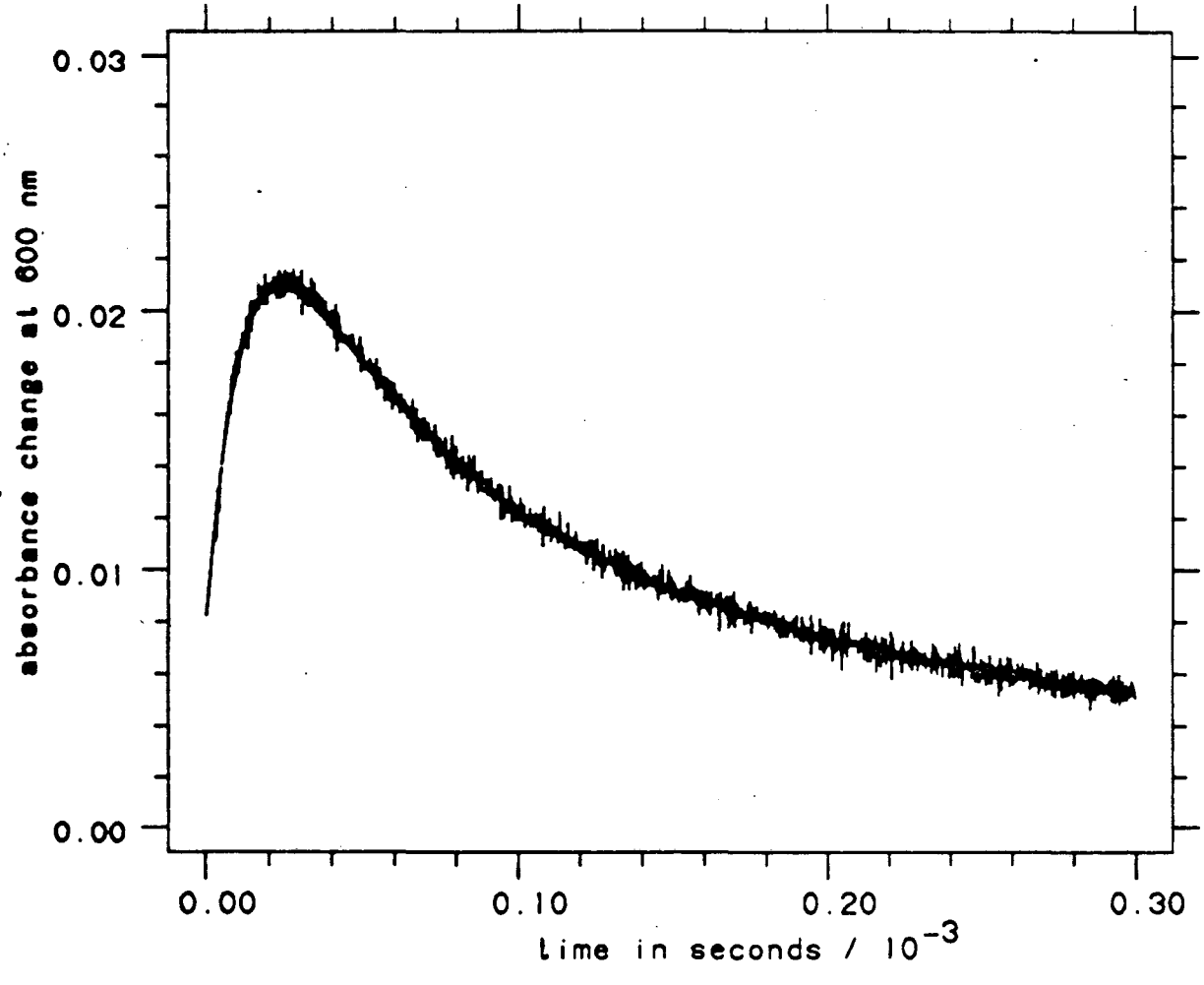

Calculated vs. expermental transient absorbance change at 600 nm. $[ZnP^{+4}] = 1\times10^{-5}$ M, $[PVS^{0}] = 1.0\times10^{-3}$ M, pH = 7.0.

Figure 4.3.7

Calculated Vs. Experimental Transient Absorbance Change at 600 nm. Poly(styrene sulfonate) solution

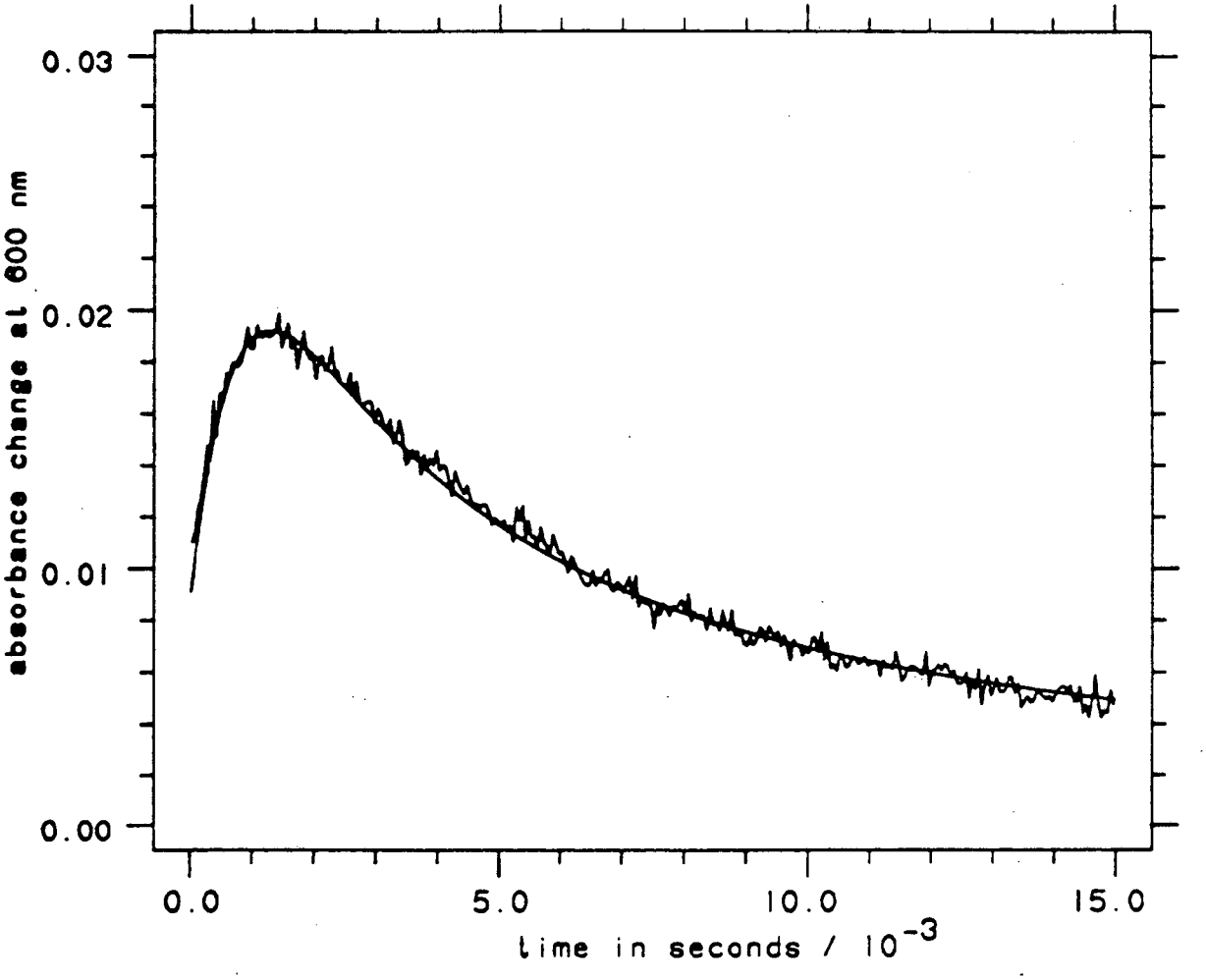

Calculated vs. experimental transient absorbance change at 600 nm.

$[ZnP^{+4}] = 1\times10^{-5}$ M, $[PVS^{\circ}] = 1.0\times10^{-3}$ M, $[PSS] = 1\times10^{-3}$ eq/L

Figure 4.3.8

Calculated Vs. Experimental Transient Absorbance Change at 600 nm, PolyP solution

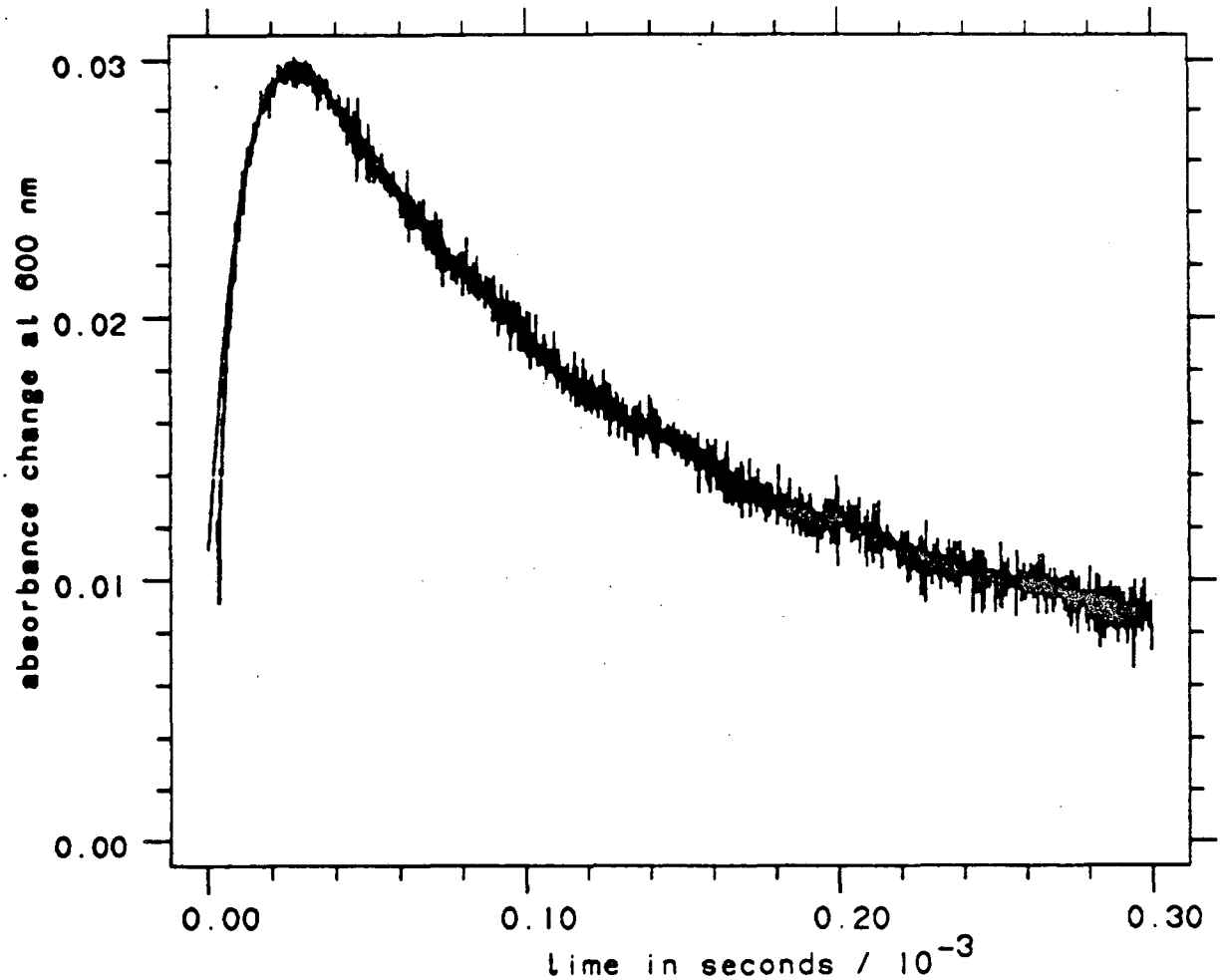

XBL 848-3451

Calculated vs. experimental transient absorbance change at 600 nm. $[ZnP^{+4}] = 1\times10^{-5}$ M, $[PVS^{0}] = 1.0\times10^{-3}$ M, [PolyP] = 1×10^{-3} eq/L, pH = 7.0.

flash at which it occurs, and the shape of the rise and decay of the transient. A good fit to the data lends creditibility to the kinetic model and the rate constants derived.Table 4.3.3 lists the values of kinetic parameters determined by the curve fitting methods described above for homogeneous and PSS containing solutions under a variety of experimental conditions.

Table 4.3.4

Calculated Rated Constants Determined By Curve Fitting of Transient Data to Proposed Kinetic Scheme

$[^3*ZnP^{+4}]_0$ M $\times10^6$	$[PVS^-]$ M $\times10^4$	$k_1/[PVS^-]+k_q$ $M^{-1}s^{-1}$ $\times10^{-7}$	k_f $M^{-1}s^{-1}$ $\times10^{-7}$	k_b $M^{-1}s^{-1}$ $\times10^{-7}$
a) with no polyelectrolyte				
2.14	2.5	6.0 (±0.2)	3.0(±0.1)	650 (±30)
2.38	2.5	5.7	3.0	660
3.45	2.5	5.8	3.0	670
3.70	2.5	5.8	3.0	670
3.78	2.5	5.8	3.0	670
2.06	5.0	4.0	3.0	690
3.78	5.0	4.0	3.0	710
2.55	10.0	1.5	3.0	700
b) With 4K MW PSS, 1.0×10^{-3} eq/L				
3.98	10.0	0.04 (±.002)	0.065 (±.002)	16 (±2)
c) With PolyP, 1.25×10^{-3} eq/L				
3.45	10.0	1.4(0.2)	3.0(0.2)	390(30)

The results of the kinetic analysis of flash photolysis data of solutions containing PolyP indicate that while PolyP addition has no effect on either quenching or forward reactions, the back-reaction is decreased by a factor of ≈2. These results are consistent with the electrostatic model of polyelectrolye effects discussed in chapter 3.

The most significant result of the PSS experiments is that both forward and back-reaction rate constants were decreased upon addition of PSS. In fact, all bimolecular reaction rate constants are decreased by a factor of ≈ 60 - 100. Since electron-transfer and collisional quenching reactions between $^{3*}ZnP^{+4}$ and PVS° are ion-molecule reactions, the electrostatic model of polyelectrolyte influence predicts that PSS will not change these reaction rates. The fact that these ion-molecule reaction rates are decreased along with the rate of the back-reaction between oppositely charged species indicates that electrostatic interactions between PSS and reactants are not responsible for the observed decrease in reaction rates in PSS solution.

The reasons behind the discrepancy between the predicted salt effects of polyelectrolytes and the observed decrease in bimolecular rate constants involving PSS-bound ZnP^{+4} are discussed in the next section.

4.3.4 Discussion

The decrease in all bimolecular reaction rates involving PSS-bound ZnP^{+4} is not consistent with the electrostatic picture of polyelectrolyte

effects discussed in chapter 3. Primary salt effects predict that both k_q and k_f will be unaffected by PSS addition. The experimental results reported here clearly do not correspond to this model of polyelectrolyte behavior. Hydrophobic polyelectrolyte influences can sometimes predominate over electrostatic effects, as demonstrated by the unexpected influence of polyelectrolytes on the alkaline fading reaction of triphenylmethane dyes described in section 3.2.3. The PSS-induced red shift in the spectrum of ZnP^{+4}, discussed in section 4.3.1, indicates that there are hydrophobic interactions between PSS and ZnP^{+4}. It is not unreasonable that hydrophobic forces should influence these reaction rates as well.

A recent study by Turro and Okubo demonstrated that the apparent microviscosity experienced by a cationic fluorescent probe bound to PSS is substantially higher that that of aqueous solution. The fluorescence maximum (λ_{max}) and lifetime (τ) of a positively charged indole derivative was found to be very sensitive to the environmental polarity, i.e., λ_{max} and τ are 374 nm and 16 ns , respectively, in pure water, but shift to 350 nm and 4-8 ns in detergent solutions.[15] When this probe was added to PSS solutions, it was found to associate strongly with the macroion in an environment with an approximate microviscosity of $\approx$150cP.[18] This evaluation of apparent microviscosity is based on measurements of the change in molecular anisotropy of the probe upon addition of PSS. The authors conclude that the hydrophobicity and

microviscosity experienced by the probe associated with PSS are extremeley high compared to those of the probe associated with micelles or in water alone.

The observed decrease in bimolecular reaction rates observed in PSS containing solutions is ascribed to a hydrophobic envelopment of the reactive ZnP^{+4} molecule by PSS. This envelopment sterically hinders the approach of all reactants, thereby decreasing all bimolecular reaction rates involving PSS-bound ZnP^{+4}. The proposed mechanism accounts for the fact that the effect of PSS does not seem to be related to the charge of the reactants.

Alternative possible explanations of the decrease in bimolecular reaction rates in PSS solutions were investigated and ruled out as possible causes of the observed decrease in reaction rates. Either an increase in the bulk viscosity of PSS-containing solutions or a decrease in the rate of PVS° diffusion would account for the observed decrease in bimolecular reaction rates. Both of these possibilities were tested as follows.

Capillary-flow measurements were used to determine the bulk viscosity of aqueous solutions both with and without PSS. These experiments are described in section 4.2.3.4. Aqueous solutions both with and without added PSS exhibited almost exactly the same flow rates, however, indicating that there is no significant difference in bulk solution viscosity between aqueous and PSS-containing solutions. These results indicate that the decrease in bimolecular reaction rates involving

PSS-bound ZnP^{+4} is not due to an increase in bulk solution viscosity upon addition of PSS.

The results of Rabani, et al., showed that the zwitterionic viologen BSV° was attracted to poly(vinyl sulfate) through dipole-induced interactions.[2a] If a similar attraction of PVS° occured in PSS solutions, the mobility of PVS° bound to PSS would decrease, which would lead to a decrease in bimolecular reaction rates involving PVS°.

Cyclic voltammetric measurements of PVS° reduction were performed in aqueous solutions both with and without added PSS. These experiments are described in section 4.2.3.5. In a linear potential sweep cyclic voltammetric experiment, the peak current at 25 C is given by the Randles-Sevik equation,

$$4.3.37) \qquad i_p = 2.69\times10^5\, n^{3/2}\, A\cdot D_0^{1/2}\, C_0^{*}\, v^{1/2},$$

where n is the number of electrons transferred, A is area of the electrode, D_0 is the diffusion coefficient of the electroactive species, C_0^* the bulk concentration of the species, and v the potential scan rate in volts/sec.[19]

Note that in the above equation, the peak current is proportional to $\sqrt{D_0}$. If significant association of PVS° by PSS occured, then the bulk diffusion coefficient of PVS° in solution would decrease, since the mass transport properties of PSS-bound PVS° species would certainly correspond to the mass transport properties of the bulky macroion. If PSS binding of PVS° occurs, then the diffusion coefficient, and hence i_p, would be decreased relative to aqueous solutions containing no PSS.

Cyclic voltammetric scans of the reduction of 1.4×10^{-3} M PVS° in 0.1M KCl solutions containing 5×10^{-3} eq/L PSS showed exactly the same peak currents as solutions without PSS, indicating that there is no significant association of PVS° with PSS under these conditions. These results lead to the conclusion that no significant association of PVS° by PSS occurs in solution.

4.5 Conclusions

Changes in the absorption spectrum of ZnP^{+4} that occur upon addition of PSS indicate that binding of ZnP^{+4} by PSS occurs. The spectral changes indicate that electrostatic "counterion" binding of ZnP^{+4} by PSS, resulting in strong association of these oppositely charged species. The red shift in the absoption maxima of PSS-bound ZnP^{+4} relative to aqueous solution indicates that the photosensitizer interacts with the hydrophobic aromatic "interior" of PSS.

Continuous photolysis experiments using ZnP^{+4} as photosensitizer, PVS° as sacrificial donor, and TEOA as sacrificial donor, were performed. The results of these experiments indicated that although the observed quantum yields in PSS containing solutions were slightly higher than homogeneous solutions, the overall quantum yield increase was not significant as compared to colliodal silica systems.

Flash photolysis experiments were performed to determine the effect of PSS and PolyP on the individual forward and back-electron

transfer reaction rate constants. The results of these experiments showed that all bimolecular rate constants involving PSS-bound ZnP^{+4} were decreased by a factor of 40-100 relative to homogeneous solution. These results are rationalized in terms of a hydrophobic "envelopment" of ZnP^{+4} by PSS, which sterically blocks approach of reactants, suppressing all bimolecular reactions involving PSS-bound species. PolyP addition caused a selective decrease in back-reaction rate only by a factor of ≈ 2.

4.6 References:

1) Bird, R. B., Stewart, W. E., Lightfood, E. N., " Transport Phenomena", Wiley, New York (1960)

2) Britz, S. J., Mackenzie, J. M. Jr., Briggs, W. R., Photochem. Photobiol. 25,137 (1977)

3) Duysens, L. N. M., Biochem. Biophys. Acta 19, 1(1956)

4) Otvos, J. W., Stone, H., Harp Jr., W. R., Spectrochimica Acta 9, 148 (1957)

5) Pasternack, R. F., Spire, E. G., Teach, M., J. Inorg. Nucl. Chem. 36, 599 (1974)

6) a) Barry, C. D., Hill, H. A. O., Mann, B. E., Sadler, P. J., Williams, R. J. P., J. Am. Chem. Soc. 95, 4545 (1973); b) Mauzerall, D., Biochemistry 4, 1801 (1965)

7) Pasternack, R. F., J. Am. Chem. Soc. 94, 4511 (1972)

8) Seeley, G. R., Jensen, R. G. Spectrochimica Acta 21,1835 (1966)

9) Tanford, C. "The Hydrophobic Effect. Formation of Micelles and Biological Membranes", Wiley, New York (1980)

10) a) Mandal, K., Hoffman, M. Z., J. Phys. Chem. 88, 5632 (1984); b) Ford, W. E., Otvos, J. W., Calvin, M. Nature 274, 507 (1978)

11) Chan, S. F., Chou, M., Creutz, C., Matsubara, T., Sutin, N. J. Am. Chem. Soc., 103, 369 (1981)

12) De Laive, P. J., Sullivan, B. P., Meyer, T. J., Whitten, D. G. J. Am. Chem. Soc., 101, 4007 (1979)

13) Rougee, N., Ebbesen, T., Ghetti, F., Bensasson, R. B., J. Phys. Chem. 86, 4404 (1982)

14) Schwarc, H. A., J. Phys. Chem. 86, 3431 (1982)

15) Turro, N. J., Okubo, T., J. Am. Chem. Soc. 104, 2985 (1982)

16) a) Kalyanasundaram, K., Newmann-Spallart, M., J. Phys. Chem. 86, 5163 (1982); b) Harriman, A., Porter, G., Richoux, M.-C., J. Chem. Soc. Faraday Trans. 2 , 77, 883 (1981)

17) Neta, P., J. Phys. Chem. 85, 667 (1981)

18) Turro, N. J., Tanimoto, Y., Photochem. Photobiol. 34, 173 (1981)

19) Bard, A., Faulkner, L, "Electrochemical Methods", J. Wiley, New York (1980) pp. 213-236

Appendix 4.1

Fortran Listing of Program INT.FOR Used to Simulate Transient Absorbance Data.

```
<
C       INTEG.FOR
C
C       A PROGRAM TO SIMULATE DATA DECAYING ACCORDING TO THE FOLLWING EQN.:
C
C
C       dX/dT = A*EXP(-BT)-CX**2
C
C
C
        Y1=0.
        X1=0.
        WRITE(6,30)
30      FORMAT(' ENTER Kq", Kq, Kb ')
        READ(5,40)RU,RF,R2
40      FORMAT(3E12.7)
        WRITE(6,90)
90      FORMAT(' enter time range of experiment')
        READ(5,100)RINTER
100     FORMAT(E12.7)
        RINTER=RINTER*.001
        WRITE(6,110)
110     FORMAT(' enter PVS conc. and ZNP* initial absorbance')
        READ(6,120)AO,PO
120     FORMAT(2E12.7)
C
C
C
        Z1=0.
        RA=RF*AO*PO*1.E-8/60800.
        B=(RU+RF)*AO
        C=R2*1.E-8
        INDX=1000
        WRITE(9,*)INDX
                DO 20 I=1,INDX
                SLOPE=RA*EXP(-B*X1)-C*Z1**2
                Y=Z1+SLOPE*RINTER*1.E8
                SLOPE2=RA*EXP(-B*(X1+RINTER))-C*Y**2
                SLOPER=(SLOPE+SLOPE2)*.5
                Z1=Z1+SLOPER*RINTER*1.E8
                Y1=Z1*12800.+.049*PO*EXP(-B*X1)
                WRITE(9,*)X1,Y1
                X1=X1+RINTER
20              CONTINUE
        END
```

Chapter 5: Alumina-Modified Silica Colloids as Charged Interfaces to Prevent Back-Reaction in Photoinduced Electron Transfer Reactions

5.1 Introduction

The use of charged interfacial systems such as micelles, vesicles and charged colliods to decrease back-reaction rates and increase quantum efficencies of photoinduced electron transfer reactions has been briefly discussed in chapter 1. The increase in overall quantum yield of oppositely charged photoproducts in continuous photolysis experiments performed in the presence of charged macromolecules is well documented.[1] The mechanism of the effect of these charged macromolecular systems on reaction rates between oppositely charged species is discussed in chapter 3. Primary salt effects act to decrease the activity of charged species in solution. This phenomenon is responsible for the observed decrease in back-reaction rates.

Colloidal silica sols has been found to be one of the most effective means increasing quantum yields in these photosystems. The observed increase in overall quantum yield in these interfacial systems is attributed to a decrease in the rate of back-reaction between the oppositely charged photoproducts formed in the initial electron transfer reaction. For the photoinduced electron transfer reaction between $^*Ru(bpy)_3^{+2}$ and PVS°, the bimolecular back-reaction rate constant is

decreased upon addition of colloidal silica over two orders of magnitude (from 7.9×10^{9} $M^{-1}s^{-1}$ to 5.7×10^{7} $M^{-1}s^{-1}$).[2] This decrease in back-reaction rate is accomplished without a significant decrease in the forward reaction rate.

The use of silica colloids in artificial photosynthetic systems, however, has been limited to high pH solutions, since silica sols are not stable in aqueous solution at neutral or acidic pH due to interparticle Si-O-Si bond formation that occurs as the repulsive negative charges on the silica particles decrease in acidic solution. The factors determining silica sol stability are discussed in greater detail in section 5.3.1.1. The instability of silica sols at neutral pH is a serious limitation in systems utilizing PVS° as electron acceptor, since the catalytic formation of H_2 from H^+ by reduced PVS° in solution is thermodynamically unfavorable at high pH ($E^{\circ}_{PVS^-/PVS^0} = -0.41$V vs. NHE).

Studies by Willner, et. al., have demonstrated that the problem of colloid instability in low pH media can be circumvented through the use of various bipyridinum analogs of PVS° which are capable of hydrogen reduction at high pH.[3] While these experiments show that hydrogen reduction by viologens in alkaline pH is possible, the experimental photolysis system is still limited to high pH by colloid instability. This chapter presents results of flash photolysis experiments using acid stable, alumina modified colloidal silica sols that are capable of preventing back-reaction between oppositely charged photoproducts throughout a

broad pH range without the corresponding loss of stability that unmodified sols experience at low pH.

The hydrophobic and electrostatic influences of macromolecular assemblies, particularly polyelectrolytes, have been outlined in chapter 3. While the discussion in chapter 3 focuses mainly on the influence of polyelectrolyte species on reaction rates, the theoretical treatment of the electrostatic effects of charged colliodal systems is basically the same as in the case of polyelectrolytes, i.e., salt effects are responsible for the dramatic decrease in reaction rates between oppositely charges ionic species in solution. This is discussed in greater detail in the following sections.

5.1.1 Previous Use of Colliodal Silica Sols in Artificial Photosynthetic Systems

5.1.1.1 Literature Review

The use of silica colloids in photoinduced electron transfer reactions was first reported by Willner, Otvos and Calvin.[2] Photosensitized reduction of PVS° by the photosensitizer $Ru(bpy)_3^{2+}$ was studied in the presence of a 40Å diameter silica colloid (Nalco *1115) and compared to the homogeneous system containing no colloid. Fluorescence quenching studies indicate that the quenching reaction of $*Ru(bpy)_3^{2+}$ by

PVS° is not affected by the colloid ($k_q = k_q' = 1.5\times10^9\ M^{-1}s^{-1}$, where k_q is the quenching rate constant in homogeneous solution and k_q' is the rate constant in solutions containing colloidal silica). Quenching of the $^*Ru(bpy)_3^{2+}$ by the positively charged electron acceptor methyl viologen (dimethyl-4,4'-bipyridinium chloride, MV^{2+}) is strongly enhanced by the addition of the colloid ($k_q' = 5\times10^{10}\ M^{-1}s^{-1}$ (with colloid) vs. $k_q = 5\times10^8\ M^{-1}s^{-1}$(Homogeneous solution)). The increase in quenching efficiency is attributed to electrostatic binding of both photosensitizer and acceptor on the negatively charged silica surface. Flow dialysis techniques were used to demonstrate the binding of the positively charged photosensitizer to the negatively charged silica surface ($K_{eq} = 1.1\times10^2\ M^{-1}$).[4]

Flash photolysis experiments indicate that the bimolecular rate constant of the back-reaction between the oppositely charged photoproducts, $Ru(bpy)_3^{3+}$ and $PVS^{-\cdot}$, is significantly retarded in the presence of the silica colloid ($k_b' = 5.7\times10^7\ M^{-1}s^{-1}$(with colloid), $k_b = 7.9\times10^9\ M^{-1}s^{-1}$(homogeneous solution)). The 140-fold decrease in back-reaction rate constant observed in colloidal silica solutions is currently the most effective means discovered to date for decreasing back-reaction rates which does not also significantly decrease forward-reaction rates. The fact that the forward-reaction rate constant (k_f) is not decreased is significant, as overall quantum yield in these artificial photosynthetic systems depends on the ratio of the forward- and

back-reaction rates, k_f/k_b. An increase in this ratio corresponds to an increase in overall quantum yield of initial photoproducts, which leads to an increase in the overall quantum yield of subsequent photoproducts as well, as can be demonstrated in the kinetic analysis given in section 4.3.3.1.

The activation energy of the back-reaction in the presence of the colloid was estimated to be 4.2 kcal mol^{-1} by a determination of the back-reaction rate as a function of temperature (this technique is discussed in section 5.3.3.4). This activation energy corresponds to a -180±20 mV potenial barrier for a singly charged reactant, which is in good agreement with the estimated surface potential (-170 mV) calculated using the known surface charge density of colliodal silica particles.[4] The importance of the surface potential of the colloid in decreasing back-reaction rates was demonstrated by varying the ionic strength and pH of the medium. These techniques are discussed in section 5.3.2.2.2. Back-reaction rates increased with increasing ionic strength and/or decreasing pH. Since both of these factors act to decrease the surface potential of the colloid, it was concluded that the high surface potental of the silica sol is responsible for the observed rate-reducing effects. The theory of electrostatic effects of charged particles on interionic reactions is discussed in section 5.1.2.

Studies by Yang of the effect of silica sols on the back-reaction between $ZnP^{+5\cdot}$ and $PVS^{-\cdot}$ show a similar effect, i.e., back-reaction rates

are significantly decreased in silica solutions without a corresponding decrease in forward-reaction rate.[5] The back-reaction rate constant was reduced from $(2.1\text{-}8.4)\times10^{9}$ $M^{-1}s^{-1}$ in homogeneous solution to 4.5×10^{7} $M^{-1}s^{-1}$ in the presence of silica sol. The back-reaction rate is decreased in the presence of silica by ≈100-fold.

In order to get an idea of the effectiveness of silica sols in these reaction systems it is necessary to compare the back-reaction rates and surface potentials of silica-containing systems with other charged particulate systems previously used to prevent back-reaction. In the past, micelles have been widely used as charged interfaces to prevent back-reaction in photoinduced electron-transfer reaction systems. For the back-reaction between $Ru(bpy)_3^{3+}$ and $PVS^{-\cdot}$, a modest ≈ 3-fold decrease in k_b is observed upon addition of 1.5×10^{-2} M sodium lauryl sulfate (k_b = 7.9×10^{9} $M^{-1}s^{-1}$ in homogeneous solution, k_b = 2.4×10^{9} $M^{-1}s^{-1}$ in micellar solution).[4] The small decrease in k_b in micellar solution is not nearly as significant as the 140-fold decrease observed in colloidal silica solution. The smaller effect observed in the micellar system is understandable when the surface potential of the micelle (≈-85 mV)[6] is compared to the much higher surface potential of the silica colloid (≈-180 mV). Assuming the potential barrier of the charged particle is the main energy barrier for the back-reaction, the larger decrease in k_b observed in colloidal silica solution relative to micellar solution is not unexpected.

In addition to the electrostatic influence of charged colloids on bimolecular reaction rates described above, the kinetics of reactions involving particle-bound species is influenced by both mass transport and geometric constraints which are imposed by the fact that one of the reactants is attached to the surface of a relatively large and bulky sphere. These constraints lead to a decrease in the rate of diffusion of the surface-bound species and limit the possible approach trajectories of reactant species in solution. These dimensional factors both lead to an expected decrease in bimolecular reaction rates involving the surface-bound species.

The calculation of the influence of electrostatic and dimensional effects on reaction rates is described in the following sections. It will be shown that the estimated decrease in back-reaction rate due to the influence of the electric field surrounding a charged silica particle is a much more significant factor than dimensional effects in determining the effect of charged silica particles reactions between oppositely charged species.

5.1.2 Theory of Electrostatic and Dimensional Effects of Charged Colliodal Particles on Interionic Reaction Rates

5.1.2.1 Introduction

The influence of macroions on interionic reaction rates has been described in chapter 3. Since charged colloidal particles are macroions, the effect of these macromolecules on interionic reactions should be calculable using the same techniques that are used for other polyionic systems. In many papers in the literature, the effect of charged particles on interionic reactions is described in terms of "electrostatic repulsion" of oppositely charged species in solution which physically seperates reactive species from each other in solution. It is not necessary to invoke this kind of behavior to account for the influence of charged particles, as repulsive interations and corresponding changes in "local concentration" are sucessfully described in terms of primary and secondary salt effects on interionic reaction rates outlined in chapter 3.

Since the dimensions and surface charge density of spherical charged particles can be determined readily, calculations of the effect of these particles on interionic reactions are simple compared to the calculations for polyelectrolyte effects. The electric field surrounding a charged particle is more easily modeled than the electric field surrounding a flexible polyelectrolyte. These calculations are given in the section 5.1.2.2.

In addition to the electrostatic effects of charged particles on interionic reactions, bimolecular reaction rates between surface-bound species and reactants in solution are decreased relative to the same reactions in homogeneous solutions because of the decrease in mobilty of the surface-bound species. The reduction in reaction dimensionality can

be accounted for in terms of collision and activated-complex therories of reaction rates. The derivation of the relationship between particle size and reaction rate for collision-controlled reactions is presented in section 5.1.2.2.1.

5.1.2.2 Electrostatic Effects of Charged Particles on Interionic Reactions

If the geometry and surface charge density of a colloidal system is known, it is possible to calculate the magnitude of their effect on interionic reactions in a relatively straightforward manner. These calculations are described in the next two sections. The magnitude of the electric field surrounding a charged spherical particle is first calculated using Gouy-Chapman-Stern theory. Once the surface potential is determined in this manner, transition-state theory can be used to determine the effect of the potential-induced changes in the energy of reactants and intermediates on reaction rates.

5.1.2.2.1 Calculation of the Electric Field Surrounding a Charged Particle

According to the model of Gouy and Chapman[7], the distribution of ions in the electrolyte solution surrounding a colloid particle is governed by the Poisson-Boltzmann equation. The derivation of the Gouy-Chapman

model of the the diffuse double layer of charges surrounding an ionic particle in solution is similar to the derivation used in the Debye-Hückel theory of simple electrolyte solutions; the difference is that the central ion point charge is replaced by a charged sphere. The Stern modification to the Gouy-Chapman model corrects for the layer of oppositely charged ions tightly bound to the charged sphere.

The modified Gouy-Chapman model relates the surface potential of a charged particle to the surface charge density of the particle and the bulk ionic strength by the following equation:

$$5.1.2) \qquad \sigma_s = [2DRT/\pi]^{1/2}\, C^{1/2} \sinh [F\Psi/2RT],$$

where σ_s is the surface charge density of the particle in coulomb m^{-2}, Ψ is the surface potential in volts, D is the dielectric constant of the solvent (78.5 for water), R is the universal gas constant (8.3 J mol^{-1} deg^{-1}), T is the temperature in degrees Kelvin, C is the concentration of electrolyte, and F is the Faraday constant (96,500 Coulombs mol^{-1}). If the ionic strength and surface charge density are known, Ψ can be easily calculated using this equation. Note the inverse relationship between ionic strength and surface potential. This will become important later in the discussion of the effect of ioinic strength on surface potentials and reaction rates.

The calculated surface potential of a charged particle is used to

estimate the influence of charged colloids on the rates of interionic reactions in next section.

5.1.2.2.2 Influence of the Electric Field Surrounding Charged Colliodal Particles on Interionic Reaction Rates

The influence of the electric field of a charged particle on interionic reaction rates between oppositely charged species can be derived using activated complex theory provided a few reasonable assumptions are made. First, it must be assumed that one of the charged reactants (opposite in charge relative to the particle) is bound to the surface of the charged particle by electrostatic forces. The oppositely charged reactant in solution must overcome the potential barrier of the charged particle in order to react with the bound reactant. The additional energy requirement to surmount this barrier increases the activation energy of the reaction since the electric field of the particle acts to repel the similarly charged reactant in solution.

Before the magnitude of this effect can be calculated, two more assumptions must be made. The relative number of oppositely charged reactant molecules bound to the particle must be small compared to the total number of charges on the particle. If this is not the case, then the charge density of the particle will be less than the estimated charge

density. The second assumption is that total binding of the oppositely charged reactant occurs to insure that no reaction between oppositely charged reactant occurs in the bulk solution. Both of these assumptions are true if a large relative number of particle binding sites per oppositely charged reactant species is maintained. If this is the case, then the equilibuium between bound and unbound reactant is driven towards complete binding, and the decrease in surface charge density caused by reactant condensation on the particle surface is small enough to be neglected in the calculations.

The effect of surface potential on reaction rates can be modeled using transition-state theory. For the case where a reactant is bound to a charged surface the reactant in solution must migrate through the potential barrier induced by the particle before reaction with the surface bound species can occur. The rate of this migration is governed by the Eyring equation:

$$5.1.3) \qquad k_1 = (kT/h) \exp[- \Delta G^{\ddagger} /RT]$$

where k is the boltzmann constant, T is the temperature, h is plank's constant, R is the gas constant, and $\Delta G^{\ddagger}$ is the free energy of activation.

The change in the free energy of activation due to the electrical double layer surrounding the particle is equal to the work required to transport the charged reactant across the potential barrier. This work is related to the surface potential by the following expression:

5.1.4) $\Delta G^{\ddagger} = z_r e\Psi$

where z_r is the valency of the reactant in solution and e is the electronic charge (1.602×10^{-19} C). This expression, when combined with equation 5.1.3, relates the reaction rate to the surface potential. For a singly charged reactant in solution. This expression is given by

5.1.5) $k_1 = A \exp[-e\Psi/RT]$ $(A = kT/h.)$

The effect of surface potential on relative reaction rates for the bimolecular reaction between a surface-bound reactant and a single oppositely-charged reactant in solution is shown in figure 5.1.1. k/k^* is the ratio of the rate constant in homogeneous solution to the rate constant in the presence of a charged surface with the indicated surface potential. When the ratio of rates is expressed in this way, the A term in equation 5.1.5 cancels, and the resulting ratio is expressed dimensionlessly.

In figure 5.1.1, k/k^* is plotted on a logarithmic scale so as to better show the influence of potential throughout the range plotted. Note that when the surface is ≈60 mV, the ratio of rates is ≈10, wheras when the surface potential is 120 mV, the ratio jumps to ≈100. Clearly, in order for the charged surface to have a significant effect on reaction rate,

the surface potential must be above ≈100mV.

In order to compare the effect of charged colloids with different surface charge density on reaction rates, equations 5.1.2 and 5.1.5 have been used to calculate k/k^* for a range of surface charge densities. The results are shown in figure 5.1.2. In this figure charge density is expressed in charges per square nanometer of surface area rather than coulombs per square meter, as in equation 5.1.2. For reference, the surface charge densities and calculated k/k^* for both silica (-170mV)[4] and SDS micellar (-85 mV)[6] colloidal systems have been noted.

Figure 5.1.2 shows that surfaces with charge densities greater than ≈1 charge/nm^2 are needed in order to obtain k/k^* ratios near 10^3. Micelles have a surface charge density of ≈0.3 charges/nm^2, therefore these macromolecular assemblies are expected to exhibit a maximum of only an approximate ≈30 fold decrease in reaction rates for singly charged reactants in solutions.

The surface chemistry of colliodal silica is discussed in section 5.2. Based on the literature value of the surface charge density of silica colloids (0.18 C m^{-2}, 1.12 charges nm^{-2}),[8] the effect of these sols on interionic reaction rates is predicted to be quite dramatic. Bimolecular interionic reaction rates between oppositely charged species are expected to be decreased by almost three orders of magnitude for the reaction between surface-bound species and singly charged reactants in solution. Reports by Willner and co-workers (see section 5.1.1.1) regarding the effect of silica sols on the electron-transfer reaction between

Figure 5.1.1

Effect of Surface Potential on Reaction Rate

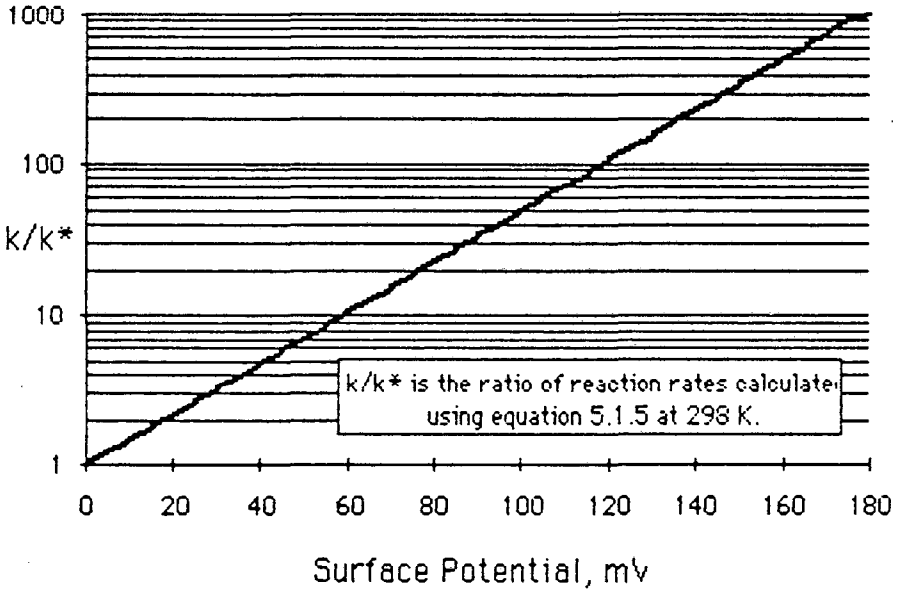

Figure 5.1.2

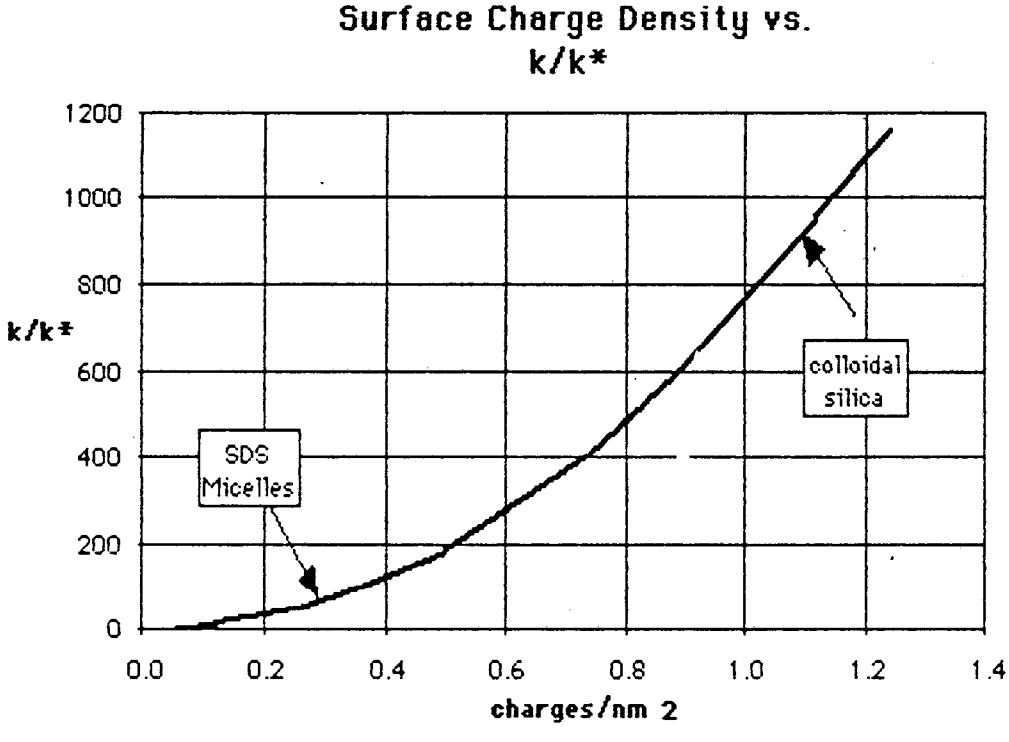

k/k* calculated using equation 5.1.2 and 5.1.5 for 0.1 M ionic strength solution at 298 K.

$Ru(bpy)_3^{+2}$ and PVS° have confirmed that the predicted decrease in reaction rates actually occurs. The present work also presents results of flash photolysis experiments that confirm that the electrostatic model presented above is valid for the photoinduced electron transfer reaction between ZnP^{+4} and PVS° in the presence of both unmodified and alumina-modified silica sols. These results are presented in section 5.3.

In addition to the electrostatic influence of charged colloidal particles on interionic reaction rates, dimensional effects on bimolecular reaction rates caused by one of the reactants being bound to the surface of a colloidal particle may also be responsible for a decrease in bimolecular reaction rates. These dimensional effects are discussed in the following sections.

5.1.2.3 Influence of Dimensionality on Bimolecular Reaction Rates Involving a Surface-bound Reactant

When one of the reactants involved in a bimolecular reaction is localized on the surface of a macromolecular spherical particle of dimensions much greater than the dimensions of the bound reactive molecule, the bimolecular reaction rate between the surface-bound species and other reactive, unbound species is reduced due to the decrease in mobility of the surface bound species. The decrease in reaction rate that

is induced by the change in dimensionality (from three dimensions in solution to two dimensions on the surface) can be accounted for using the collision-control theory of bimolecular reactions.

Qualitatively, a reduction in reaction rate seems reasonable considering the large increase in effective mass of one of the reactants that occurs upon binding to the much more massive particle. In addition to this decrease in mobility caused by the increase in effective mass experienced by the bound reactant, the approach of unbound reactant species in solution to the surface bound species is limited to trajectories that are nearly perpendicular to the surface of the particle. This geometric constraint together with the mass-induced decrease in reactant mobility are both expected to lead to a decrease in reaction rates involving surface-bound species.

In the following section, the geometric and mass-transport effects caused by the localization of one of the reactants of a bimolecular reaction is analyzed using collision-control theory. The geometric constraints induced by surface binding are shown to lead to a decrease in bimolecular reaction rates involving surface-bound species and reactants in solution.

5.1.3.2.1 Theoretical Calculation of Dimensional Influences on Bimolecular Reaction Rates

The theoretical treatment that follows is based on the derivation of geometric effects of the reduction of dimensionality in interfacial reactions given published by Astumian and Schelly.[9] Consider the bimolecular reaction

5.1.6) $A + B \xrightarrow{k} C.$

If B is localized on the surface of a particle, the corresponding heterogeneous reaction can be written as

5.1.7) $A + B_s \xrightarrow{k^*} C_s \longrightarrow$ products

where B_s and C_s is the surface-bound reactant and intermediate, respectively. The bimolecular rate constants for the homogeneous and heterogeneous reactions are k and k*, respectively. According to simple collision theory[10], the rate of reaction 5.1.6 is

5.1.8) $-(dN_A/dt) = N_A N_B V^{-1} [(8\pi kT/\mu_{AB})^{1/2} \sigma_{AB}^2 \exp(-E_a/kT)]$

where σ_{AB}^2 is the effective collision cross-section (approximated by $\sigma_{AB}^2 \approx (r_A+r_B)^2$), and $\mu_{AB} = (m_A m_B/(m_A+m_B))$ is the reduced mass of A and B. The term in brackets is the bimolecular rate constant k. Collision

theory assumes that the concentration of reactants in solution is uniform throughout. This is not true in the case of diffusion-controlled reactions.

For the heterogeneous reaction depicted in equation 5.1.7, if the entire surface of the particles is covered with reactant (this assumption only simplifies the derivation and will be removed later), the number of collisions between A and surface-bound B species is

$$5.1.9) \qquad Z_{A\text{-}B_s} = N_A N_P V^{-2}(8\pi kT/\mu_{A\text{-}P})^{1/2}\,(r_A+r_P)^2$$

where N_P and r_P refer to the number and radius of the large particles. Assuming the mass and radius of the particle is much greater than those of the reactants, then $\mu_{A\text{-}P} \approx m_A$ and $(r_A+r_P)^2 \approx r_P^2$. The total area available for collision of A with surface bound B is

$$5.1.10) \qquad \text{Area} = 4\pi\, r_P^2\, N_P = (2r_B)^2\, N_B$$

assuming cubic close packing of B on the surface of the particles. This packing restraint is removed by simple increasing r_P at fixed N_P. Since it will turn out that the resultant decrease in reaction rate is independent of the diameter of the particle, the results are applicable to systems in which there is not close-packing of the surface with reactant. The inclusion of this constraint here simplifies the derivation, so it is

included here.

Using equations 5.1.9 and 5.1.10 in a rate expression analagous to equation 5.1.8 gives

$$5.1.11) \quad -(dN_A/dt) = N_A N_B V^{-1} [(8\pi kT/m_A)^{1/2} r_B^2 \exp(-E^*_a/kT)]$$

where E^*_a is the activation energy for the heterogeneous reaction and the experession in brackets is k^*.

The ratio of rate constants can be determined by combining equations 5.1.8 , 5.1.10 and 5.1.11 to give

$$5.1.12) \quad k^*/k = \pi^{-1}[m_A/(m_A+m_B)]^{1/2} [r_B/(r_A+ r_B)]^2 \exp(-\Delta E_a/kT)$$

where ΔE_a is the difference in activation energies between the homogeneous and heterogeneous reactions.

The exponential term represents the energetic reason for the change in rate observed in colloidal systems which was discussed in sections 5.1.2.2. The factors of π^{-1} and $[r_B/(r_A+ r_B)]^2$ are the result of the geometric constraints of the reaction system that occur when B is attached to a large particle, i.e., collisions of A species with surface-bound B species do not occur from other than perpendicular trajectories with respect to the plane of the particle surface. The factor

$[m_A/(m_A+m_B)]^{1/2}$ arises from the increase in effective mass of the surface-bound reactant, which acts to decrease the mobility of B in solution.

Both the geometric and mass factors in equation 5.1.12 are always less than one, meaning that a decrease in reaction rate should be induced by these factors when a reactant involved in a bimolecular reaction is bound to a large particle. Given reasonable molecular dimensions and masses, a maximum of a 50-fold decrease in reaction rate is expected to be possible due to these geometric and mass transport considerations.

Note that no explicit dependence of reaction rate on the size of the particle is predicted. This implies that as long as the assumptions stated above hold ($\mu_{A-P} \approx m_A$, $(r_A+r_P)^2 \approx r_P^2$) an increase in particle size will not lead to a decrease in reaction rate. This is an important conclusion in terms of the design of colloidal systems to be used for the prevention of back-reaction in artificial photosynthetic systems. There is no advantage in using larger diameter particles as far as decreasing back-reaction is concerned. There are advantages in using smaller particles, however. The surface area/volume ratio of smaller particles is greater, so less mass of particles is needed to obtain the needed surface area. The light scattering of smaller diameter particles is less (per unit surface area) than for larger diameter particles, so light scattering problems that are sometimes associated with the characterization of the effects of collidal systems using optical methods can be avoided.

The derivation of dimensional effects for diffusion-controlled reactions will not be presented here, since those results have no direct bearing on the reactions discussed in this thesis. The results of the theoretical treatment are interesting, however, in that it turns out that there is an effect of particle size on reaction rate for diffusion-controlled reactions. The ratio of rates is given by

$$5.1.13) \quad k^*/k = r_B^2/\pi r_P (r_A + r_B)^2$$

In the case of diffusion-controlled reactions, then, there is an express dependence of k^*/k on the diameter of the particle. Using typical molecular radii and a colloid size of 1 μm, the ratio of rates is $\approx 10^5$, which indicates that the dimensional effect is much more pronounced in the case of diffusion-controlled reactions than it is for collision-controlled reactions.

5.1.2.4 Summary

The preceding sections have described both electrostatic and dimensional effects on reaction rates which result from the binding of one reactant on the surface of a charged colloidal particle. The potential gradient which reactants in solution must overcome to react with surface bound species can influence reactant rates significantly. Bimolecular

reaction rates between oppositely charged species can be decreased as much as $\approx 10^3$-fold relative to the same reaction in homogeneous solution. The magnitude of the electrostatic effect is proportional to the magnitude of the surface potential. This is related to the surface charge density. The surface potential can be varied by altering either the surface charge density of the particle or by changing the ionic strength of the medium surrounding the particle.

Geometric and mass-transport constraints imposed by anchoring one of the reactants to a spherical colloidal particle also act to decrease bimolecular reaction rates between surface-bound species and reactants in solution. This effect is independent of the surface potential of the colloid. For collision-controlled reactions, the effect is also independent of the size of the colloidal particle involved. The dimensional constraints imposed lead to an estimated 10-100-fold decrease in specific bimolecular reaction rates.

Flash photolysis experiments were performed in which the effect of silica sol particle size on back-reaction rates were studied. These are discussed in section 5.3.3.1. The prediction that there is no dependence of reaction rate on particle size for collision-controlled reaction is confirmed by these experiments. For particle systems of 7, 12 and 22 nm diameter, back-reaction rates were found not to depend on the particle size.

5.1.2.5 Conclusions

While both electrostatic and dimensional effects act to decrease bimolecular reaction rates between oppositely charged species, the calculations of the relative magnitudes of the effects indicate that, for reasonably highly charged colloids, electrostatic effects will predominate over dimensional effects. Although the two effects occur simultaneously, they can be distinguished from each other readily by utilizing the fact that the electrostatic effect is a function of ionic strength, wheras the dimensional effect is independent of ionic concentration.

The following section describes the physical and chemical properties of the colloidal silica sols used in this study. The surface charge density and acidity of these sols are two factors which influence the effectiveness of these particles in preventing back-reaction in artificial photosynthetic systems. The effect of surface alumina modification on these properties is discussed. Alumina modification is shown to increase both the surface charge density and stability of silica particles at neutral and acidic pH. The increase in stability and charge density allows the use of alumina modified particles throughout a wider pH range (pH 3-11) than unmodified silica sols.

5.2 Physical and Chemical Properties of Ludox Colloidal Silica Sols

As discussed in section 5.1, the high surface charge density on the surface of silica particles makes them useful as charged interfaces for retarding back-reaction between oppositely charged photoproducts in photolysis experiments. The nature of the charged surface of silica sols is discussed in the following sections. The chemistry of unmodified silica sols similar to those used by Willner, et. al.,[2] to prevent back-reaction in artificial photosynthetic systems will be compared to the chemistry of alumina-modified silica sols. The higher surface acidity of alumina-modified sols allows the use of these colloids throughout a broader pH range than unmodified silica, increasing the usefulness of colloidal systems considerably. Before the effect of alumina modification is discussed, the nature of the unmodified silica surface is described in the following section.

5.2.1 Unmodified Ludox Sols

Ludox colloidal silica is an aqueous colloidal dispersion of silica particles. The particles in Ludox sols are discrete, uniformly sized spheres of 7, 12 or 22 nm diameter which have no detectable internal surface area or crystallinity as determined by electron microscopy and gas adsorption measurements.[11] The sols are dispersed in an alkaline medium

which maintains a strong negatively charged surface through deprotonation of surface SiOH groups. The high surface charge density acts to decrease interparticle collisions through electrostatic particle-particle repulsion and thus stabilize the suspension by decreasing the rate of interparticle Si-O-Si bond formation.

5.2.1.1 Commercial Preparation

The preparation of uniformly sized silica sols is described in a patent by Iler and Wolter.[12] The process involves removing excess alkali from a solution of alkali metal silicate using a cation exchange resin. Throughout the preparation of the sol, the pH of the solution is kept basic. The equilibrium processes involved in the precipitation of silica from silicate solution are described by the following three reactions.

5.2.1) $Na_2H_2(SiO_4) + H_2O \rightleftarrows NaH_3SiO_4 + OH^- + Na^+$

5.2.2) $NaH_3SiO_4 + H_2O \rightleftarrows Si(OH)_4 + OH^- + Na^+$

5.2.3) $Si(OH)_4 \rightleftarrows (SiO_2)_{solid} + 2H_2O$

The mechanism of precipitation of silicate using ion-exchange techniques can be deduced from the equilibrium expressions above. Exchange of Na^+ for H^+ on the resin shifts the equilibria described by equations 5.2.1 and 5.2.2 to the right through the removal of Na^+ and the

release of H^+. A further shift in in the equilibrium occurs due to the neutralization of OH^- by the H^+ released from the resin upon binding of Na^+.

The colloidal particle thus created has been demonstrated to be composed of amorphous silica (density 2.20gm/cm^3). In the bulk of the particle, every silicon atom is tetrahedrally coordinated by oxygen atoms, therefore the bonding in the interior of the particle consists entirely of strong (799 kJ/mole) Si-O-Si bonds.[13]

The tetrahedral coordination of surface silicon atoms is maintained by internal Si-O-Si bonds and by one or more surface Si-OH bonds.[14] These surface hydroxyl groups are responsible for the charge that develops on the silica particle surface in high pH media. The nature of these groups is discussed in the following section.

5.2.1.2 Surface Charge Density

Potentiometric titration and electrophoretic mobility measurements of Ludox HS colloidal silica sol (particle diameter 12 nm) have demonstrated that the isoelectric point of commercially prepared silica particles is somewhere between pH 1 and 2.[15] Above this pH range, exchange of Na^+ for silanolic protons occurs. This leads to an increase in the surface charge density of the silica surface. The larger, less electronegative Na^+ ions cannot enter into the electronic structure of the $Si-O^-$ ion and are much more readily hydrated, thus ionization of the

surface increases.

5.2.1.3 Acidity of Surface Silanol Groups

Potentiometric titrations of the surface silanol groups of Ludox sols have been performed to determine the apparent pK of the exchangable ionic sites on the silica surface.[14] Analysis of data obtained by titrating ion-exchanged Ludox HS samples with NaOH have shown that a single equilibrium reaction cannot be used to describe the exchange of Na^+ for H^+ on the silica surface. A mathematical model was developed in which two different kinds of exchange sites were present on the silica surface and in which the apparent equilibrium constants varied with the surface charge density. This model gave a reasonable fit to the titration data with apparent pK values of 5.5 and 9.0.

The model is not unreasonable considering the following facts: Studies have shown that the surface silanol groups on silica sols are of three different kinds. Silanol groups with one, two or three exposed Si-OH groups are possible ($-Si(OH)_3$, $=Si(OH)_2$, and $\equiv Si-OH$). The surface charge density of the sol increases as the extent of cation exchange increases, which tends to decrease the acidity of the remaining silanolic protons. This phenomenon has been demonstrated in coulombic titrations of silica sols.[16]

The high surface charge density of silica sols is largely responsible for the stability of these colloids, as will be shown in the next section.

5.2.1.4 Stability of Silica Sols

Colloidally dispersed silica sols are unstable at low pH due to the formation of interparticle Si-O-Si bonds. The formation of these bonds holds the particles in fixed positions relative to each other and results in the formation of a rigid, highly porous, tangled network of branching chains known as a gel. The driving force behind gel formation is the stability of the Si-O-Si bond.

The rate of gel formation is a function of both the pH and the ionic strength of the colloidal solution. The mechanism of the formation of Si-O-Si bonds involves interparticle collision and loss of a water molecule which is depicted in the following equation.

5.2.4) $$2{\equiv}Si\text{-}OH \longrightarrow {\equiv}Si\text{-}O\text{-}Si{\equiv} + H_2O$$

The stability of silica sols decreases as the ionic strength of the solution is increased. This is due to an increase in interparticle collisions caused by the decrease in the magnitude of the electric field surrounding the particle in higher ionic strength media.

Since the surface charge density is strongly dependent on pH, the stability of silica sols is also decreased as the pH of the solution decreases. A minimum in the stability occurs at pH $\approx$7, below which stability increases again. The minimum in the pH stability curve, shown

below for a typical unmodified silica colloid, does not occur at the pH at which the surface charge density is at a minimum (pH 1-2). An additional factor is important in determining sol stability in addition to suface charge density. This factor is discussed below.

When the colloid is the least stable (≈pH 7), both $Si-O^-$ and Si-OH groups are present on the colloid surface. Below this pH, the increase in H^+ concentration results in protonation of ionized surface silanol groups. This leads to a decrease in the concentration of surface $Si-O^-$ groups. In high pH solutions, the opposite is observed, i.e., deprotonation of surface silanol groups occurs which leads to a decrease in Si-OH surface groups. The observed decrease in stability at neutral pH has been proposed to be due to interparticle hydrogen bond formation that occurs when both protonated and unprotonated surface silanol groups are present on the silica surface.[17] Gel formation has been proposed to occur via the following steps;

5.2.5) $\equiv Si-OH + {}^-O-Si\equiv \longrightarrow \equiv Si-OH\cdots\cdots{}^-O-Si\equiv$

5.2.6) $\equiv Si-OH\cdots\cdots{}^-O-Si\equiv \longrightarrow \equiv Si-O-Si\equiv + OH^-$

Note that in equation 5.2.5 both Si-OH and $Si-O^-$ moieties are necessary for intermediate formation. This mechanism accounts for the stability of unmodified silica sols in both high and low pH media.

As discussed in section 5.1, the goal of the studies of silica sols

is to find new systems which would be stable over a wider pH range than colloidal silica. The stability of alumina-modified colloidal silica sols in neutral and acidic media is described in the following section.

5.2.2 Alumina Modified Colloidal Silica Sols

Reaction of the surface of an silica sol with aluminate ion leads to the incorporation of aluminosilicate anionic sites onto the surface of the sol. The negative charges introduced onto the silica surface by this process create a fixed negative charge independent of pH from pH 3-11. These fixed charges are in addition to the pH-dependent charges resulting from deprotonation of remaining surface silanol groups. The strong acidity of the additional aluminosilicate groups increases the stability of the resultant sol at neutral and acidic pH by increasing the surface charge density of the particle in the lower pH range.

5.2.2.1 Commercial Preparation

Alumina-modified sols are prepared by reacting sodium aluminate with the surface of a commercially available unmodified sol such as Ludox HS.[18] This reaction is represented as follows:[19]

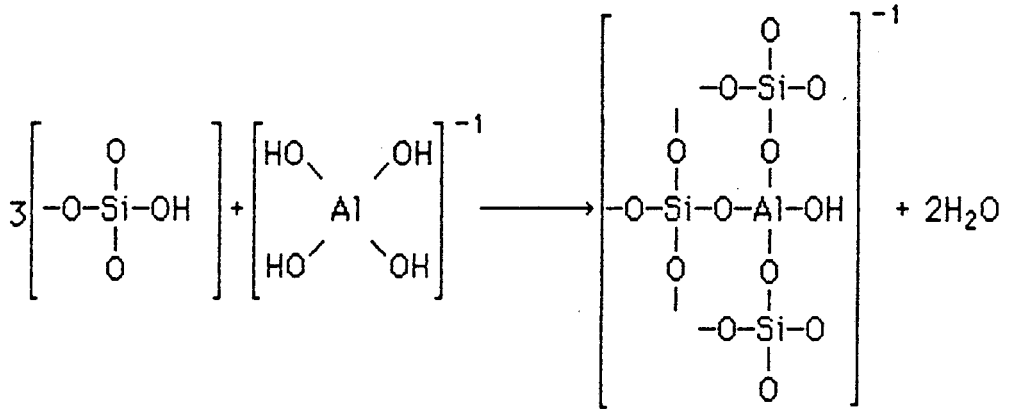

Incorporation of alumina occurs exclusively on the surface of the pre-formed colloidal particle. The amount of alumina incorporated onto the silica surface, expressed as the percentage of the amount that is theoretically required to deposit one aluminum atom on every silicon atom (8 Si/nm^2), is typically ≈ 4% for Ludox AM, a 12 nm modified silica colloid prepared from Ludox HS.

The incorporation of anionic, four-coordinate aluminum into silica was first observed by Pauling in crystalline minerals [20] and soon afterwards in alumina-silica cracking catalysts.[21] The resultant increase in surface charge density and consequential increase in sol stability at neutral and acidic pH is discussed in the following sections.

5.2.2.2 Surface Acidity of Alumina-Modified Silica Sols

The pK_a of the alumina sites on a modified silica sol surface can be estimated by comparing the acid-catalysis cracking activity of aluminum-modified silica (in the form of alumina-silica cracking catalysts) with the catalytic activity of strong acids.[22] For the cracking of isopropyl benzene, the relative activity of alumina-modified silica was determined to be between the activity of perchloric acid ($pK_a \approx -8$) and silicotungstic acid, which indicates that the aluminosilicate acid species is indeed a very strong acid. In aqueous solution the alumina sites are expected to be completely dissociated regardless of pH.

5.2.2.3 Stability of Alumina Modified Silica Sols Compared to Unmodified Silica

As discussed in section 5.2.1.4, the stability of silica sols decreases sharply upon decreasing the pH of the medium. The decrease in surface charge density accompanying the drop in pH increases interparticle collision rates. This leads to an increase in interparticle Si-O-Si bond formation and subsequent gel formation.

The substitution of alumina on the surface of silica sols introduces highly acidic sites which cannot be removed or neutralized in low pH media. The permanent surface charge density associated with these sites leads to an increase in sol stability throughout the pH range of 3-11. The

increase in stability is especially evident at low pH.

Figure 5.2.1 depicts the relative stability of both alumina-modified (Ludox AM) and unmodified (Ludox HS) silica sols. These two sols are compared because they both have the same particle diameter (12 nm).

Note that although the unmodified sol has a minimum in stability around pH 5.5, the stability of the alumina modified sol continually increases as the pH is lowered. The lack of a minimum in the curve for the alumina-modified sol is indicative of the fact that even at pH 5.5, where gelling is a maximum for the underivatized colloid, the surface charge density on the alumina modified sol is still great enough to prevent coagulation. The stability of both the alumina-modified and the underivatized sols increases below pH 5.5 due to the decrease in surface $Si-O^-$ groups necessary for interparticle hydrogen bond formation (see section 5.2.1.4).

5.2.3 Summary

The incorporation of strongly acidic alumina sites on the surface of silica colloids leads to an increase in the surface charge density of the colloids in neutral and acidic media. This increases the utility of these sols as charged interfaces for decreasing back-reaction between oppositely charged photoproducts in photoinduced electron-transfer schemes by widening the pH range in which these colloids can be used.

Figure 5.2.1

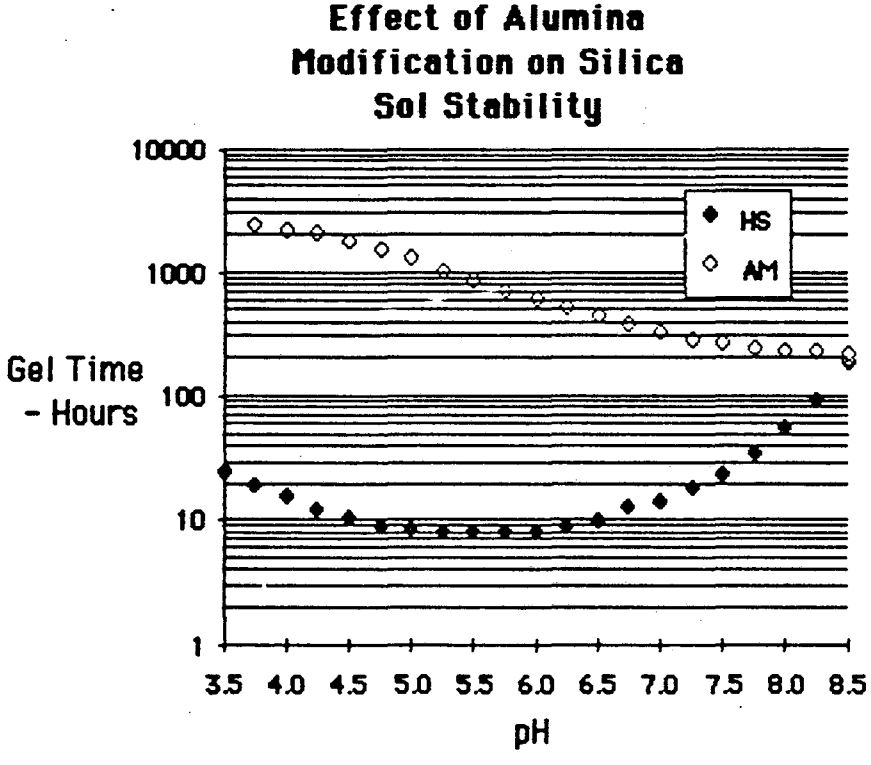

HS = Unmodified Colloidal Silica, 12 nm particle diameter

AM = Alumina-Modified Colloidal Silica, 12 nm particle diameter.

Gel times determined in 30 % SiO_2 solids solution containing 0.01 N NaCl. Data used to construct above chart obtained from the manufacturer of Ludox AM and HS.[11]

The ultimate solar energy storage system that is one of the long-term goals of this research will probably not utilize the photosensitizer or electron relays used in this study. The discovery of a charged interfacial system with stability over a wide pH range is potentially useful in photosensitized electron transfer reaction systems of this kind regardless of the particular components used in the reaction. The electrostatic and dimensional arguments presented above are equally valid for other photoredox systems in which oppositely charged photoproducts are formed.

The following section describes flash photolysis experiments that demonstrate the rate-retarding influence of alumina-modified silica sols at neutral pH for the photoredox reaction between ZnP^{+4} and PVS°. Alumina-modified colloids offer significant advantages over unmodified silica sols for the following reason: Reduced PVS^- anion is incapable of hydrogen reduction above pH 6.93 ($E_{0_{PVS/PVS^-}}$ = -0.41V vs. NHE). Since underivatized colloidal silica is unstable between pH 5 and 7, it cannot be used in hydrogen generating photolysis systems that use PVS as the reversible electron acceptor. Alumina-modified silica sols, however, are stable at pH 7, therfore they can be utilized to increase overall quantum yields in photolysis systems using PVS°.

5.3. Effect of Alumina-Modified Colloidal Silica Sols on The Photoinduced Electron Transfer Reaction Between ZnP^{+4} and PVS°

5.3.1 Introduction

This section describes experiments designed to probe the influence of both alumina-modified and unmodified colloidal silica sols on the individual forward- and back- electron transfer reactions between the photosensitizer ZnP^{+4} and the reversible electron acceptor PVS°. The results of these experiments confirm the hypothesis that alumina-modified silica colloids exert the same dramatic back-reaction rate retarding effect that unmodified silica sols do. The observed decrease in back-reaction rates in the case of alumina-modified sols occurs throughout the pH range of 6-9, thereby significantly extending the useful pH range in which silica sols can be used.

5.3.2 Experimental Section

5.3.2.1 Materials

All materials, unless otherwise specified below, were prepared as described in section 2.1.

5.3.2.2 Purification and Characterization of Colloidal Silica Sols

du Pont Ludox colloidal silica sols were a gift from the manufacturer. They were cleaned by an ion-exchange technique originally developed to purify polystyrene latex emulsions. [23] This procedure removes any ionic impurities present in the sol as it is supplied by the manufacturer. In order to insure that no ionic or polyelectrolyte impurities were introdued by the ion-exchange resins during the clean-up procedure, the Dowex 1-X4 anion exchange resin and Dowex 50-X4 anion exchange resins (50 mesh) were purified as follows. ≈50 gms of one of the resins is loaded into a large Büchner funnel equipped with a mechanicial stirrer as shown in figure 5.3.1. The resin is washed and rinsed with the following sequence of solutions;

1)	Wash:	Hot (>80 C) deionized water
2)	Wash:	Methanol
3)	Rinse:	deionized water (3 times)
4)	Wash:	3N NaOH
5)	Rinse:	deionized water (3 times)
6)	Wash:	3N HCl
7)	Rinse:	deionized water (3 times)
8)	Wash	3N NaOH

9) Rinse: deionized water (3 times)

10) Wash: 3N HCl

11) Rinse: deionized water (3 times)

Wash = fill the funnel with the appropriate solution, stir for about 30 min, then suction filter solution into vacuum flask. During the washing procedure the vacuum line must be plugged or the stopcock closed so that the wash solution will remain in the Büchner funnel for the entire wash.

Rinse = Fill the funnel with deionized water and stir for 1-5 minutes, then vacuum filter the rinse solution into the vacuum flask.

After this purification procedure, the resins may be stored for several weeks before the purification procedure needs to be performed again. It is important that the anion exchange resin is stored in the Cl^- form, as it is unstable in the OH^- form. Just before using the purified resins for sol purification, the anion exchange resin is washed in 3N NaOH and rinses with deionized water. Equal amounts of the anion and cation exchange resins are then mixed together and the silica sol to be purified is added. The mixture is stirred for about 30 minutes, and the purified sol is subsequently separated from the resins by filtration. After purification the pH of the sol is usually $\approx$2.5. 1.0 N NaOH is added to bring the pH to the desired value.

Figure 5.3.1
Apparatus for Cleaning Ion-Exchange Resins

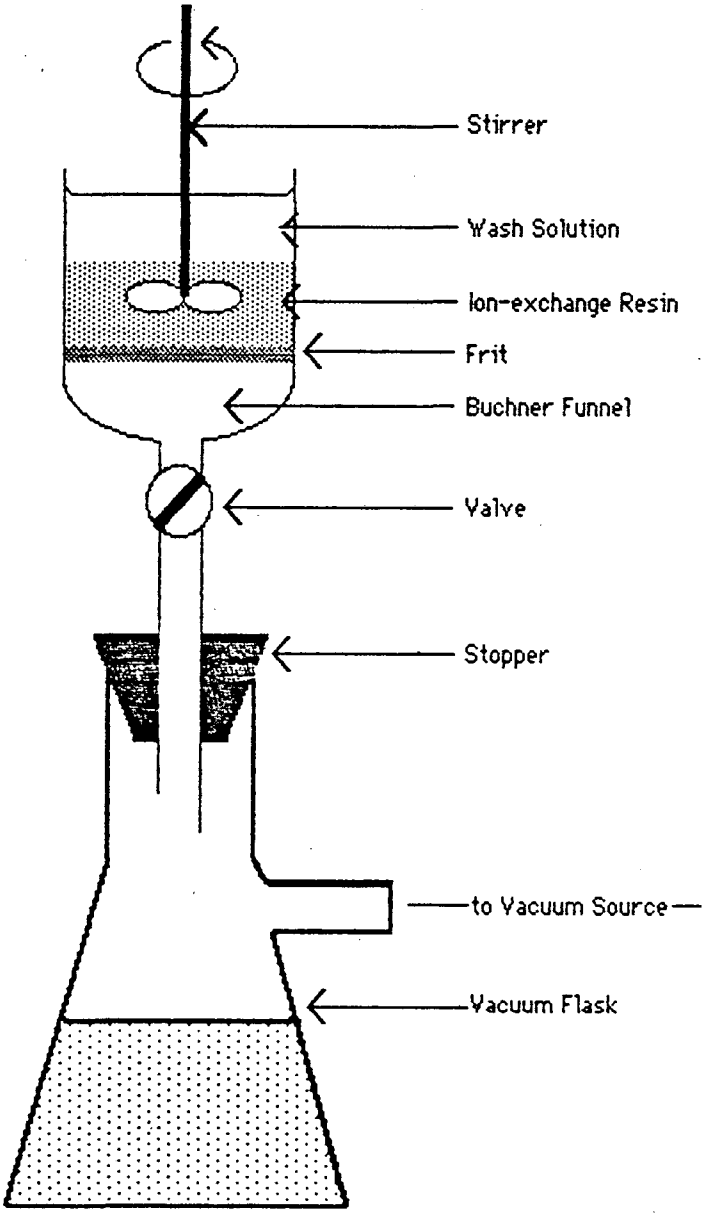

Dry weight analysis of the purified sols is performed by pipetting 3-10 ml of the sol into a tared scintillation vial and heating at 140 C for 2 or more days until a constant weight is achieved.

Once the weight percent of solids is determined as described above, the purified colloid solutions are diluted with water to a stock solution concentration of 5.0 gms dry weight/100 ml (5.0% w/v).

The determination of the specific surface area of unmodified Ludox sols is performed by NaOH titration of the ionizable SiOH groups on the surface of the sols. This empirical procedure that follows was obtained from the manufacturer (du Pont) and has been calibrated by them using duplicate determinations of surface area by nitrogen absorption (B.E.T.) analysis.[24] The titration procedure is as follows:

A sample of colloidal silica sol containing approximately 1.5 gms of of SiO_2 is purified by ion-exchange as described prevously. The volume of the solution to be titrated is diluted to ≈100 ml and 20 gms of reagent grade NaCl is added. This solution is titrated with 0.1 N NaOH. The number of equivalents of base required to change the pH from 4.0 to 9.0 is empirically related to the surface area in m^2/gm by the following relationship:

$$\text{Area } (m^2/gm) = A(\text{eq.}) \times [3.97 \times 10^5 \ m^2/\text{eq.}]/B(\text{gms})$$

where A is the equivalents of base necessary to raise the pH of the

solution from pH 4 to 9 and B is the dry weight equivalent of the sol being titrated.

For the three unmodified silica sols used in the experiments described in the following sections (LUDOX SM, HS and TM), the results of these titrations are consistent to within 10% of the manufacturers specifications (based on average particle diameter). For the calculations involving specific surface area/gm, the calculated values based on the particle diameter were used.

5.3.2.3 Measurements & Methods

Flash photolysis experiments were performed as described in chapter 2. This reaction system has been studied using flash photolysis techniques rather than continuous photolysis techniques, as flash photolysis data allows the direct calculation of bimolecular rate constants. Calculation of individual reaction rate constants from continuous photolysis experimental data assumes knowledge of the rate constants involving sacrificial electron donors. As discussed in section 4.3.2.3, since the effect of charged interfaces on these donor reaction is not known, the determination of kinetic parameters from continuous photolysis experimental data is difficult.

5.3.2.3.1 Sample Preparation for Flash Photolysis Experiments

1×10^{-4} M ZnP^{+4}, 1×10^{-2} M PVS°, and 5.0% w/v silica colloid stock solutions were freshly prepared within 24 hr of flash photolysis experiments. The pH of the stock solutions of ZnP^{+4} and PVS° was adjusted to ≈7 before use. 10 ml of sample solutions were typically prepared by combining 1 ml each of the polyelectrolyte, PVS°, and ZnP^{+4} stock solutions into a 10 ml volumetric flask and diluting to a final volume of 10 ml. The stock solution containing silica was added to the flask before the ZnP^{+4} stock solution to prevent precipitation of the silica by ZnP^{+4}, which occurs when $[ZnP^{+4}]>>[SiO^-]$. Homogeneous solutions containing no silica colloid were prepared in a similar manner but without the addition of the silica stock solution to the final dilution. The PVS° concentration of all solutions flashed was 1×10^{-3} M. The pH of the final dilutions was adjusted prior to degassing. 3 ml aliquots of the final dilutions were measured into specially designed airtight flash photolysis cells (see section 2.2.1.4) using a disposable 5 ml plastic syringe. Samples were deoxygenated by flushing the cell contents with purified argon gas for 30 min (Ar flow rate ≈ 100ml/min). Argon gas scrubbing methods are described in chapter 2. The estimated residual O_2 concentration is $\approx2\times10^{-7}$ M (see section 2.2.5.2)

Note: Most of the experiments using colloidal silica sols were performed using the 12 nm diameter particle size suspensions (Ludox HS or AM) available from du Pont. The concentration of silica in solution used in flash photolysis is typically 5.0% w/v. This corresponds to a particle

concentration of 4.2×10^{-5} M assuming a spherical particle of 6 nm radius and a particle density of 2.2 g/cm^3. The concentration of ZnP^{+4} used throughout in flash experiments was 1×10^{-5}M. Using these concentrations of ZnP^{+4} and silica, there is, on the average, only one ZnP^{+4} bound to the surface of a silica particle. In this case, no significant ZnP^{+4} - ZnP^{+4} interactions occur on the silica surface. At significantly lower silica concentrations, the excited-state lifetime of ZnP^{+4} is considerably decreased due to triplet-triplet interactions between photosensitizer molecules on the same silica particle.

5.3.3 Flash Photolysis Experimental Results

5.3.3.1 Kinetic Model

The original model used to simulate transient absorbance data is described in section 3.5.3.2. The equation describing the transient behavior of $^{3*}ZnP^{+4}$ is

$$5.3.1) \qquad [^{3*}ZnP^{+4}]_{(t)} = [^{3*}ZnP^{+4}]_0 \exp[-(k_1 + k_2[PVS^\circ])t],$$

where $k_1 = k_d + k_q'[O_2]$ and $k_2 = k_f + k_q$. $[^{3*}ZnP^{+4}]_0$ is determined by monitoring the initial absorbance change at 480 nm. The transient behavior of $PVS^{-\cdot}$ is given by the following differential equation

5.3.2) $$d[PVS^-]/dt = k_f[PVS^\circ][^3*ZnP^{+4}] - k_b[PVS^{-}\cdot]^2.$$

Substituting the expression for $[^3*ZnP^{+4}]$ found in equation 4.3.21 into the above equation gives

5.3.3) $$d[PVS^-]/dt = k_f[PVS^\circ]\,[^3*ZnP^{+4}]_0 \exp\,[-(k_1 + k_2[PVS^\circ])t] - k_b[PVS^{-}\cdot]^2.$$

Fitting of experimental data is simplified in this case by the fact that in silica-containing flash samples $k_b << k_f$. Because the rate of the forward reaction is very fast relative to the back-reaction rate, the forward reaction appears to be instantaneous on the time scale that $[PVS^{-}\cdot]$ is typically monitored. In this case, equation 5.3.3 can be approximated as

5.3.4) $$d[PVS^-]/dt = - k_b[PVS^{-}\cdot]^2.$$

Through a change in variable (from $[PVS^{-}\cdot]$ to $1/[PVS^{-}\cdot]$), equation 5.3.4 can be expressed as

5.3.5) $$d(1/[PVS^{-}\cdot])/dt = k_b\epsilon_{602}$$

The assumptions discussed in section 4.3.3.2 have also been used in the derivation of equation 5.3.4 and 5.3.5, i.e., $[PVS^-] = [ZnP^{+5}\cdot]$. If this model and the assumptions used in the derivation of equations 5.3.4 and 5.3.5 are correct, a simple reciprocal plot of the ΔA_{600} vs. time data (neglecting initial times when the forward-reaction is still occuring) should be linear with a slope of $-k_D \times \epsilon_{602}$ (ϵ_{602} is the extinction coefficient of PVS^- at 602 nm).

Typical transient absorbance data for silica-containing samples is shown in figures 5.3.2 and 5.3.3. In figure 5.3.2, the absorbance change at 600 nm is shown on a time scale from 0 to 15 mS. The initial buildup of PVS^- cannot be resolved when the transient data is depicted on this relatively slow time scale. The only reaction observable in this figure is the back-reaction, as evidenced by the decrease in ΔA_{602} (due to $PVS^{-}\cdot$). If the same sample is shown on a time scale of 0 to 0.3 mS, as in figure 5.3.3, it can be seen that in addition to an initial ΔA_{602} at t=0, ΔA_{602} initially increases with time. ΔA_{602} at t=0 is due to absorption of $^{3*}ZnP^{+4}$ at 602 nm, which is rapidly scavenged by PVS° through collisional and electron-transfer quenching. This has been confirmed by flash experiments designed to determene the excited-state extinction coefficents of $^{3*}ZnP^{+4}$, which is discussed in section 2.2.5.1. The buildup of PVS° via forward reaction is responsible for the increase in absorbance with time after t=0 that can be seen in figure 5.3.3.

Figure 5.3.2

Transient Absorbance Data :Colloidal Silica-Containing Samples

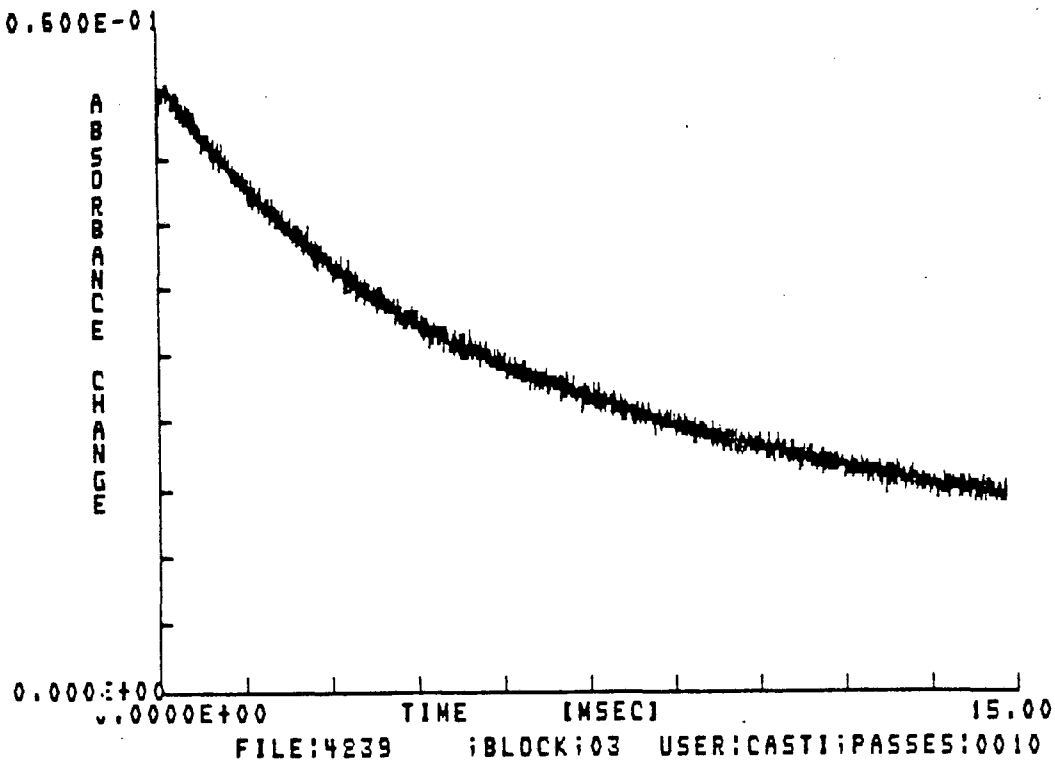

Transient absorbance change at 600 nm.

$[ZnP^{+4}] = 1.0\times10^{-5}$ M; $[PVS^{\circ}] = 1\times10^{-3}$ M; 5.0%w/v Ludox AM colloidal silica. Sample adjusted to pH 7.0 prior to degassing and flashing.

For comparison purposes, figure 5.3.3 also shows the transient absorbance behavior of a homogeneous sample (no silica) containing the same concentrations of photosensitizer and electron acceptor used in the heterogeneous sample. Note that the decrease in absorbance with time that occurs after the initial buildup occurs is markedly faster in the homogeneous sample, while the buildup of absorbance is quite similar, at least in the time range of 0-50 μS. This behavior indicates that there is a selective decrease in back-reaction rate in the silica system as compared to the homogeneous system. The forward reaction seems to be only slightly affected by the addition of the colloidal silica. All silica-containing samples exhibited similar behavior w.r.t. forward reaction, i.e., no significant decrease in forward reaction rates was ever observed in silica-containing samples.

In contrast to the minimal effect that silica particles have on the forward-reaction, the back-reaction in silica-containing samples is consistently slower than the corresponding homogeneous solutions. In Figure 5.3.3, no detectable back-reaction can be observed for the silica-containing sample for up to 300 μs. The homogeneous sample has almost completely back-reacted in the same amount of time, as evidenced by the nearly complete dissappearance in transient absorbance after 300μs.

Figure 5.3.3

Transient Absorbance Data: Homogeneous vs. Colloidal Silica Containing Solutions

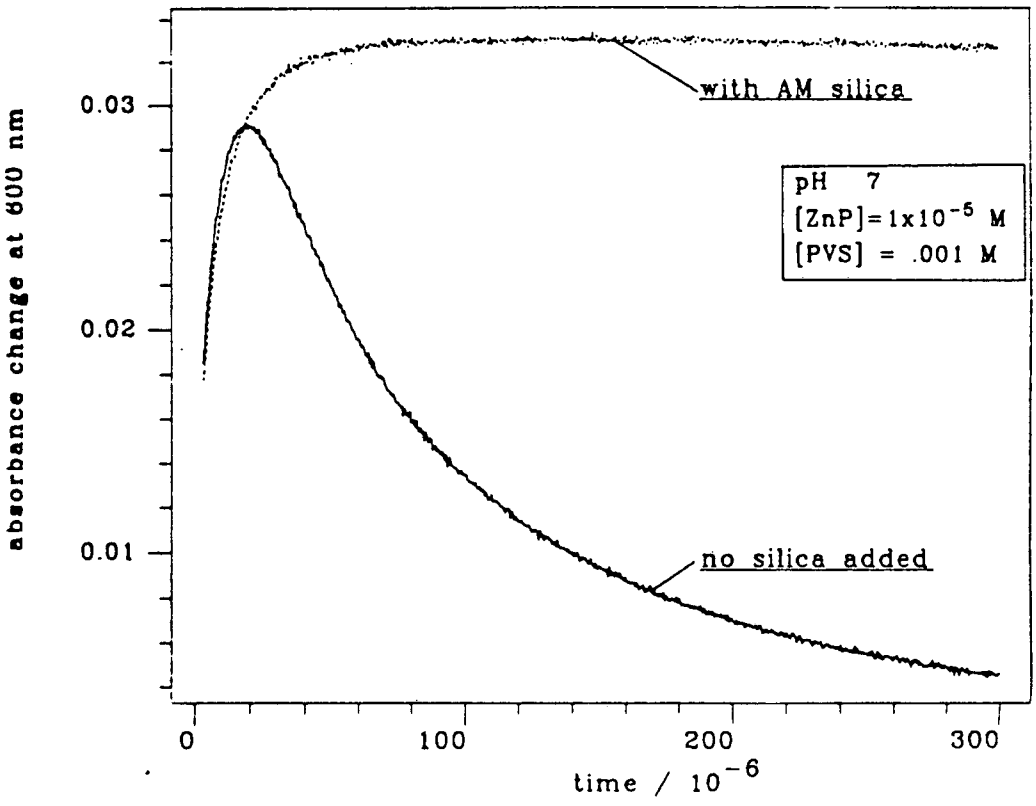

Transient absorbance change at 600 nm.

$[ZnP^{+4}] = 1.0\times10^{-5}$ M; $[PVS^{\circ}] = 1\times10^{-3}$ M

Samples were adjusted to pH 7.0 prior to degassing and flashing

a) no silica present

b) 5.0% w/v Ludox AM silica colloid present

In order to quantitate the effect of colloidal silica sols on back-reaction rates, $1/\Delta A_{600}$ vs. time plots were constructed so that bimolecular rate constants could be obtained using equation 5.3.4. Figure 5.3.4 is a plot of the using the same data and x-axis (time) that was used to create figure 5.3.2, but the y-axis in figure 5.3.4 shows the reciprocal absorbance change. Equation 5.3.4 predicts that a plot of this form should be linear with a slope of $k_b\epsilon_{602}$. The deviation from linearity of the reciprocal absorbance data is clearly visible, which means that the kinetic model developed to describe the back-reaction is inadequate to describe the kinetics of the back-reaction throughout the course of the reaction. The upward curvature of the reciprocal absorbance plots visible between 20 and 100 mS indicates that the rate of dissapearance of $PVS^{-\cdot}$ is faster than predicted using the simple second-order kinetic scheme proposed above. Refinement of the model is necessary to describe the observed kinetics.

Since oxygen contamination was found to influence excited-state quenching experiments (see sections 2.2.5.2 and 4.3.3.3), it was thought that the residual oxygen present in the flash samples ($[O_2]_{liquid}$ = 2.3×10^{-7} M) might also be interfering with the back-reaction in silica-containing samples. The slowness of the back-reaction rate observed in silica sol solutions could allow side reactions such as the removal of $PVS^{-\cdot}$ by oxygen to compete effectively with back-reaction and influence reaction kinetics.

Figure 5.3.4

Transient Absorbance at 600 nm of Colloidal Silica-Containing Sample: Reciprocal Absorbance vs. Time

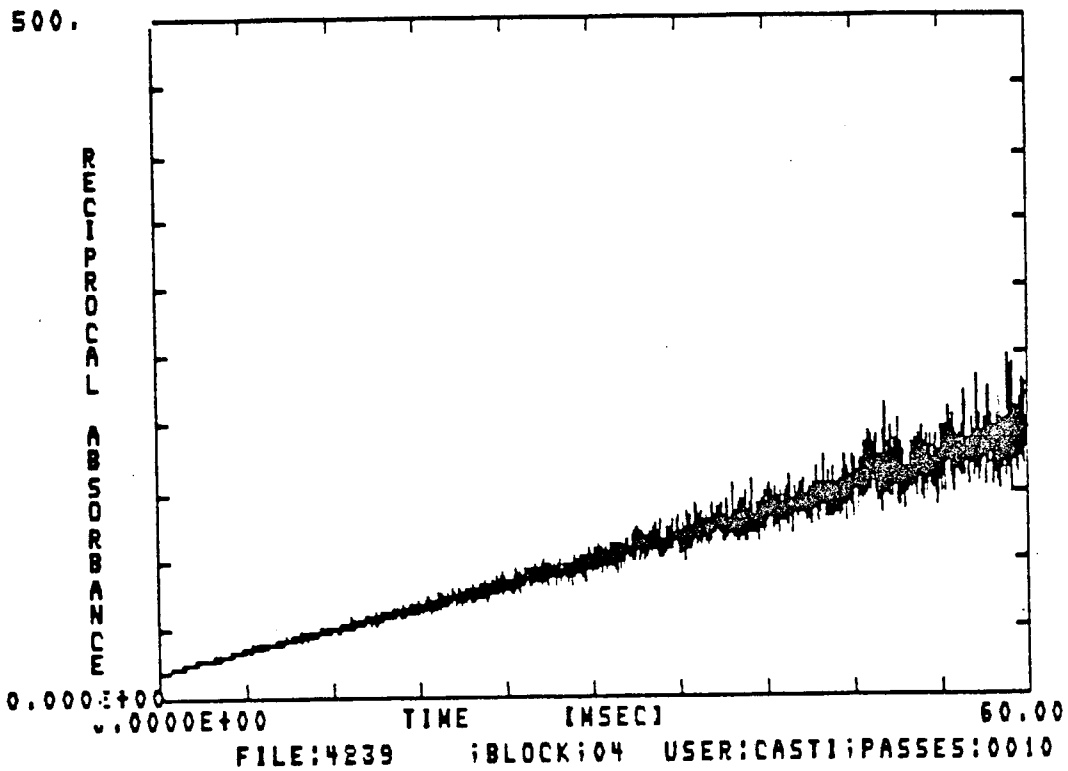

Transient absorbance change at 600 nm.

$[ZnP^{+4}] = 1.0\times10^{-5}$ M; $[PVS^{0}] = 1\times10^{-3}$ M; 5.0% w/v Ludox AM silica colloid present. Sample adjusted to pH 7.0 prior to degassing and flashing.

It is well known that residual oxygen in solution scavenges reduced viologen species. This is demonstrated by the observation of a delay in the onset on reduced viologen appearance in continuous photolysis systems containing sacrificial electron donors. [25] Reduced viologen formed early in the photoreaction is immediately reoxidized by residual oxygen in solution. The appearance of reduced viologen does not occur until all of the residual oxygen is depleted.

When a small volume of oxygen is added to a degassed flash photolysis sample containing ZnP^{+4} (1×10^{-5} M), PVS° (0.001 M) and colloidal silica (5.0% w/v), the decay rate of [$PVS^{-}\cdot$] increases, which indicates that residual oxygen does influence the decay kinetics of $PVS^{-}\cdot$.

The influence of residual oxygen on the kinetics of the photoreaction of ZnP^{+4} and PVS° in the presence of colloidal silica can be accounted for in the manner described below. Equation 5.3.4 is modified by the addition of a term which accounts for the depletion of $PVS^{-}\cdot$ by oxygen. This term is included in the following equation;

$$5.3.6) \qquad d[PVS^{-}]/dt = - k_b[PVS^{-}\cdot]^2 - k'_{O_2}[PVS^{-}\cdot][O_2]$$

where k'_{O_2} is the rate constant for scavenging of $PVS^{-}\cdot$ by O_2. Note that this rate constant is different than k_{O_2}, the rate constant for quenching of $^{3*}ZnP^{+4}$ by O_2 discussed in section 2.2.5.2.

The inclusion of another reaction for $PVS^{-\cdot}$ into the kinetic model invalidates the approximation that $[PVS^{-\cdot}] = [ZnP^{+5\cdot}]$. The approximation may still be valid in the early stages of reaction, however, depending on the extent of reaction, the relative values of the rate constants k_b and k'_{O_2} and the concentrations of $PVS^{-\cdot}$ and O_2. Note also that since the first term in equation 5.3.6 is second order in $[PVS^{-\cdot}]$, the larger the initial concentration of $PVS^{-\cdot}$, the smaller the influence of the oxygen scavenging term will be.

In the early stages of reaction when $[PVS^{-\cdot}] \approx 2.3\times10^{-6}$ M, the first term on the right side of equation 5.3.6 is $\approx 2.6\times10^{-4}$ M s^{-1} (this assumes $k_b \approx 5\times10^{7}$ $M^{-1}s^{-1}$). Using the values for k_{O_2} and $[O_2]$ determined in section 2.2.5.2 and assuming a diffustion-controlled reaction of oxygen with $PVS^{-\cdot}$ (a worst-case estimate), the second term in equation 5.3.6 is $\approx 7.4\times10^{-4}$ M s^{-1}. By comparing the relative magnitude of these two terms it can be seen that the residual oxygen in solution can have a significant influence on the reaction kinetics of $PVS^{-\cdot}$ disappearance. The actual magnitude of the oxygen scavenging term depends upon the value of k'_{O_2}.

In order to extract kinetic parameters from transient absorbance data, the influence of back-reaction and oxygen quenching of $PVS^{-\cdot}$ need to be separated from each other. This is done by performing flash

experiments at varying laser intensities. At higher laser intensities, the initial concentration of $PVS^{-\cdot}$ increases. Since the first term in equation 5.3.6 contains a $[PVS^{-\cdot}]^2$ term while the the second term contains $[PVS^{-\cdot}]$ to the first power only, the relative magnitude of the $k_b[PVS^{-\cdot}]^2$ term increases compared to the $k_{O_2}[PVS^{-\cdot}][O_2]$ term as $[PVS^{-\cdot}]$ increases. In the limit of high $[PVS^{-\cdot}]$, the $k_{O_2}[PVS^{-\cdot}][O_2]$ term is insignificant and the slope of a $1/\Delta A$ vs. t plot corresponds to $k_b\epsilon_{602}$.

The initial concentration of $PVS^{-\cdot}$ is limited in a flash photolysis experiment by the the number of incoming photons, the concentration of photosensitizer and the efficiency of forward electron-transfer reaction. In the experiments reported in this section, the concentration of $PVS^{-\cdot}$ is never greater than $\approx 5\times10^{-6}$ M, so the limit of high $[PVS^{-\cdot}]$ can never really attained. Values for k_b and k_{O_2} are determined by extrapolation to high $[PVS^{-\cdot}]$ in the following way. A change in variable operation is performed on equation 6.3.6 so that transients can be monitored in the reciprocal absorbance form. This results in the following equation:

$$5.3.6) \qquad d(1/[PVS^{-\cdot}])/dt = -k_b - k_{O_2}[O_2]/[PVS^{-\cdot}]_{initial}.$$

where $[PVS^{-\cdot}]_{initial}$ is the maximum concentration of $PVS^{-\cdot}$ that is obtained during a particular experiment.

Values of k_b and $k_{O_2}[O_2]$ are determined using equation 5.3.6 by plotting the apparent reaction rate ($d(1/[PVS^{-\cdot}])/dt$) during the inital stages of the back-reaction (between 0 and 15 ms) as a function of $1/[PVS^{-\cdot}]_{initial}$. If the proposed model is applicable and the assumptions are correct, a straight line with a slope of $k_{O_2}[O_2]$ and an intercept of k_b should be able to be drawn through the data points.

Implicit in the preceding derivation are the assumptions that $[PVS^{-\cdot}] \equiv [ZnP^{+\cdot}]$ and that $[PVS^{-\cdot}] \equiv [PVS^{-\cdot}]_{initial}$. Both of these assumption are valid only during the initial stages of the reaction. The deviations from linearity of $1/\Delta A$ vs. t plots of transient data from is likely to be due to the failure of these two assumptions.

$1/\Delta A$ vs. t plots of transient absorbance data governing a wide time range do deviate from linearity, as shown in figure 5.3.4. Linearity of these plots is observed, however, when only the beginning of the decay of $PVS^{-\cdot}$ is plotted, as shown in figure 5.3.5. In this plot only the first 15 ms of data are depicted rather than the entire decay profile of the transient signal. The linearity of this plot implies that over the time range used in figure 5.3.5, the assumptions of the model used to derive equation 5.3.6 are valid.

Figure 5.3.6 shows the results of plotting experimental data in the manner described above to determine k_b and k_{O_2}. $[PVS^{-\cdot}]_{initial}$ is varied by placing neutral density filters in the path of the incoming laser beam

so as to decrease the initial concentration of $^{3*}ZnP^{+4}$. The range of $[PVS^{-\cdot}]_{initial}$ obtainable by this method is 0.7-3.6x10^{-6} M. The slope and intercept of the linear least-square fit of the data is; intercept = k_b= 1.05x10^7 M^{-1} s^{-1}, slope = $k_{O_2}[O_2]$ = 36.8 s^{-1}. Since $[O_2]$ is known (see section 2.2.5.2, k_{O_2} is calculated to be 36.8 s^{-1}/2.3x10^{-7} M = 1.6x10^8 M^{-1} s^{-1}. For all experiments containing silica, this technique was used to determine k_b.

Variations in the determination of $k_{O_2}[O_2]$ were observed from sample to sample. This variation is ascribed to small sample-to sample changes in $[O_2]$ due to differences in degassing efficiency.

The observed deviations from pure second-order decay of $PVS^{-\cdot}$ are thus adequately described by a modified kinetic scheme in which residual oxygen competes with oxidized $ZnP^{+5\cdot}$ for $PVS^{-\cdot}$. Oxygen impurities so not appear to be important in homogeneous reaction systems because k_b is larger in the homogeneous system ($k_b \approx 7\times10^9$ $M^{-1}s^{-1}$)compared to the silica colloidal system($k_b \approx 1\times10^7$ $M^{-1}s^{-1}$. The influence of the $k_{O_2}[O_2][PVS^{-\cdot}]$ term in equation 5.3.6 becomes neglible compared to the $k_b[PVS^{-\cdot}]^2$ term when the value of k_b approaches 10^{10} $M^{-1}s^{-1}$.

Figure 5.3.5

Transient Absorbance at 600 nm of Colloidal Silica-Containing Sample: Reciprocal Absorbance vs. Time

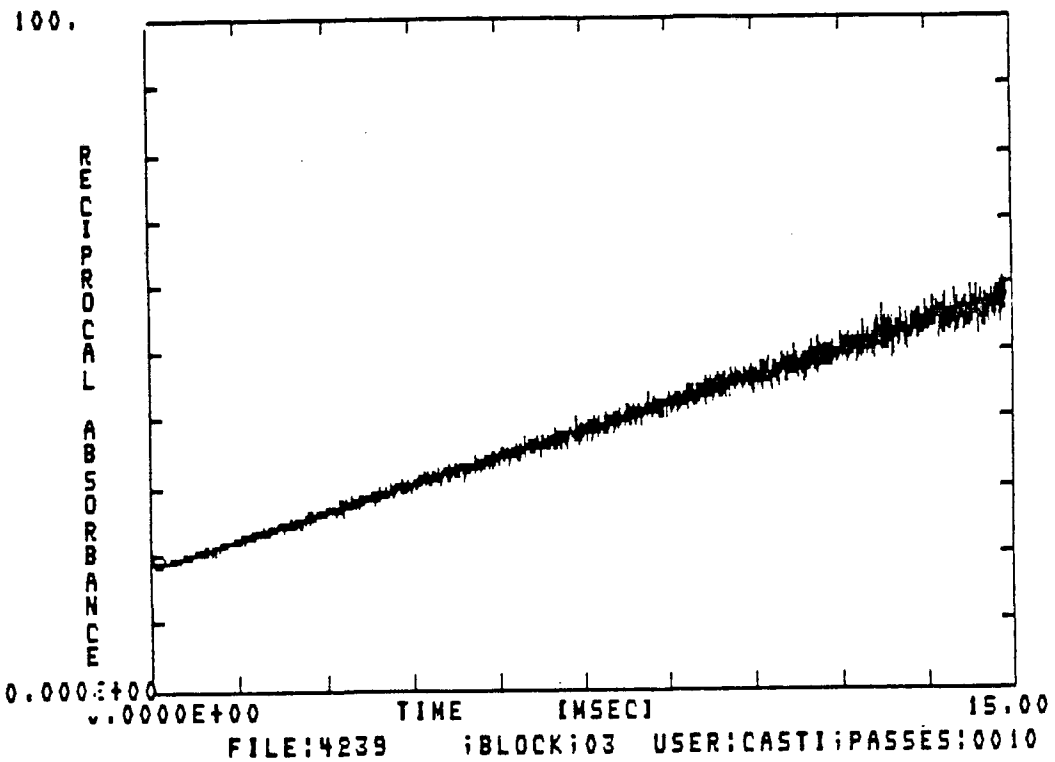

Transient absorbance change at 600 nm.

$[ZnP^{+4}] = 1.0\times10^{-5}$ M; $[PVS^{0}] = 1\times10^{-3}$ M; 5.0% w/v Ludox AM silica colloid present. Sample adjusted to pH 7.0 prior to degassing and flashing.

Figure 5.3.6

Graphic Determination of k_b and k'_{O_2}

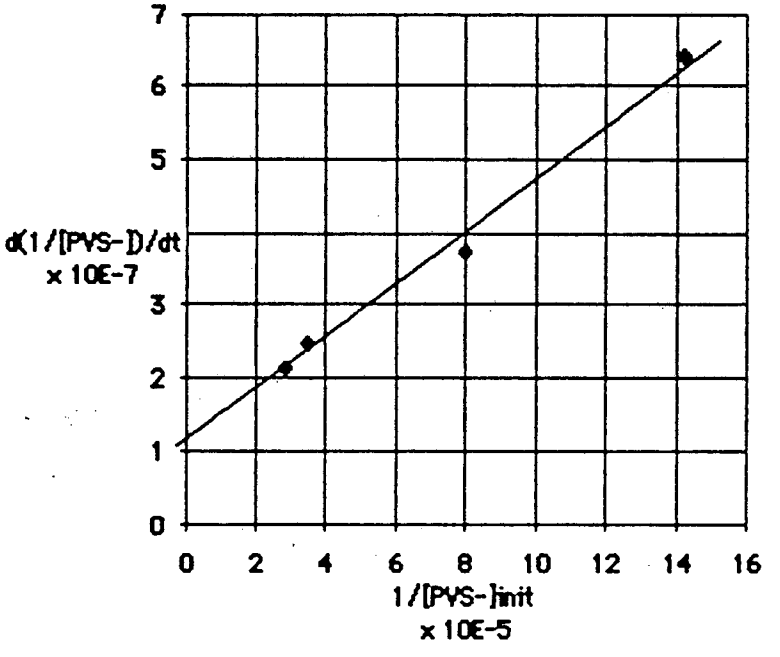

Effect of initial (maximum) $PVS^{-\cdot}$ concentration on initial slope of reciprocal absorbance plot (600 nm decay). Experimental conditions: $[ZnP^{+4}] = 1\times10^{-5}$ M; $[PVS^{\circ}] = 1\times10^{-3}$ M; Ludox AM colloidal silica = 5.0 wt %; temperature = 20 C; 3 ml sample degassed using argon purging as described in section 5.3.2.3.; initial slopes determined using the first 15 ms of transient data as shown in figure 5.3.5.

Flash photolysis experiments were also performed using Ludox silica sols of particle diameter 7, 12 and 22 nm diameter in order to determine the effect of particle size on back-reaction rate. The theory of dimensionality outlined in section 5.1.2.3 predicts that there should be no express dependence of reaction rate on particle diameter for collision-controlled reactions. Flash experiments confirmed this prediction. Back-reaction rate constants (k_b) were determined at pH 9.0 for samples containing equivalent silica surface areas/volume of Ludox SM (7 nm), HS (12 nm) and TM (22 nm) unmodified colloidal silica sols were the same to within experimental variation. The fact that k_b is independant of particle diameter implies that the theory of dimensionality outlined in section 5.1.2.3 can be used to describe the influence of particle size on reaction rate for the collision-controlled back-reaction between $ZnP^{+5\cdot}$ and $PVS^{-\cdot}$.

The kinetic model described above is used throughout the following sections to determine k_b in silica sol-containing systems under various experimental conditions. In particular, the influence of alumina-modification of silica sols on the influence of pH on the charge density on the silica surface is determined by following k_b as a function of pH. This is the topic of the following section.

5.3.3.2 Effect of pH and Ionic Strength on Back-Reaction

A study of the influence of pH on the back-reaction rate in the presence of both alumina-modified and unmodified silica sols was undertaken to determine if alumina-modified silica sols would indeed be more effective than unmodified silica sols in reducing back-reaction in neutral and acidic media.

As discussed in section 5.2.1, unmodified colloidal silica sols can be used only in high pH media because the decrease in surface charge density of silica at neutral and low pH induces gel formation of silica suspensions. This instability leads to a decrease in the effectiveness of colloidal silica.

Both the surface charge density and stabilty of silica sols are important factors in determining the usefulness on silica sols in artificial photosynthetic systems. Alumina-modified silica sols are expected to be significantly more effective in the pH regime in which unmodified silica is both ineffective as a charged interface and unstable because of protonation of surface silanol groups. The increased acidity of surface silicoaluminate sites is responsible for the difference in properties of unmodified vs. alumina-modified silica sols.

The hypothesis that alumina-modified sols function more effectively than unmodified silica sols at neutral and acidic pH was tested by

performing flash photolysis experiments on solutions containing equal concentrations of photosensitizer (ZnP^{+4}), electron donor (PVS^{0}), and containing either unmodified silica (Ludox HS, 12 nm diameter particles) or alumina modified silica (Ludox AM, 12 nm diameter). The only experimental variables were the addition of either Ludox AM or HS, the pH of the solution flashed and the solution ionic strength. k_b's were determined using the method described in section 5.3.3.1. In all cases a linear relationship between the inital decay rate ($d(1/[PVS^{-\cdot}]/dt$) and $1/[PVS^{-\cdot}]_{initial}$ was obtained. k_b's were determined by extrapolating to $1/[PVS^{-\cdot}]_{initial} \longrightarrow 0$. The effect of solution pH on back-reaction rate for both alumina-modified and unmodified silica sols is shown in figure 3.5.7.

The most striking conclusion that can be deduced from the data presented in figure 3.5.7 is that the alumina-modified silica sol retains nearly 100% of its effectiveness in preventing back-reaction thoughout the pH range of 10-6, whereas the unmodified sol is already only half as effective in preventing back-reaction at pH 8 than it is at pH 10. At pH 6.5, the back-reaction rate for the unmodified sol is significantly faster than that of the alumina-modified sol. This behavior indicates that the charge density of the alumina-modified silica particles is higher than the unmodified silica particles in neutral pH medium. The prediction that the more acidic surface of the alumina-modified particles would be more effective than unmodified silica is confirmed by these results.

Figure 5.3.7

Effect of pH on Back-Reaction Rates: Alumina-modified vs. Unmodified Ludox Colloidal Silica Sols

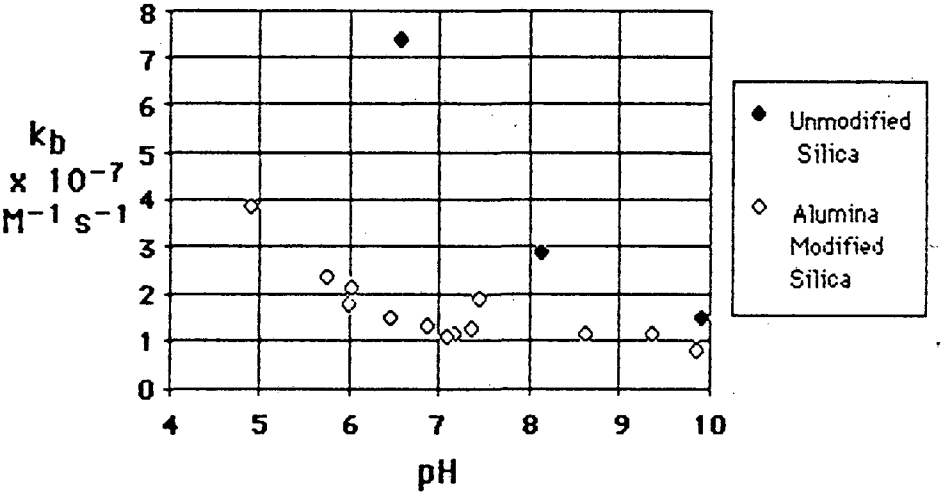

Experimental conditions: $[ZnP^{+4}]$ = 1×10^{-5} M; [PVS°] = 1×10^{-3} M; Ludox (AM or HS) colloidal silica = 5.0 wt %; temperature = 20 C; 3 ml sample degassed using argon purging as described in section 5.3.2.3.; k_b determined using the first 15 ms of transient data.

In order to confirm the mechanism of the effect of charged colloidal particles on bimolecular reaction rates, the effect of ionic strength on back-reaction rates was studied. In the theoretical treatment outlined in section 5.1.2, Equation 5.1.2 relates the surface charge density of a charged particle to the electric field surrounding the particle. Equation 5.1.3 relates the functional dependance of an interionic reaction rate k_1 on the electric field strength. These two equations can be combined as follows to obtain the influence of ionic strength on reaction rate;

$$5.3.7) \qquad k_1 = A \exp[(-2e/F)\operatorname{arcsinh}(\sigma_s/(2DRT/\pi)^{1/2} C^{1/2})].$$

This expression shows that an increase in ionic strength is predicted to lead to a increase in the reaction rate constant between oppositely charged species. Although the functional form of equation 5.3.7 is more complex than the same expression derived for simple salt solutions (see section 3.2.1.1), the general trend of rate with ionic strength is similar.

Figure 5.3.8 depicts the effect of ionic strength on back-reaction rates for samples containing alumina-modified colloidal silica. The general trend of increasing k_b with increasing ionic strength is consistent with the proposed model of the influence of the electric field surrounding the negatively charged colloidal particles on back-reaction rates.

Figure 5.3.8

Effect of Ionic Strength on Back-Reaction Rates: Alumina-Modified Silica-Containing Samples

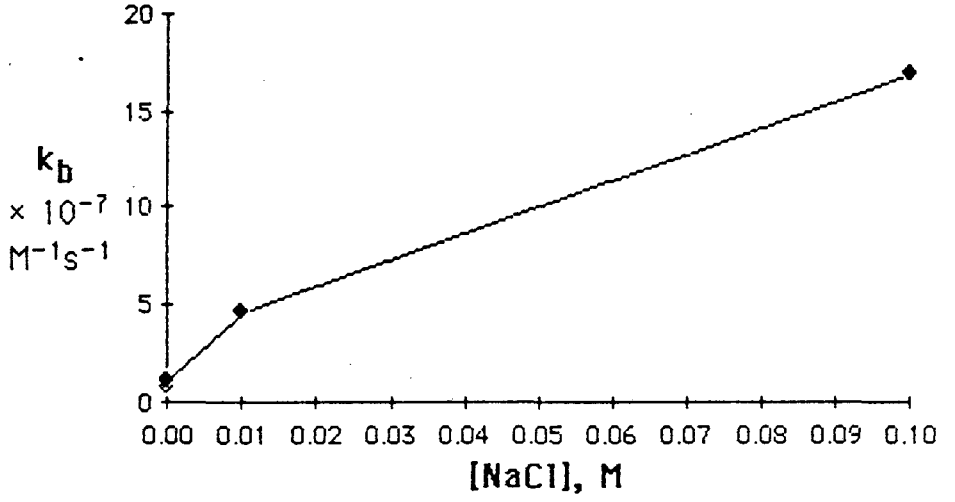

Experimental conditions: $[ZnP^{+4}] = 1\times10^{-5}$ M; $[PVS^{0}] = 1\times10^{-3}$ M; Ludox AM colloidal silica = 5.0 wt %; temperature = 20 C; 3 ml sample degassed using argon purging as described in section 5.3.2.3.; k_b determined using the first 15 ms of transient data as described in section 5.3.3.1.

The next section describes experiments designed to study the strength of the effective electric field surrounding a colloidal particle. Observation of the temperature dependance of back-reaction rate is used to determine the activation energy of back-reaction using a simple arhenius-type plot. This energy barrier is related to the potential field surrounding the charged particle through the use of equation 5.1.2.

5.3.3.3 Effect of Temperature on Back-Reaction: Determination of the Effective Electric Field Surrounding a Charged Silica Particle

It has been demonstrated in the preceding sections that the electric field surrounding a charged colloidal particle is largely responsible for the observed decrease in back-reaction rates between oppositely charged photoproducts in photosystems such as the one studied in this thesis. The magnitude of the rate-retarding influence of these charged particles can be related to the surface charge density of the particle, which has been estimated to be 0.18 C/m^2. [4] An independent estimate of the surface charge density is possible by determining the temperature dependence of back-reaction rate. As described in section 5.1.2.2, transition-state theory can be used to determine the effect of changes in activation energy on reaction rates. The equation that describes this relationship is

5.3.8) $k_1 = A \exp[-E_a/kT]$.

For the reaction between oppositely charged species, the addition of charged particles to the reaction system will induce binding of one of the reactants to the particle. Charged reactants in solution are influenced by the electric field surrounding the charged particle. The potential barrier which must now be surmounted in order for reaction between oppositely charged species to occur imposes an additional term to the activation energy of the reaction. If this term is much larger than the activation energy for the homogeneous reaction, equation 5.3.8 can be expressed as follows;

5.3.9) $k_1^* = A \exp [-e\Psi/kT]$

where $e\Psi$ is the magnitude of the potential barrier imposed by the charged particle. Ψ is the potential (in volts) of the electric field surrounding the particle. Ψ is calculable using equation 5.1.2 if the ionic strength and surface charge density of the charged particle in question are known.

The estimation of the surface charge density can be confirmed by experiments in which k_b is determined as a function of temperature. Substituting k_b for k_1^* and taking the log of both sides of equation 5.3.9 gives

5.3.10) $\log(k_b) = \log(A) - e\Psi/kT.$

A plot of $\log(k_b)$ vs. 1/T should yield a straight line with a slope of $e\Psi/k$ and an intercept of log(A). This is a classic arrhenius plot, but in this case the result (E_a) can be related to the surface charge density of the particle through transition-state theory and the Gouy-Chapman-Stern model of the charged interface.

For the back-reaction between $PVS^{-\cdot}$ and $ZnP^{+5\cdot}$, k_b was determined throughout the temperature of 0-50 C. Figure 5.3.9 shows the arrhenius-type plot that was used to determine Ψ. The slope of the best-fit line through the experimental data gave a slope of 13.4 kJ/Mole. This corresponds to an effective surface potential of 140 mV, which corresponds well to the reported surface charge density of silica sols of ≈170 mV. [4]

The agreement between calculated and determined surface potential supports the conclusion that the surface charge density of the alumina-modified silica sol is responsible for the observed decrease in the rate of back-reaction between $ZnP^{+4\cdot}$ and $PVS^{-\cdot}$. This conclusion is also supported by the observed dependance of k_b on ionic strength.

Figure 5.3.9

Arrhenius-Type Plot to Determine Surface Potential of Ludox AM Alumina-Modified Colloidal Silica Sol

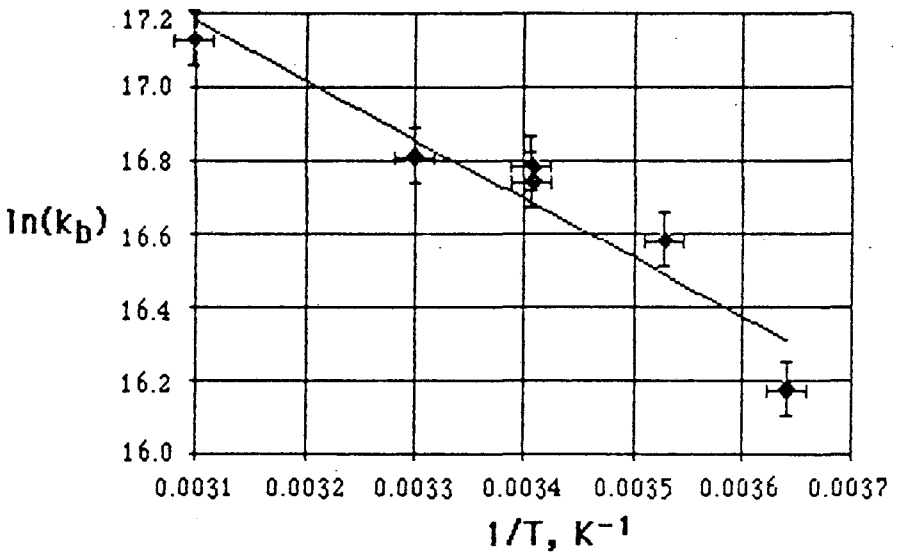

Experimental conditions: $[ZnP^{+4}] = 1\times10^{-5}$ M; $[PVS^{\circ}] = 1\times10^{-3}$ M; Ludox AM colloidal silica = 5.0 wt %; temperature = 0-50 C; 3 ml samples degassed using argon purging as described in section 5.3.2.3.; k_D's determined using the first 15 ms of transient data; kinetic analysis described in section 5.3.3.1.

5.4 Conclusions

A kinetic model has been developed that describes the transient absorbance behaviour of ZnP^{+4}/PVS°/colloidal silica photolysis systems in which pure second-order decay of initial photoproducts ($ZnP^{+5\cdot}$ and $PVS^{-\cdot}$) is perturbed by scavenging of $PVS^{-\cdot}$ by residual O_2.

Flash photolysis experiments have confirmed that alumina-modified silica particles are significantly more effective than unmodified silica sols in neutral pH media at decreasing the rate of back-reaction between $ZnP^{+4\cdot}$ and $PVS^{-\cdot}$. At pH 7, the addition of alumina-modified silica sol decreases k_b by almost three orders of magnitude relative to homogeneous solution, from 7×10^9 M^{-1} s^{-1} to 1.2×10^7 M^{-1} s^{-1}. At this pH, unmodified silica is unstable and therefore unusable as a charged interface for retarding back-reaction. Alumina-modified silica sols therefore offer a significant advantage over unmodified sols in that alumina-modified sols can be used throughout the pH range of ≈6-11. Unmodified sols are restricted to alkaline pH media because of surface protonation which occurs below ≈pH 8.

A study of the effect of ionic strength on back-reaction rate confirms that the influence of alumina-modified colloidal silica sols is due to the electric field gradient surrounding the negatively charged particle. Temperature dependance studies have determined that the activation energy for back-reaction in the presence of alumina-modified

silica particles at pH 7 is 13.4 kJ/Mole. This corresponds to an effective surface potential of 140 mV.

A study of the effect of particle size on back-reaction rates has determined that for the particle size range between 7 and 22 nm, no express dependence of k_b on particle size exists. This behavior confirms predictions based on dimensional considerations that collision-controlled reaction rates involving a particle-bound reactant are independent of particle size.

The practical implication of this observation is that smaller diameter silica sols are as effective as larger diameter sols in preventing back-reaction. An advantage of using the smaller size sols is that since smaller diameter sols have a higher surface area/volume ratio than larger sols, a lower concentration (by weight) of the smaller diameter sol contains an equivalent area of charged surface. Less of the smaller diameter sol is needed. In addition, in solutions containing equal surface area equivalents of silica (m^2 surface area/volume), the probability of there being more than one ZnP^{+4} per particle is reduced in smaller particle diameter systems. The bimolecular ZnP^{+4} self-quenching reaction that occurs when more than one ZnP^{+4} is bound to a silica particle can therefore be controlled using a lower concentration of the smaller diameter silica sol than would normally be needed in the case of a larger particle.

4.5 References

1) Chapter 1, references 7-12

2) Willner, I., Yang, J. M., Laane, C., Otvos, J. W., Calvin, M., J. Phys. Chem., 35, 3277 (1981)

3) Willner, I., Degani, Y., Isr. J. Chem., 22, 163 (1982)

4) Laane, C., Willner, I., Otvos, J. W., Calvin, M., Proc. Natl. Acad. Sci. USA, 78, 5928 (1981)

5) Yang, J. -M., Ph.D Thesis, University of California at Berkeley, 1981 (LBL Report # LBL-13650)

6) Evans, C. A., Bolton, J. R., Photochem. Photobiol., 30, 697 (1979)

7) Rosen, M. J., "Surfactants and Interfacial Phenomena"; Wiley-Interscience, New York, 1978, pp 28-55

8) Iler, R. K., "The Colloid Chemistry of Silica and Silicates", Cornell Univ. Press, Ithaca, NY 1955

9) Astumian, R. D., Schelly, Z. A., J. Am. Chem. Soc., 106, 304 (1984)

10) North, A. M. "The Collision Theory of Chemical Reactions in Liquids"; Methuen: London, 1964

11) du Pont Technical Bulletin E-64602 ,"LUDOX Colloidal Silica: Properties, Uses, Storage and Handling", 1984

12) Iler, R. K., Wolter, F. J., U. S. Patent 2,631,134 (E. I. du Pont de Nemours & Co., Inc., 1953)

13) Reference 8, pp 99

14) Allen, L. H., Matijević, E., Meites, L., J. Inorg. Nucl. Chem. 33, 1293

(1971).

15) Allen, L. H., Matijevic, E., J. Coll Int. Sci. 31(3), 287 (1969)

16) Schindler, P., Kamber, H. R., Helv. Chim. Acta. 51, 1781 (1968)

17) Depasse, J., Watillon, A., J. Coll. Int. Sci., 33(3), 430 (1970)

18) Alexander, G. B., Iler, R. K., U. S. Patent # 2,897,797 (du Pont, 1959)

19) Tamele, M. W., Discuss. Faraday Soc., 8, 270 (1950)

20) Pauling, L., "Nature of the Chemical Bond", Cornell Univ. Press, Ithaca, NY (1948)

21) Thomas, C. L., Ind. Eng. Chem., 41, 2564(1949)

22) Reference 8, pp 263

23) Bangs, Leigh B., "Uniform Latex Particles", Seragen Diagnostics Inc., Indianopolis, IN, 1984

24) E. I. du Pont de Nemours Analytical Method L750.700, 11/20/80

25) Ford, W. E., Otvos, J. W., Calvin, M., Proc. Natl. Acad. Sci. 76(8), 3590 (1979)

TECHNICAL INFORMATION DEPARTMENT
LAWRENCE BERKELEY LABORATORY
UNIVERSITY OF CALIFORNIA
BERKELEY, CALIFORNIA 94720